# Final report: DOE Contract No. DE-FC26-05NT42456 June 30, 2005 to December 31, 2012

## Sustainable Transportation Fuels from Natural Gas ($H_2$), Coal and Biomass

Gerald P. Huffman, Director, CFFS, and
Professor of Energy Research Emeritus,
University of Kentucky
908 Belmere Drive
Lexington, KY 40509
Phone: (859) 576-9454
E-mail: gphuffman@uky.edu

This report is a revision.
Submission Date: May 10, 2013

**Consortium for Fossil Fuel Science**

University of Kentucky (UK)
Auburn University (AU)
West Virginia University (WVU)
University of Utah (Utah)
University of Pittsburgh (Pitt)

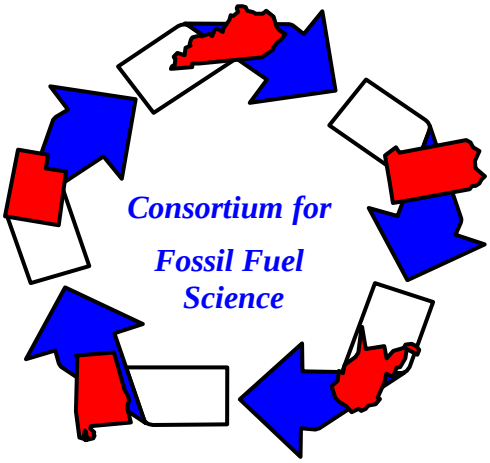

# Table of Contents

# Sustainable Transportation Fuels from Coal, Natural Gas (≥ 90% $C_nH_{2n+2}$ gases) and Biomass

U.S. Department of Energy (Fossil Energy/NETL) Contract No. **DE-FC26-05NT42456**

***Contact:*** Gerald P. Huffman, Director, Consortium for Fossil Fuel Science, Professor of Energy Research Emeritus, University of Kentucky, (859) 576-945, gphuffman@uky.edu

**Abstract:** This research program is focused primarily on the conversion of coal, natural gas (i.e., methane), and biomass to liquid fuels by Fischer-Tropsch synthesis (FTS), with minimum production of carbon dioxide. A complementary topic also under investigation is the development of novel processes for the production of hydrogen with very low to zero production of $CO_2$. This is in response to the nation's urgent need for a secure and environmentally friendly domestic source of liquid fuels. The carbon neutrality of biomass is beneficial in meeting this goal. Several additional novel approaches to limiting carbon dioxide emissions are also being explored.

**Executive Summary:** The items listed below give a very short summary of the most significant results obtained in the research projects conducted during this contract.

- Syngas produced by gasification of coal typically has $H_2$/CO ratios in the range of about 0.5 to 0.9. Fischer-Tropsch synthesis of liquid fuels requires syngas with $H_2$/CO ratios of 2.0 or higher. It is shown that replacement of the traditional water-gas shift (WGS) reaction by catalytic dehydrogenation (CDH) for a 50,000 bbl/day plant can:

- Produce the required $H_2$ (1,000 tons/day)

- Eliminate the emission of 22,000 tons of $CO_2$ per day

- Save over 2,000,000 gallons of water per day

- Produce nearly 3,000 tons per day of multi-walled carbon nanotubes.

- Inexpensive Fe-Ni, Fe-Mo, and Fe-Mn alloys were shown to be excellent catalysts for CDH of hydrocarbon gases.

- Patents have been obtained on CDH and on combining FTS with CDH (FTS-CDH).

- Pt nanoparticles supported on stacked-cone nanofibres are excellent catalysts for dehydrogenation of several high $H_2$ content liquid hydrocarbons.

- Hydrolysis of water containing a suspension of high surface area carbon (BP2000) can produce pure hydrogen at energy efficiencies about four times higher than that for ordinary water electrolysis.

- Hydrothermal treatment of cellulose and lignin in an autoclave produces spherical particles of carbons about 250 nm in diameter. These carbon nanoparticles were found to be nearly as active as commercial carbon BP2000 for producing energy efficient hydrogen electrochemically.

- A wide variety of analytical techniques, including Temperature Programmed Reduction (TPR), BET surface area measurements, Electron Magnetic Resonance (EMR), XRD, SEM, TEM, $^{57}$Fe Mössbauer spectroscopy and XAFS (x-ray absorption fine structure) spectroscopy were used to determine the structure and reactions of the catalysts used for FTS, CDH, and WGS reactions.

- A generic, robust optimization framework was developed that enables identification of economically optimal production schemes for carbon resource processing in polygeneration plants.

- Process models were developed for both gas-phase Fischer-Tropsch Synthesis (FTS) and Supercritical Fluid FTS (SCF-FTS), under investigation by Dr. Christopher Roberts at Auburn University. Economic and Environmental impact analyses were performed for the two FTS processes, which showed that (SCF-FTS) results in an increased operational cost but the increased production rate of fuel range compounds makes up for it.

- We have shown that modifications to the FTS process under dense phase conditions (including supercritical fluid recycle, supercritical fluid phase FTS (SCF-FTS)) results in significant enhancement of middle distillate products while also significantly reducing the production of methane and extending catalyst lifetime due to in situ extraction.

- Integration of product upgrading stages, namely oligomerization and cracking/isomerization reactions, subsequent to the SCF-FTS catalyst bed narrow the FTS products to the fuel range in single pass operation. Specifically, we have operated the continuous SCF-FTS reactor in a triple catalyst bed configuration with Fe and/or Co based FTS catalysts in stage 1, and Pd and zeolite catalysts in stages 2 and 3.

- Process performance is indicated by the following reaction parameters: conversion, selectivity, product yields, and carbon number distribution as related to key reaction conditions including catalyst type, temperature and pressure.

- Pd on mixed iron/ceria aerogels has been found to be very active as a Water Gas Shift Catalyst. Gas phase deposition of Pd via (allyl)(cyclopentadienyl)Pd leads to much better dispersion and higher catalytic activities than obtained from solution phase depositions.

- We have found ferrihydrites to be very active as F-T catalysts (as has SASOL), which yielded primarily n-alkanes.

- Synthetic amorphous ferrihydrites were found to have high activity as catalysts for the Fischer-Tropsch conversion of syngas to liquid fuels over a period of 100 hrs in a fixed bed

reactor at 265 $^{o}$C and 100 psig pressure, representing somewhat better catalytic activity as compared to a commercial bed catalyst.

- We have submitted a patent application which involves the stabilization of high surface area ceria at high temperatures. Ceria has substantial commercial importance, but high surface area forms typically undergo agglomeration on heating.

- We have demonstrated that the active catalyst species for the conversion of sugars to hydroxymethylfurfural involves chromium in the +3 oxidation state, rather than +2 as had been often proposed by others.

- 67 Graduate and Postdoctoral students were trained under the support of this contract. Throughout this report, their names have been highlighted in **bold lettering** and the research they conducted has been briefly described. Their current positions, if known, have been given. It is gratifying that many these young scientists have elected to continue working in the field of fossil fuel science.

# "Eliminating $CO_2$ emissions during the production of liquid fuels from coal and natural gas by combining Fischer-Tropsch synthesis with catalytic dehydrogenation"

G.P. Huffman, N. Shah, F.E. Huggins, Devdas Panjala, Wenqin Shen, and Yuguo Wang,
CFFS and Department of Chemical and Materials Engineering, University of Kentucky

**Abstract:** Catalytic dehydrogenation (CDH) of hydrocarbon gases present in natural gas or produced by Fischer Tropsch synthesis (FTS) yields pure hydrogen and multi-walled carbon nanotubes (MWCNT). The production of liquid fuels from coal-derived syngas by FTS requires that the $H_2$/CO ratio of the syngas be 2.0 or higher. However, the syngas produced by gasification of coal typically has $H_2$/CO ratios in the range of about 0.5 to 0.9. The additional $H_2$ required has traditionally been produced by the water-gas shift (WGS) reaction. Unfortunately the WGS reaction produces one molecule of $CO_2$ and uses one molecule of $H_2O$ for each molecule of $H_2$ it produces. This research showed that replacement of the WGS reaction with the CDH reaction could eliminate the emission of very large amounts of $CO_2$ and save huge amounts of water.

## 1. Development of catalytic dehydrogenation technology

Initial work on this topic began prior to the current contract with DOE. Our first publication on CDH was published in 2001 [1]. Fe-based alloy catalysts were developed that were very active for the decomposition of methane. These included Fe-Ni, Fe-Pd, and Fe-Mo with the effective ratio of Fe to Ni, Pd, and Mo approximately = 2/1. Initially, these were deposited on γ-$Al_2O_3$ and reduced in $H_2$ at 700°C to metallic Fe alloys that were predominantly face-centered cubic or austenitic [2, 3]. Following reduction, hydrogen is displaced from the reaction tube by an inert gas. Methane is then injected into the CDH reaction tube and decomposes on the surfaces of the Fe-alloy catalysts as the temperature is increased, releasing $H_2$, while C diffuses into the metallic alloy. The carbon then saturates and precipitates outward from the surfaces of the catalyst particles, forming multi-walled carbon nanotubes (MWCNT). As shown in Figure 1, the amount of $H_2$ production reaches a plateau of about 70 to 90 % between 650 and 800 °C [1]. The effective reaction is

$$CH_4 \rightarrow C_{MWCNT} + 2H_2 \qquad (1)$$

As shown in the lower half of Figure 1, ethane injected into the CDH reactor converts rapidly to methane at a temperature of approximately 450°C [4]; as the temperature increases above 450 °C, decomposition of the methane then proceeds via equation (1). The complete reaction for ethane is effectively that shown below.

$$C_2H_6 \rightarrow CH_4 + C_A + H_2 \rightarrow C_A + C_{MWCNT} + 3H_2\ , \qquad (2)$$

where $C_A$ is amorphous carbon. Above approximately 450 °C, all of the ethane has been converted to methane and decomposition of methane then proceeds as described above. The CDH of propane is very similar to that of ethane [4]. Typical electron micrographs of the MWCNT are shown in Figure 2. The top micrograph is a typical SEM micrograph showing a ***SPAGHETTI-LIKE*** conglomerate of MWCNT. Such accumulations typically clog up CDH plug–flow reactors ½ to1 inch in diameter in about 8–10 hours. For this reason, we would like to

build a fluid-bed reactor that will enable continuous removal of MWCNT and injection of new or refurbished CDH catalysts.

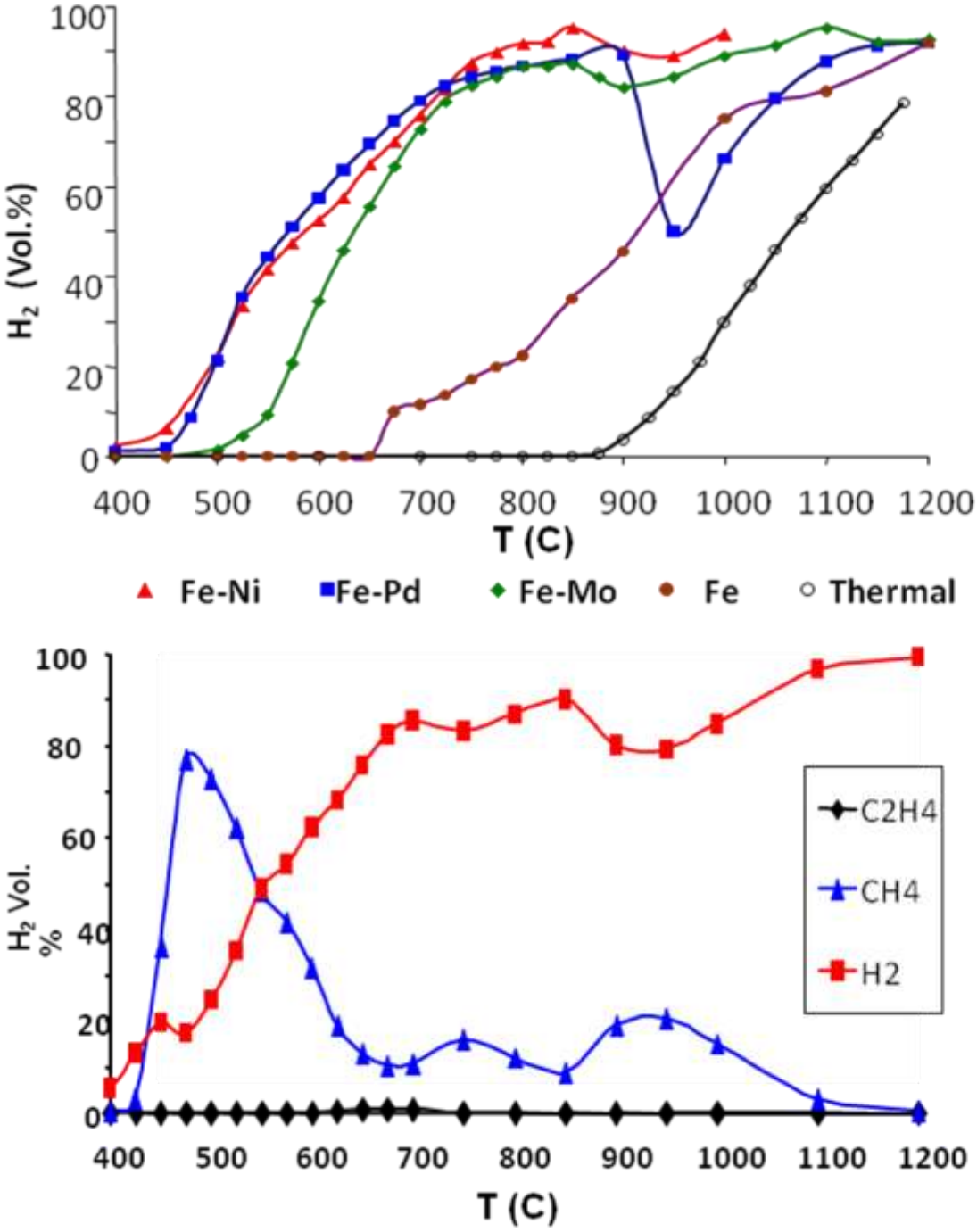


Figure 1. Top: CDH of methane. Bottom: CDH of ethane using an Fe-Ni catalyst.

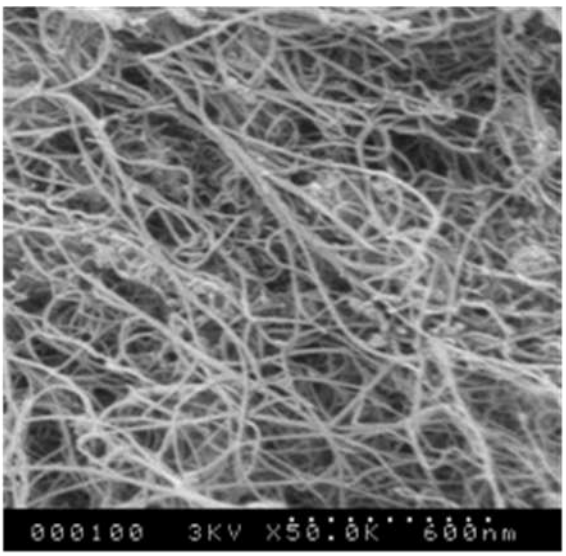


Figure 2. SEM (top) and TEM (bottom) micrographs of MWCNT produced by decomposing undiluted methane at 700 °C.

To initiate this task, a fluid-bed reactor one inch in diameter was developed by Dr. Naresh Shah and graduate student Shankang Ma with a switching mode reaction system for the semi-continuous production of hydrogen and carbon nanotubes by CDH of methane [8]. The reactor employed periodic removal of the spent catalysts and MWCNT and replenishment of fresh catalysts to the FB reactor. It was successfully demonstrated and ran in the semi-continuous mode for about 25–30 hours.

In future work, we plan to build a fully continuous fluid-bed CDH reactor of larger size that will continuously remove spent catalysts and MWCNT and replace them with new or refurbished catalysts for periods of days or weeks. This will of course be dependent on the availability of funding.

The typical structure of the MWCNT can be seen in the high resolution TEM micrograph shown in the lower half of Figure 2. The MWCNT consist of 8 – 10 concentric graphene tubes that typically have outer diameters of about 10-11 nm covered with a thin layer (~1-2 nm) of amorphous carbon and inner diameters of about 5-6 nm. The amorphous carbon can be removed by a cleaning process in a dilute nitric acid solution.

## 2. Catalytic dehydrogenation of liquid hydrocarbons

In addition to CDH of hydrocarbon gases, there was also interest in CDH of hydrogen-rich liquids, since cars and other vehicles are obviously designed to carry liquid fuels. Our research in this area was led by Yuguo Wang, a Postdoctoral Student at the University of Kentucky. Stacked-cone carbon nanotubes (SC-CNT) were used as the support for Pt and Pd nanoparticle catalysts for partial dehydrogenation of cyclohexane and methylcyclohexane, which produced pure hydrogen and aromatics. The aromatic from cyclohexane was benzene, which is a pollutant. However, CDH of methyl-cyclohexane produces hydrogen and toluene, which is a more desirable by-product. The results showed that a 0.25 wt % Pt/SC-CNT catalyst has the same catalytic activity and selectivity to produce aromatic products and hydrogen as a commercial 1 wt % $Pt/Al_2O_3$ catalyst [6]. Even 0.1 wt % Pt/SC-CNT showed high reaction activity for the dehydrogenation of cyclohexane and methylcyclohexane, and this catalyst also had the highest turnover number (TON) for hydrogen production. Transmission electron microscopy established that the mean diameter of the Pt nanoparticles dispersed on the SC-CNT remained approximately 1−2 nm even after the cyclohexane dehydrogenation reaction ran for 8-10 hours. Pd supported on SC-CNT was not nearly as effective as Pt/SC-CNT for the dehydrogenation of cyclohexane and methylcyclohexane.

SC-CNT with a BET surface area of ~280 $m^2/g$ were also used as the support for Pt catalysts used for partial dehydrogenation of tetralin and decalin to produce pure hydrogen and naphthalene. At 240 °C, dehydrogenation of decalin produces hydrogen, tetralin, and naphthalene. The small amount of tetralin present in the products compared with the amount of naphthalene produced indicates that the dehydrogenation of decalin to tetralin is slower than the dehydrogenation of tetralin [7].

## 3. Coupling Fischer-Tropsh Synthesis and Catalytic Dehydrogenation

Increasing fuel prices, coupled with decreasing supplies of petroleum in the U.S. and fuel security concerns have led to increasing interest in producing large amounts of liquid hydrocarbon fuels by Fischer-Tropsch synthesis (FTS) using syngas produced from our most abundant fossil fuel, coal. Unfortunately, the syngas produced by coal gasification has too little $H_2$ to produce liquid fuels by FTS. The traditional method of producing the additional $H_2$ required has been to utilize the water-gas shift (WGS) reaction.

$$H_2O + CO \rightarrow H_2 + CO_2 \quad (1)$$

However, as we showed in a recent publication [8] and a new paper [9] that has not yet been published, using the CDH reaction instead of the WGS reaction to produce the amount of $H_2$ required for a 50,000 barrel per day FTS plant could avoid the emission of thousands of tons of $CO_2$ emissions and save millions of gallons of water. A schematic diagram of the proposed configuration of such a plant is shown below.

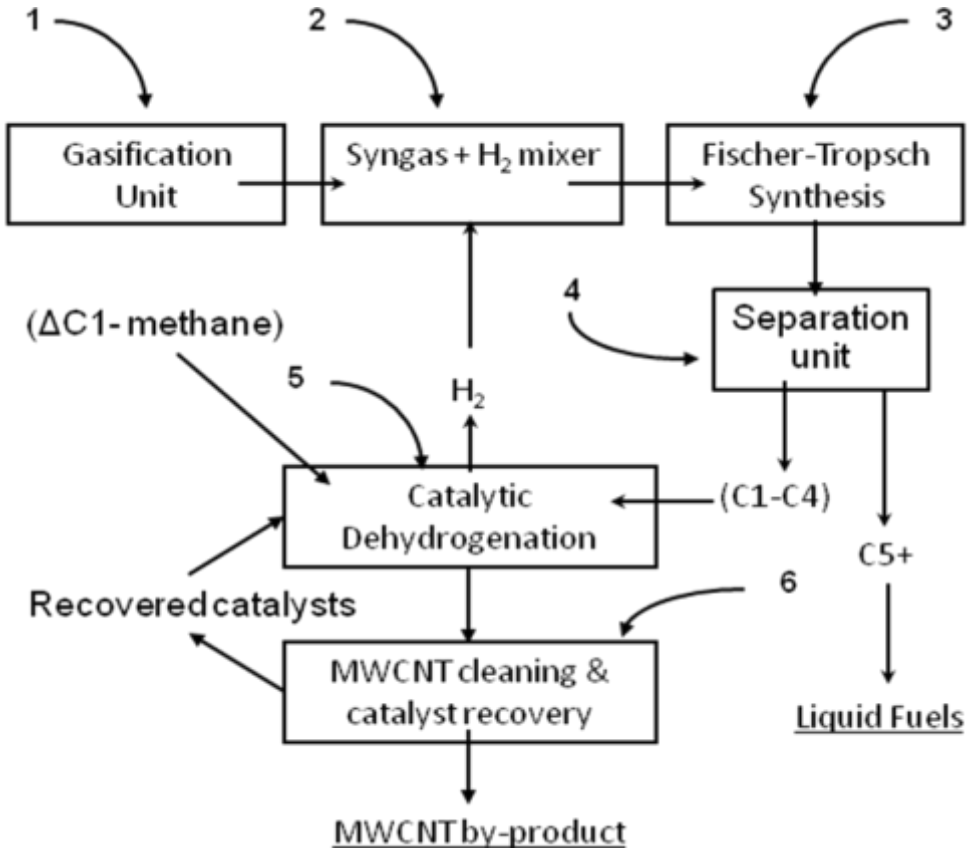


Figure 3. Schematic diagram of a Fischer-Tropsch Synthesis – Catalytic dehydrogenation (FTS-CDH) liquid fuel production facility.

To test this concept, 26 experimental FTS data sets were obtained from 10 different publications selected from the literature [8, 9]. Figure 4 shows the results obtained for the

$H_2$/CO ratios by combining FTS with CDH of the (C1 – C4) products (methane, ethane, propane, etc.) of FTS for the 26 FTS data sets used. All of the FTS data were produced using Co FTS catalysts. Fe FTS catalysts are not appropriate because Fe is an excellent catalyst for the WGS reaction, which we want to avoid.

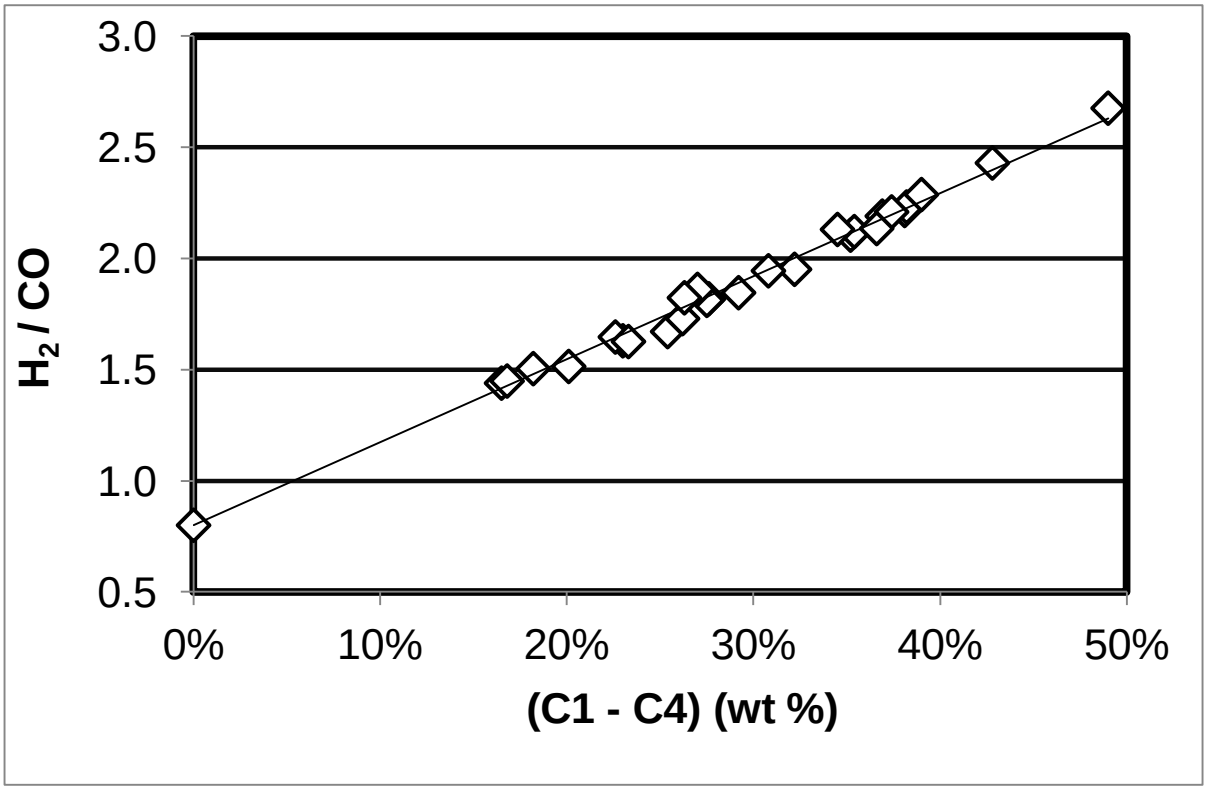


Figure 4. $H_2$/CO ratios achieved by adding the $H_2$ produced by CDH of the FTS (C1-C4) products to a syngas with an initial $H_2$/CO = 0.8.

For simplicity, it was assumed that the initial $H_2$/CO ratio of the syngas leaving the Gasification Unit was either 0.6 or 0.8. The 26 FTS data sets taken from 10 different publications [8, 9] were again used as examples to test the FTS-CDH concept. The equations used to calculate the weight percentages of $H_2$ and multi-walled carbon nanotubes produced by CDH of the (C1-C4) products of FTS and the $H_2$/CO molar ratios are available in both references [8] and [9] and will not be repeated here. The results of separating the gaseous hydrocarbon FTS products (C1-C4), directing them to the CDH reactor, and mixing the resulting $H_2$ with the incident syngas are shown in Figure 4 [8]. It is seen that for an initial $H_2$/CO ratio of 0.8, all of the $H_2$/CO ratios are raised to 1.49 or higher and half are raised to 1.99 or higher.

Reference [9] carries the concept further by adding $H_2$ produced by CDH of methane derived from natural gas to the syngas. If hydro-fracking continues to expand, this should be an economical method of avoiding all $CO_2$ emissions during the production of liquid fuels from coal

and natural gas. Figure 5 illustrates the effect this would have on the $H_2$/CO ratios [9] for a syngas with an initial $H_2$/CO ratio of 0.6.

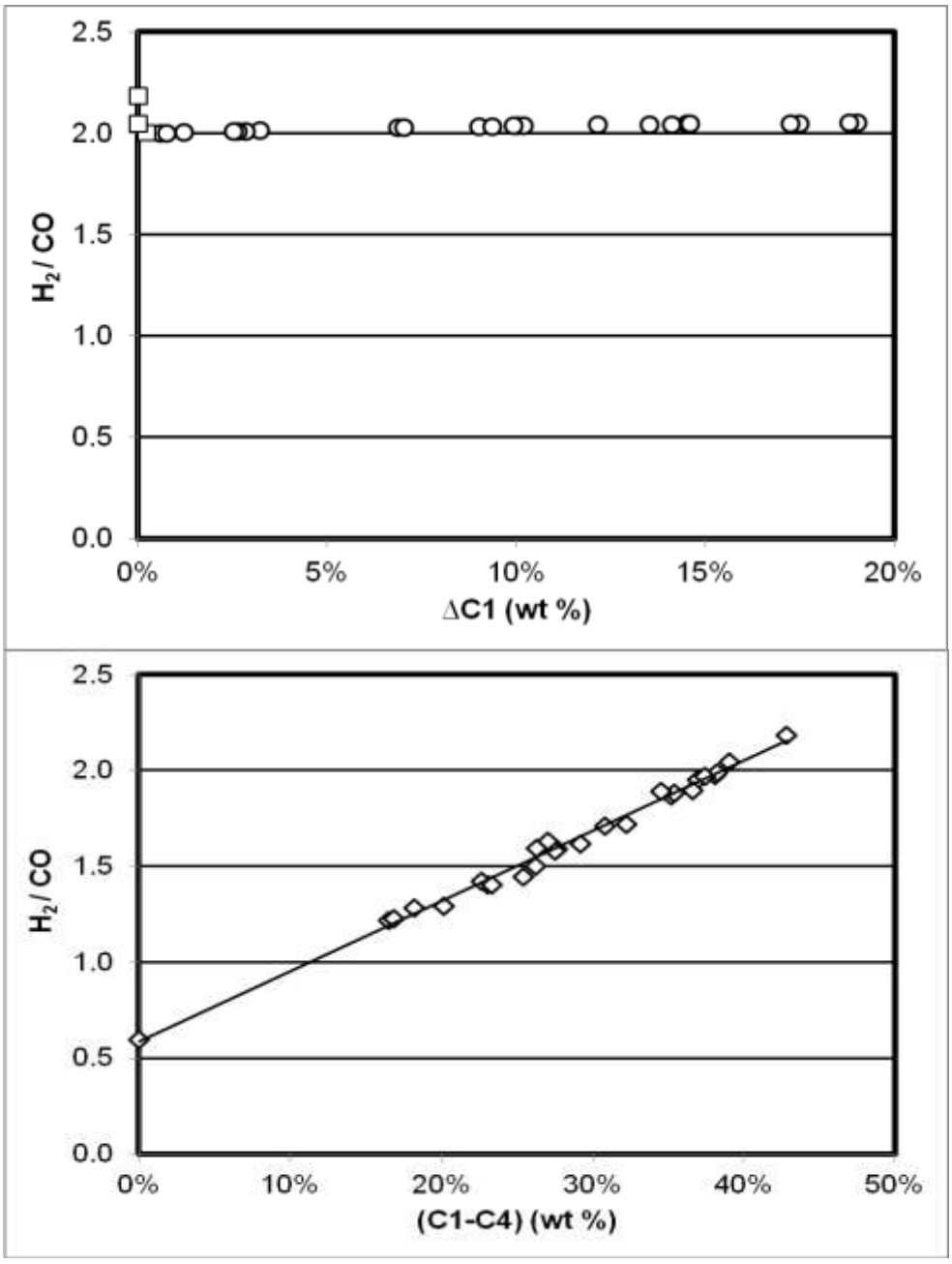


Figure 6. (Bottom) $H_2$/CO ratios achieved by adding the $H_2$ produced by CDH of the FTS (C1-C4) products to a syngas with an initial $H_2$/CO = 0.6.

(Top) $H_2$/CO ratios achieved by adding the $H_2$ produced by CDH of the wt % of methane shown on the abscissa to that produced by CDH of the FTS (C1-C4) products alone.

Table 1 gives a summary of the calculated amounts of products and environmental savings that could be achieved for a 50,000 bbl/day plant by combining Fischer-Tropsch synthesis,

catalytic dehydrogenation, and methane injection (FTS–CDH–MI ), relative to a conventional FTS plant. The results shown in the table below are the averages calculated for all 26 FTS data sets used in this model [8].

**Table 1. Summary of the Amounts of Products and Environmental Savings for a 50,000 barrel/day FTS-CDH-MI plant relative to a conventional FTS plant**

| **Products** | **Weight (tons/day)** |
|---|---|
| Wt. 50K bbl oil | 7,229 |
| Total all products | 11,640 |
| Total $H_2$ | 1,000 |
| Total MWCNT | 2,930 |
| **Environment savings** | **Amounts/day** |
| $CO_2$ emissions avoided | 22,007 tons/day |
| $H_2O$ saved | 9,002 tons/day |
| $H_2O$ saved | 2,160,436 gal/day |

Finally, it should also be noted that the FTS-CDH and FTS-CDH-MI processes are energy efficient processes. Using "Transition State Theory" [10, 11], the "activation enthalpy" for CDH reactions using the three different Fe-alloy catalysts was shown to range from 30 to 37 kcal/mol [8]. It is also shown in reference [8] that this energy could be provided from heat released by the syngas during cooling from gasification temperatures (~1,500-1,600 K) to the temperature of the CDH reaction (~1,000K).

**Students who contributed significantly to the Catalytic Dehydrogenation and Fischer – Tropsch synthesis + Catalytic Dehydrogenation (FTS-CDH) research.**

1. **Devdas Panjala** was a Postdoctoral Scholar at UK from 2001 to 2005. He conducted our initial research on catalytic dehydrogenation (CDH) of hydrocarbon gases under the direction of Prof. Naresh Shah. Dr. Panjala currently works at ConocoPhillips.
2. **Wenqin Shen** earned her PhD in Chemical Engineering at UK in 2009. She published several papers on catalytic dehydrogenation (CDH) using nanoscale, monodisperse Fe-Ni catalysts on a Mg-based support. The catalyst maintained high activity for dehydrogenation of methane for periods of up to 20 hours. She used a Mg-based support, which enabled easy cleaning of the MWCNT produced by the CDH process. She is now employed by Sud-Chemie in Louisville, KY.
3. **Abhijit Bhagavatula** will complete his PhD in Chemical Engineering at UK in 2013. His research topic is gasification of coal, biomass, and coal-biomass mixtures. He has made presentations at two AIChE meetings and is currently preparing two papers for publication and writing his PhD thesis.

4. **Artur Braun** was a Postdoctoral Student at the University of Kentucky from 2001 to 2005, during which time he conducted small angle x-ray scattering (SAXS) research on the growth of cobalt nanoparticle catalysts in silica aerogels. He is now the Group Leader of the Laboratory for High Performance Ceramics, in Dübendorf, Switzerland.
5. **Yuguo Wang** was a Postdoctoral Student who conducted experiments on CDH of liquid hydrocarbons and published several papers on that topic during the time he spent at UK (2004 – 2006). He is now employed at Aramco.
6. **Xuebei Shi** conducted preliminary experiments on CDH of methane from Fischer-Tropsch synthesis to hydrogen and carbon nanotubes and developed promising Fe-Mn CDH catalysts supported on Mg(Al)O catalysts. She is now working on her PhD thesis.
7. **Shankang Ma** assisted Prof. Naresh Shah in building and testing a semi-continuous fluid-bed CDH reactor. He is now working on a Ph.D. in Pharmacology at the University of Louisville.

**Patents:**

Two patents have been awarded for this research [12, 13].

**References:**


1. Gerald P. Huffman, Naresh Shah, and Devdas Panjala, "Hydrogen production by catalytic decomposition of methane", *Energy & Fuels*, **15** (2001) 1528-1534.
2. Naresh Shah, Sidharta Pattanaik, Frank E. Huggins, Devadas Panjala, and Gerald P. Huffman, "XAFS and Mössbauer spectroscopy characterization of supported binary catalysts for non-oxidative dehydrogenation of methane", *Fuel Processing Technology*, **83** (2003) 163-174
3. A. Punoose, N. Shah, G.P. Huffman, and M.S. Seehra, "X-ray diffraction and electron magnetic resonance studies of M/Fe/$Al_2O_3$ (M=Ni, Mo, and Pd) catalysts for $CH_4$ to $H_2$ conversion", *Fuel Processing Technology*, **83** (2003) 263-274.
4. N. Shah, Y. Wang, D. Panjala, and G.P. Huffman, "Production of pure hydrogen and carbon nanostructures by catalytic non-oxidative dehydrogenation of ethane and propane", *Energy & Fuels*, **18** (2004) 727-736.
5. Naresh Shah, Shankang Ma, Yuguo Wang, and Gerald P. Huffman, "Semi-continuous hydrogen production from catalytic methane decomposition using a fluidized-bed reactor", *International J. Hydrogen Energy*, **32** (2007) 3315-3319.
6. Yuguo Wang, Naresh Shah, and Gerald P. Huffman, "Pure hydrogen production by partial dehydrogenation of cyclohexane and methylcyclohexane over nanotube supported Pt and Pd catalysts", *Energy & Fuels*, **18** (2004) 1429-1433.
7. Yuguo Wang, Naresh Shah, Frank E. Huggins, and Gerald P. Huffman, "Hydrogen production by catalytic dehydrogenation of tetralin and decalin over stacked cone carbon nanotube-supported Pt catalysts", *Energy & Fuels*, **20** (2006) 2612-2615.
8. Huffman, Gerald P. "Incorporation of catalytic dehydrogenation into Fischer-Tropsch synthesis of liquid fuels from coal to minimize carbon dioxide emissions", *Fuel*, **90** (2011) 2671-2676.

9. Huffman, Gerald P., "Zero emissions of $CO_2$ during the production of liquid fuel from coal and natural gas by combining Fischer-Tropsch synthesis with catalytic dehydrogenation", *Fuel* (2013), http://dx.doi.org./10.1016 /j.fuel.2013.3.01054 , in the press.

10. Eyring, Henry. "The activated complex in chemical reactions", *J. Chem. Phys.* (1935) **3**:107–15.

11. Wynne-Jones, WFK and Eyring, Henry. "The absolute rate of reactions in condensed phases." *J. Chem. Phys.* (1935):**3.**

12. "Catalytic Conversion of Hydrocarbons to Hydrogen and High-Value Carbon", Naresh Shah, Devdas Panjala, and Gerald P. Huffman, U.S. Patent Number 6,875,417 B1, April 5, 2005.

13. "Incorporation of Catalytic Dehydrogenation into Fischer-Tropsch Synthesis to Significantly Reduce Carbon Dioxide Emissions," Gerald P. Huffman, Patent Number 8,309,616, November 13, 2012.

14. "Ostwald-Ripening of Cobalt Precipitates in Silica Aerogels? – An Ultra-Small Angle X-Ray Scattering Study", Artur Braun, Jan Ilavsky, Brian C. Dunn, Pete R. Jemian, Frank E. Huggins, Edward E. Eyring, and Gerald P. Huffman, *J. Applied Crystollography*, **38** (2004) 132-138.

**Energy efficient production of $H_2$ by electrolysis of water containing activated carbon (BP2000) and hydrothermally converted lignocellulosic biomass**

**M. S. Seehra, Department of Physics, WVU**

**Final Report through December 31, 2012.**

Our focus in this sub-task under the contract # DE-FC-26-05NT42456 was on investigating and developing the energy-efficient electrochemical production of $H_2$ gas at laboratory scale using carbons, coals and biomass. Since production of $H_2$ by conventional water electrolysis has an efficiency of only about 30 %, considerably lower than the nearly 80 % efficiency of producing $H_2$ by steam reforming of methane [1], our focus was on improving this efficiency of the electrochemical process of producing $H_2$. The results obtained under this program have been published in three significant peer-reviewed research papers [2-4] which can be accessed for complete details. The results are also detailed in three M.S. theses of my graduate students [5-7]. A brief summary of these results is given below.

.

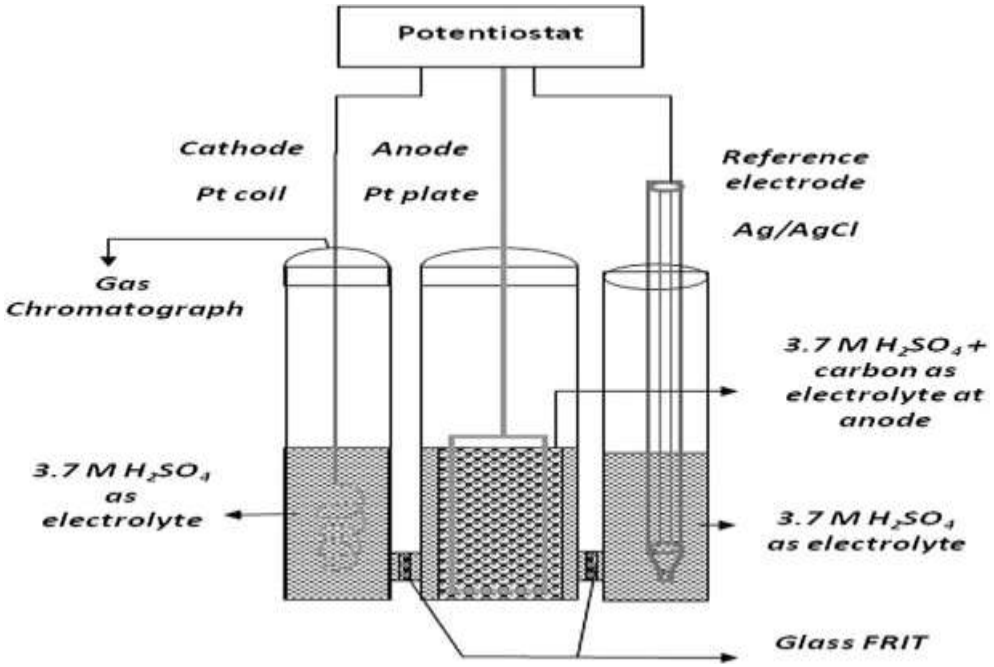


Fig. 1 – A schematic diagram of the three-electrode cell with Pt plate as anode (surface area 6.8 $cm^2$) and Pt coil as cathode (surface area 2.5 $cm^2$). A magnetic stirrer was used to stir the contents of the anode (from Ref. [2]).

The schematic diagram of the experimental set up used in these experiments is shown in Fig. 1. In standard water electrolysis using only the electrolyte (acidic or alkaline) in the anode, hydrogen evolution does not begin till a voltage of about 2 V is applied (see Fig.2). Following up on the initial experiments of Coughlin et al [8] using carbon assisted water electrolysis in which carbon is added to the anode, we tested a variety of carbons [2,3] to produce hydrogen. It was

found that high surface area commercial carbon BP2000 gave the best results. In agreement with the theoretical predictions [8], $H_2$ evolution was observed at applied voltages as low as 0.5 V (see Fig.2) with carbon BP2000 added to the anode. It was also established that the net reaction is : $C(s) + 2H_2O$ -------> $CO_2(g) + 2H_2(g)$ with pure $CO_2$ evolved at the anode and pure $H_2$ evolved at the cathode. The process is really then electrochemical gasification of carbon in water occurring at room temperature with the concurrent evolution of pure hydrogen produced at the cathode.

In order to quantify the efficiency of this process, we measured current $I_o$ in the circuit and the time $t_H$ needed to produce the same amount of $H_2$ (1000 units of area under the hydrogen peak observed in the gas chromatograph) for each applied voltage $E^o$. From these quantities, we computed the hydrogen evolution rate $R_H = 1/t_H$ and $A_H = R_H / E^o I_o$, the later representing the amount of hydrogen produced per watt.hr of energy used. The plots of current, $R_H$ and $A_H$ vs. $E^o$ for three cases are shown in Fig. 2. These three cases are: (i) Just the electrolyte viz. 3.7M $H_2SO_4$ representing conventional water electrolysis; (ii) electrolyte plus BP2000 added [3]; and electrolyte plus hydrothermally converted cellulose [4].

The first point to note is that in water electrolysis without using any carbon, measurable $R_H$ is observed only for $E^o > 2$ V. For better efficiency, we need both higher $R_H$ and higher $A_H$. In Fig. 2, the dotted lines are drawn to compare magnitudes of $R_H$ and $A_H$ at $E^o = 2.6$ V for water electrolysis with the magnitudes of these quantities at $E^o = 0.7$ V where we have exactly the same evolution rate $R_H$. However, with the use of carbons, the magnitude of $A_H$ is a factor of about five higher. This shows that with the use of activated carbon BP2000, the amount of hydrogen produced per watt-hr of energy used is a factor of five higher; with the use of hydrothermally treated cellulose, $A_H$ is a factor of about four larger.

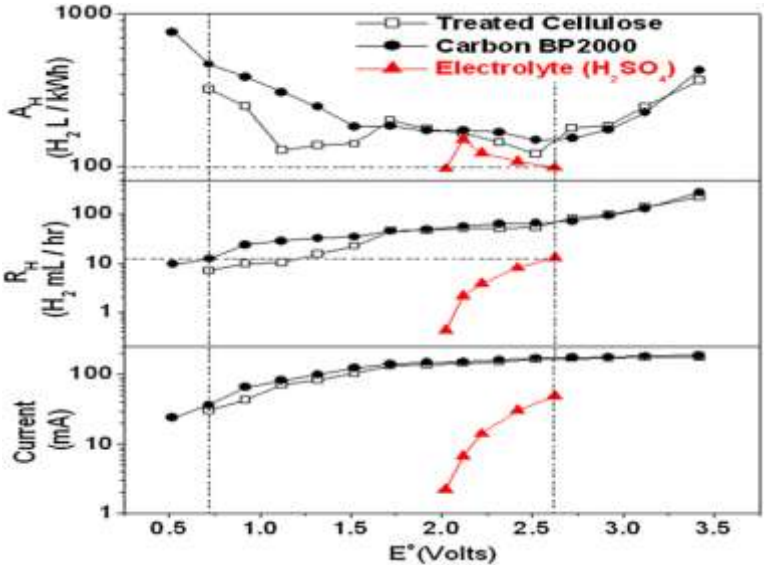


Fig. 2 – The variations of $R_H$, $A_H$ and current $I_o$ with change in applied potential $E^o$ (with respect to standard hydrogen electrode) for the three cases listed on the figure.

## Comparative Energy Analysis

From the discussion given in our publication [4], one gasoline gallon equivalent (GGE) equals 33.4 kWh of electricity which in turn equals 10.1 $m^3$ of $H_2$ gas at standard temperature and pressure (STP). According to this equivalence, one KWh of electricity equals 300 L (liters) of hydrogen, i.e. use of one KWh of electricity must produce 300 L of $H_2$ @ STP for 100% energy efficiency. This equivalence is used here to determine the energy efficiencies of our electrochemical processes for producing $H_2$ using carbon BP2000 and hydrothermally pre–treated cellulose.

For electrolyte only representing water electrolysis in Figs. 2 , $E^o > 2$ V is needed to start the reaction, reaching close to saturation at $E^o$ =2.6 V. At this voltage in Fig. 2, $R_H$ is about 15 mL/h and $A_H$ equals 100 L per kWh of $H_2$ produced. As noted earlier, if process were 100% energy efficient, $A_H$ = 300 L/kWh should have been produced. Thus water electrolysis is only about 33% (100/300) efficient, in agreement with the 30% efficiency reported in the detailed analysis of Rosen and Scott comparing various processes for producing $H_2$ [1].

In Fig. 2, the horizontal dotted line is drawn to show that using commercial carbon BP2000 with surface area of 1500$m^2$/ g, the same $R_H$ is obtained at applied voltage $E^o$ = 0.7 V using carbon BP2000 as obtained by applying $E^o$ = 2.6 V in conventional water electrolysis. However, at $E^o$ = 0.7 V with carbon BP2000, $A_H$ = 450 L/kWh of $H_2$ is produced, resulting in energy efficiency of 150% (450/300) compared to about 33% for conventional water electrolysis. This nearly five-fold improvement in energy efficiency over conventional water electrolysis is coming from the extra electrons provided by the use of carbon BP2000. This is understandable since oxidation of carbon once initiated is an exothermic reaction. This electrochemical gasification however occurs at room temperature and it does produce $CO_2$ at the anode but it is well separated from the $H_2$ produced at the cathode. The cost of commercially available BP2000 is not included in the above energy analysis. All carbons are effective in this process but the $H_2$ evolution rate and efficiency factor $A_H$ depend on the particle size and surface area of a carbon [3]. So the efficiency will depend on the properties of the carbon used in the process.

In Fig. 2, the data of $H_2$ production using hydrothermally treated cellulose in addition to carbon BP2000 is also included. As compared to the data for BP2000, with treated cellulose, somewhat lower $A_H$ = 350 L/kWh is obtained at $E^o$ = 0.7 V with essentially similar evolution rate $R_H$ of $H_2$. This yields slightly lower energy efficiency of about 120% (350/300) which is still a factor of four improvement over conventional water electrolysis. As before, the above estimate of energy efficiency does not include the costs associated with producing hydrothermally treated cellulose. Untreated microcrystalline cellulose was found to be inactive in producing hydrogen.

## Conclusions

The several fold increase in energy efficiency noted above to produce pure hydrogen in carbon-assisted water electrolysis vis-a-vis conventional water electrolysis is the major result of this project. Pure $CO_2$ is produced at the anode from the oxidation of carbon but it is well separated from pure $H_2$ produced at the cathode. With hydrothermally treated cellulose, about a

four–fold increase in energy efficiency is obtained but no $CO_2$ could be detected at the anode in this process; so further work is needed to understand the chemistry of this reaction. These major improvements in energy efficiencies should make these processes to produce hydrogen very competitive with hydrogen produced using steam reforming of methane and coal gasification. More complete details of the experimental procedures and results are available in references 2 through 7 quoted below.

## References

1. M. A. Rosen and D.S. Scott, Comparative efficiency assessments for a range of hydrogen production processes. Int. J. Hydrogen Energy, 23, 653-659 (1998).

2. M.S. Seehra, S. Ranganathan and A. Manivannan: Carbon-assisted water electrolysis: an energy-efficient process to produce pure $H_2$ at room temperature, Appl. Phys. Lett. 90, 044104 (3 pages), 2007. Erratum: Appl. Phys. Letters 92, 239902(2008).

3. M. S. Seehra and S. Bollineni: Nanocarbon boosts energy-efficient hydrogen production in carbon-assisted water electrolysis, Int. J. Hydrogen Energy. 34, 6078-6084 (2009).

4. M. S. Seehra, L. P. Akkineni, M. Yalamanchi, V. Singh, and J. Poston : Structural characteristics of nanoparticles produced by hydrothermal pretreatment of cellulose and their applications for electrochemical hydrogen generation, International J. Hydrogen Energy, 37, 9514-9523, (2012),

5. Sukanya Ranganathan: Carbon assisted electrolysis of water to produce hydrogen at room temperature. M. S. thesis, 2007, West Virginia UniversityShilpa Bollineni: Hydrogen production via carbon- assisted water electrolysis at room temperature: Effects of catalysts and carbon type. M. S. thesis, 2008, West Virginia University.

7. L. P. Akkineni : Hydrothermal pretreatment of biomass samples for producing energy efficient hydrogen electrochemically. M. S. thesis, 2011, West Virginia University.

8. R. W. Coughlin and M. Farooque. Electrochemical gasification of coal: simultaneous production of hydrogen and carbon dioxide by a single reaction involving coal, water and electrons. Ind. Eng. Chem. Process Des. Dev. 19, 211 (1980).

Graduate students **Sukanya Ranganathan**, **L. P. Akkineni**, and **A. Manivannan,** and Postdoctoral student **Vivek Singh** all made significant contributions to this research project.

# Structural and Electronic Characterization of Catalysts for Coal-Biomass Conversion to Transportation Fuels

F. E. Huggins[1], N. Shah[1], G. P. Huffman[1] and M. S. Seehra[2]
[1]CFFS & Department of Chemical and Materials Engineering, University of Kentucky
[2]Department of Physics, West Virginia University

*Final Report: December 31, 2012*

## A. Introduction:

The goal of this project, administered and carried out by the PI's listed above from the University of Kentucky (UK) and West Virginia University (WVU), was to provide structural and electronic characterization of catalysts developed under this research contract. Structural characterization was achieved at various stages of the reactions and correlated with the products obtained in the catalytic reactions. Many graduate and postdoctoral students received training in the use of these structural characterization techniques in catalysis research.

The leaders for this part of the research effort were Dr. Frank Huggins (UK) and Dr. Mohindar Seehra (WVU), both of whom have had extensive experience in catalyst characterization over the past 25 years. Catalysts were investigated with respect to the following reactions: Fischer-Tropsch synthesis; catalytic dehydrogenation of gaseous hydrocarbons; the water-gas-shift reaction; and methanol synthesis.

## B. Analytical techniques used for characterization of catalysts:

The list of analytical techniques employed for the structural/electronic characterization of the catalysts is given below. Techniques 1 through 7 were used by the Seehra group at WVU and techniques 8 through 11 were used by the Huggins group at UK.

1. X–Ray Diffraction (XRD): Chemical phases; Crystallite size; Quantification of different phases using Rietveld refinement.
2. Temperature Programmed Reduction (TPR): Temperature of reduction of oxides; Electronic states; Interaction of the catalysts with support.
3. BET surface area measurements of catalyst/support systems
4. Thermogravimetry/Differential Scanning Calorimetry (TGA/DSC): Thermal stability, phase changes, moisture loss and oxidation/reduction.
5. Electron Magnetic Resonance (EMR): Electronic states of magnetic ions in catalysts/support systems.
6. SQUID Magnetometry: Electronic states of magnetic ions & their interactions and concentrations.
7. Infrared/Photoacoustic Spectroscopy: Structural features, complementary to XRD.
8. *Transmission electron microscopy (TEM and STEM) for determining the shape and size distribution of the catalysts at the nm scale.
9. *Scanning electron microscopy (SEM) for lower resolution imaging and energy dispersive x-ray analysis.

10. $^{57}$Fe Mőssbauer spectroscopy for identification of Fe phases in catalysts at different stages of the reactions and for determining the distribution of Fe among different phases.
11. XAFS (x-ray absorption fine–structure) spectroscopy for determining electronic states and local structure of the key elements of the catalysts before and after the reactions. The XAFS spectroscopy was conducted largely in collaboration with the Synchrotron Catalyst Consortium at the National Synchrotron Light Source (NSLS), Brookhaven National Laboratory (NY), which allowed us to take advantage of the special *in situ* apparatus available there.

---

*Dr. Naresh Shah (UK, CFFS) provided valuable assistance in obtaining the TEM and SEM data.

**C. Specific Projects Investigated:**

Below we summarize some of the specific projects for which the UK and WVU analytical groups collaborated in investigating catalyst structures during the course of this contract. The names of the collaborators and lists of several publications containing structural characterization data are included are given below. It is impractical to give the results for all the projects listed here. Therefore, we have chosen to provide characterization details for just a few in section **C.** and **D.** Specific projects are as follows:

**C.1---Cu-based catalysts for methanol to $H_2$ conversion** (collaboration with Wender, Tierney et al, Pittsburgh)

1. ACS Preprints 52, 411 (2007),
2. J. Appl. Phys. 101, 09H107 (2007)
3. J. Appl. Phys. 103, 0D104 (2008)

**C.2-- Pd/Ceria/$SiO_2$ aerogel catalysts for water-gas shift (WGS) catalysis**
(collaboration with Eyring, Ernst, Pugmire et al, Utah)

1. Energy & Fuels 22,1439 (2008)
2. Chem. Mater. 18, 5144 (2006)
3. Chem. Mater. 17, 5183 (2005)

**C.3-- Co/$Al_2O_3$ and Co/$SiO_2$ catalysts for conventional and supercritical phase FT synthesis** (collaboration with Roberts et al, Auburn, and WVU )

1. Appl. Catal. A: General 285, 169 (2005);
2. ACS Preprints 50, 598 (2005).

**C.4 – Fe-Ni, Fe-Mo and Fe–Mn alloy catalysts for catalytic dehydrogenation of gaseous hydrocarbon from FT synthesis** ( UK-WVU collaboration)

1. ACS Preprints 52(2), 63 (2005);
2. Energy & Fuels 21, 3520 (2007);

3. Energy & Fuels 22, 3620 (2008);
4. Appl. Catal. A: General 351, 102 (2008).

**C.5--- Fe on SBA-15 or silica aerogels for FTS** (collaboration with Eyring, Ernst, Pugmire et al., Utah)

1. Appl. Catal A: General 278, 232 (2005);
2. Energy & Fuels 20, 2608 (2006);
3. Spectrochim. Acta A 72, 975 (2009).

**C.6 --- (K, Co, Cu, Pd) substituted iron aerogel catalysts for FTS and WGS catalysis** (collaboration with Eyring, Ernst, Pugmire et al., Utah)

1. Energy &Fuels, 22, 1439,( 2008)
2. Energy & Fuels, 23, 14 (2009)
3. Spectrochim. Acta A 76, 74 (2009).

**C.7 --- Fe:Al: Cu:K= 100:25:5:1.5 catalysts for FTS catalysis**
(collaboration with Eyring, Ernst, Pugmire et al., Utah ) ; Details and references given in Section D.

**C.8 --- (Cu,Zn)/Al2O3 catalysts for synthesis of alcohols;**
(collaborations with Roberts et al, Auburn)

**C.9 --- Nanoparticle catalyst systems**
(Collaborations with Roberts et al); in-house nanoparticle systems prepared at Auburn and UK, and investigated at UK and WVU. Included nanoparticles of Au, Pd, Ni, Fe, ($Fe_3O_4$, $Fe_2O_3$, NiO, $CeO_2$ and $Ni(OH)_2$). Some references on this work are given below.

1. Appl. Phys. Letters 90, 213102 (2007);
2. IEEE Trans. Magn. 43, 3091 (2007);
3. Appl. Phys. Letters 90, 213102 (2007);
4. IEEE Trans. Magn. 43, 3091 (2007);
5. J. Appl. Phys. 103, 07D524 (2008);
6. Solid St. Commun. 145, 192 (2008);
7. J. Phys. Condens.Matter. 20, 015218 (2008);
8. Energy & Fuels 21, 3520 (2007);
9. J. Appl. Phys. 99,08Q503 (2006);
10. J. Appl. Phys.111, 07B516 (2012);.
11. J. Phys. Condens. Matter, 24,076002 (2012);
12. Materials Letters,68, 347(2012);

**D.1 Synthetic doped amorphous ferrihydrite for Fischer-Tropsch synthesis (FTS) of fuels**

This catalyst system was synthesized and tested for FT synthesis by the Utah CFFS group, and characterized by the WVU-UK analytical team. The TEM micrographs of three samples viz. UT-1, UT-2 and UT-4 are shown in Fig. 1. UT-1 is the as-prepared catalyst based on the nominal composition of Fe:Al:Cu = 100:25:5 and dried at 100$^{o}$C. X-ray diffraction and IR spectroscopy showed the features similar to those of 2-line undoped ferrihydrite (FHYD) (FeOOH).n$H_2O$. However TEM shows flake-like morphology without any hint of diffraction fringes seen in the undoped sample. Hence this material is amorphous in nature most likely due to the substitutes of Al and Cu for Fe. This may also be the reason for its superior performance in FTS reactions. Details of the synthesis, structure and magnetic properties of UT-1 were published in Ref. 1 noted below.

UT-2 has the nominal composition of Fe:Al:Cu:K = 100:25:5:1.5 obtained by adding the promoter K to UT- 1 and it was calcined at 400$^{o}$C. Its x-ray diffraction and IR patterns are similar to that of UT-1. However in magnetic and EMR investigations, presence of an additional magnetic phase is clearly indicated. Since ferrihydrite nanoparticles are known to change to hematite when heated in air to 700$^{o}$C and to magnetite when heated in an inert gas, the magnetic phase is likely an iron oxide. The core shell structure of the UT-4

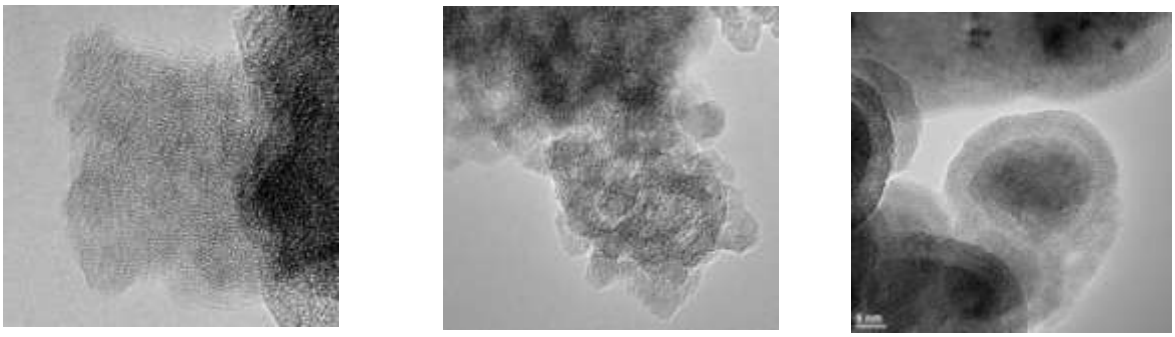

Fig. 1 TEM micrographs for the UT-1 (a), UT-2 (b) and UT-4 (c) samples (from left to right) obtained at the University of Kentucky.

sample, produced by borohydrite reduction of UT-2, is clearly evident in Fig 1(c), whereas in XRD, elemental Fe nanoparticles of 7 nm size and $\gamma$-$Fe_2O_3$/$Fe_3O_4$ oxide phase with particle of size = 6 nm were identified. Details of the various properties of UT-4 were published in Ref. 2 listed below.

Mössbauer spectroscopic analyses of the UT-1 and UT-2 original materials showed that their spectra consisted of two slightly asymmetric broadened lines consistent with the formation of ferrihydrite. These spectra are similar to those reported for iron aerogel and xerogel FTS catalysts that were discussed in detail in joint UK/Utah papers (Refs. 4, 5). In contrast, the Mossbauer spectrum of the reduced material, UT-4, shown in Figure 3, exhibited some remnant ferric oxide material, metallic iron, and an extremely broadened magnetic phase that was identified as an amorphous iron boride.

Results from the use of UT-1 and UT-2 as catalysts for FTS to produce fuels were recently published in Ref. 3 listed below. The conversion of syngas to liquid fuels was carried out over a period of 100 hrs in a fixed bed reactor at 265 $^{o}$C and 100 psig pressure. The product yields were

found to be superior to those obtained with the use of a commercial fixed bed catalyst. This enhanced catalytic activity was attributed to the amorphous nature of the ferrihydrite phase determined in UT-1 and UT-2. More details on the product yields in given in Ref. 3 and in the report from Utah.

**D.2. Investigation of mixed cobalt and iron oxide catalysts supported on silica and alumina:**

Many heterogeneous catalysts are prepared in oxide form (precursor catalyst) but are catalytically active only in a reduced or metallic state. This situation is found for important reactions such as Fischer-Tropsch synthesis (FTS), the water-gas-shift (WGS) reaction, and catalytic dehydrogenation (CDH) that were investigated in the Consortium research program. Although reduction may be the initial process when the precursor catalyst is exposed to reactant gases, there is generally an induction period of impaired catalytic activity until the catalyst becomes fully reduced and activated. This induction period is often minimized or avoided completely by a pre-reduction step prior to introducing the catalyst to the reactants. Furthermore, pre-reduction may offer better control over the reduction process leading to improved properties of the catalyst and enhanced initial activity. Under ideal circumstances, equilibrium would be reached between the catalyst's properties and the reactant gases at the desired conditions of the reaction and the catalytic activity would remain constant over time. Normally, however, one of the critical properties of the catalyst degrades with time of exposure to the reactant gases resulting in loss of catalytic activity.

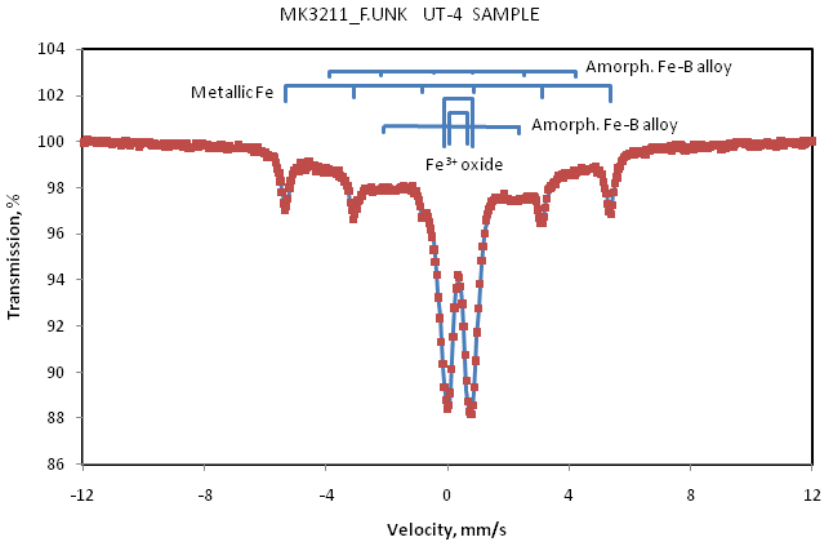


Figure 3: Mössbauer spectrum of borohydride-reduced catalyst sample, UT-4.

1. M. S. Seehra, V. Singh, X. Song, S. Bali and E. M. Eyring: Synthesis, structure and magnetic properties of non-crystalline ferrihydrite nanoflakes, J. Phys. Chem. Solids, 71, 1362-1366 (2010).
2. V. Singh, M. S. Seehra, S. Bali, E. M. Eyring, N. Shah, F. E. Huggins and G. P. Huffman: Magnetic properties of (Fe, Fe-B)/$\gamma$-$Fe_2O_3$ core-shell nanostructure, J. Phys. Chem. Solids. 72, 1373-1376(2011).

3. S. Bali, G. Bali, F. Huggins, M. S. Seehra, V. Singh, J. Hancock, R. Harrison, G. Huffman, R. Pugmire, R. Ernst, and E. Eyring: Synthetic doped amorphous ferrihydrite for the Fischer-Tropsch synthesis of alternative fuels, Industrial & Engg. Chem. Research, 51, 4515-4522 (2012).
4. S. Bali, F. E. Huggins, G. P. Huffman, R. D. Ernst, R. J. Pugmire, and E. M. Eyring, Iron aerogel and xerogel catalysts for Fischer-Tropsch synthesis of diesel fuel. Energy & Fuels, 23, 14-18, (2009).
5. F. E. Huggins, S. Bali, G. P. Huffman, and E. M. Eyring, Iron-oxide aerogel and xerogel catalyst formulations: characterization by $^{57}$Fe Mössbauer and XAFS spectroscopies, Spectrochim. Acta A. 76, 74-83, (2010).

In the current Consortium Research program, we have also investigated the states of iron, cobalt, and mixed cobalt-iron in a number of precursor catalyst materials supported on alumina or silica before and after reduction in various gaseous atmospheres at 500$^o$C. Catalyst materials of composition 100Fe, 67Fe33Co, 33Fe67Co, and 100Co, amounting to 15 wt% metal on the silica or alumina support were prepared. These materials were synthesized using principally incipient wetness methods. Techniques such as X ray-diffraction, cobalt X-ray absorption fine structure (XAFS) and iron Mössbauer spectroscopies (Figure 4), were used to identify specific details about the elements in these materials. The results, summarized in Tables 1 and 2, indicate that the reduction behavior of the Co-Fe oxides is quite different on silica compared to that on alumina, despite similar treatments.

Table 1. Summary of phases observed for calcined and reduced ($H_2$, 500$^o$C, 3 h) catalyst formulations supported on $SiO_2$.

| Composition | Calcined ($N_2$, 500$^o$C, 3 h) | Reduced ($H_2$, 500$^o$C, 3 h) |
|---|---|---|
| $Co_{100}$ | $Co_3O_4$ | Co metal (fcc) |
| $Fe_{33}Co_{67}$ | $Co_3O_4$ + $\alpha$-$Fe_2O_3$ | Co (fcc) + Fe-Co (bcc) alloy |
| $Fe_{67}Co_{33}$ | $Co_3O_4$ + $\alpha$-$Fe_2O_3$ | Fe-Co (bcc) alloy |
| $Fe_{100}$ | $\alpha$-$Fe_2O_3$ | $\alpha$-Fe metal (bcc) |

Table 2. Summary of phases observed for calcined and reduced ($H_2$, 500$^o$C, 3 h) catalyst formulations supported on $Al_2O_3$.

| Composition | Calcined ($N_2$, 500$^o$C, 3h) | Reduced ($H_2$, 500$^o$C, 3 h) |
|---|---|---|
| $Co_{100}$ | $(Co,Al)_3O_4$ | Co metal (fcc) |
| $Fe_{33}Co_{67}$ | $(Co,Fe,Al)_3O_4$ + spm $\alpha$-$Fe_2O_3$ | Co (fcc) + Fe-Co (bcc) alloy + $(Fe,Co,Al)_3O_4$ + spm $\alpha$-$(Fe,Al)_2O_3$ |
| $Fe_{67}Co_{33}$ | $(Co,Al)_3O_4$ + $\alpha$-$Fe_2O_3$ + spm $\alpha$-$Fe_2O_3$ | Fe-Co (bcc) alloy + $(Fe,Co,Al)_3O_4$ + spm $\alpha$-$(Fe,Al)_2O_3$ |

The differences in behavior of Fe and Co with respect to the two types of support can be attributed to the formation of spinel phases of composition $(Fe,Co,Al)_3O_4$ on the alumina. The formation of this phase severely retards reduction of iron and cobalt to metallic phases that are thought to be active in FTS. Furthermore, it would appear that iron is the major malefactor

because the formation of the spinel phase does not appear to be significant for pure cobalt and is most extensive for pure iron.

The effect of the reducing atmosphere and temperature was also investigated for some of these materials. Mossbauer spectroscopy was especially useful in this study because of the detailed information it gave regarding the forms of iron after reduction, which consist of carbides, oxides and metallic phases in varying proportions. Examples of the Mossbauer spectra are shown in Figure 5 and representative results for iron only compositions are shown schematically in Figure 6. Similar results were found for the iron in the mixed Fe-Co formulations.

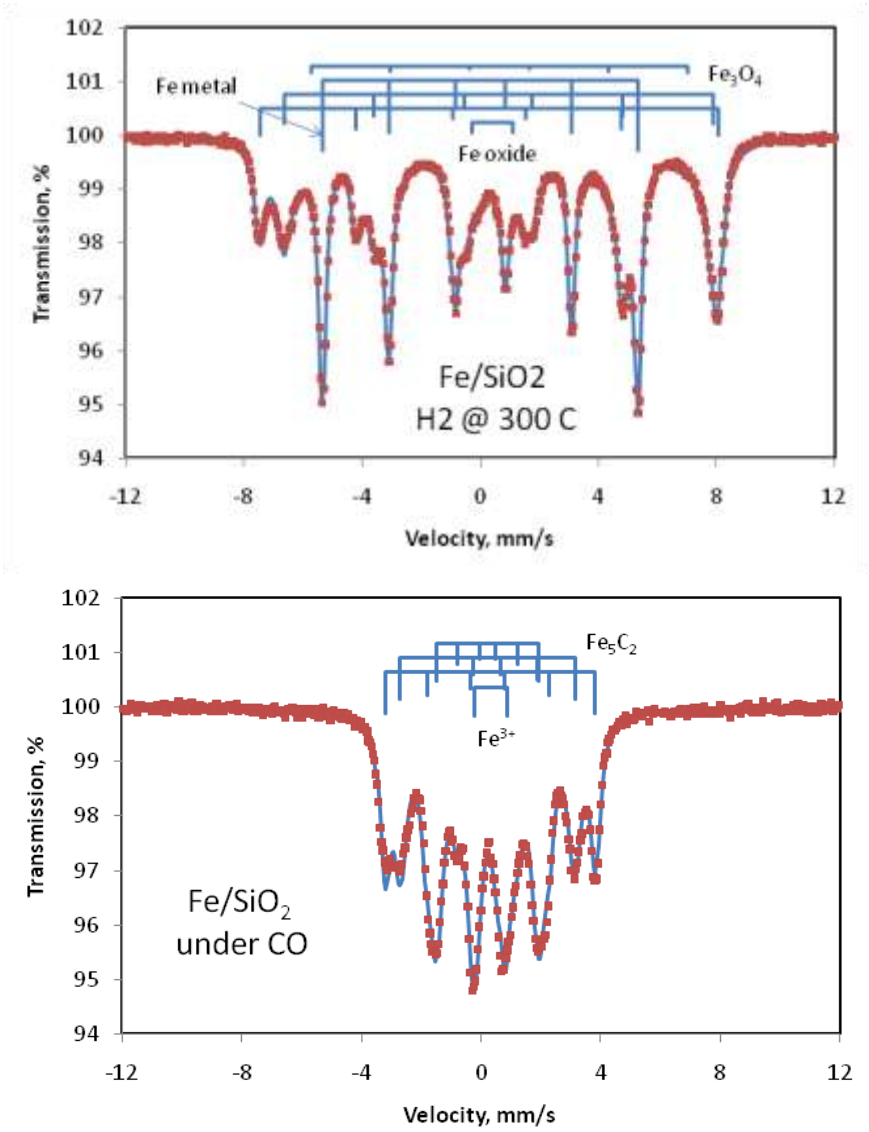


Figure 5. Mössbauer spectra of 15 wt% Fe on silica reduced in hydrogen (top) and CO (bottom).

From these investigations, we were able to conclude the following for the mixed Fe-Co formulations on silica and alumina that:

- Prior to reduction, the iron is entirely ferric;
- The silica-supported formulation is much easier to reduce than the corresponding alumina-supported formulation;
- $H_2$ is most effective for promoting formation of metallic Fe or Fe-Co alloys;
- CO promotes formation of iron carbide;
- Syngas, on the other hand, promotes magnetite and Co-containing spinel formation.

Interestingly, it was also found that under conditions of CO reduction it was the Hägg carbide ($Fe_5C_2$) that formed on silica, while it was cementite ($Fe_3C$) that formed on alumina.

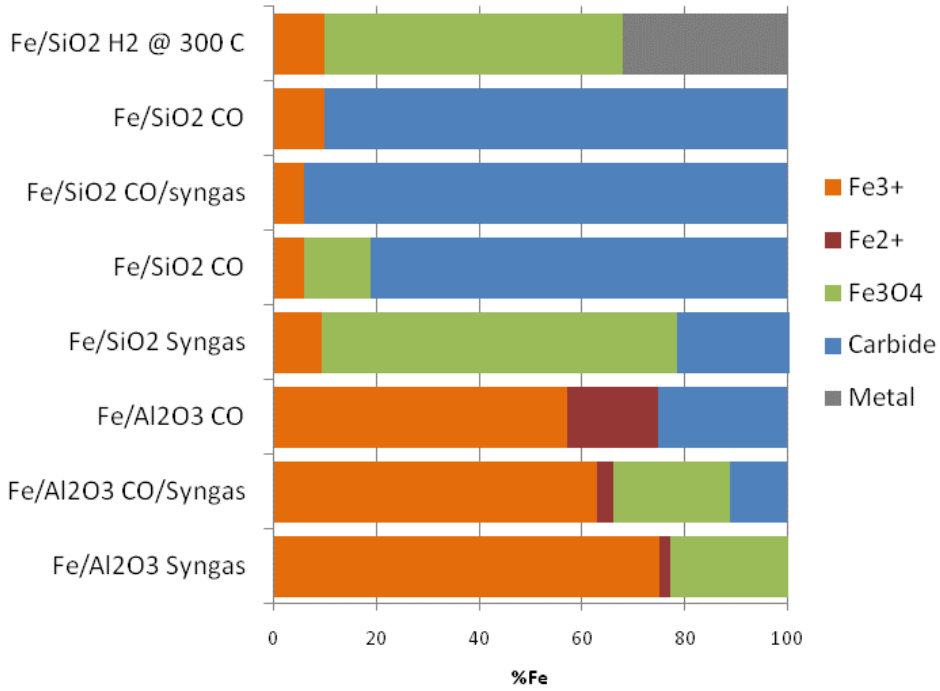


Figure 6: Summary of Mössbauer data obtained on the reduction of the catalyst formulation 0–15 wt% Fe on silica or alumina under different atmospheres; hydrogen, carbon monoxide, syngas, and CO followed by syngas. Phases detected include nonmagnetic ferric iron oxide ($Fe^{3+}$), nonmagnetic ferrous iron ($Fe^{2+}$), most probably $FeAl_2O_4$, magnetite ($Fe_3O_4$), iron carbide (carbide) and iron metal (metal).

**D.3. Characterization of Fe-Mn catalysts for catalytic dehydrogenation of alkanes**

A new suite of ($Fe_2Mn$) alloy catalysts designed for catalytic dehydrogenation (CDH) of alkanes were prepared by **Xuebei (Kathy) Shi** as part of her Ph.D. thesis research by loading $Fe(NO_3)_3{\cdot}9H_2O$ and $Mn(NO_3)_2{\cdot}4H_2O$ solutions onto several supports. These included $\gamma$-$Al_2O_3$, silica, Al-substituted MgO (2Mg(1Al)O), bulk MgO, and the zeolite, ZSM-5. Each catalyst was calcined overnight at 500°C in air and then used for CDH of methane at 700°C for a number of hours. The catalysts were characterized by Mössbauer spectroscopy and Mn XAFS

spectroscopy. The Mn s-ray absorption near-edge spectra (XANES) and EXAFS/RSF (radial structure functions) obtained from $Fe_2Mn$ on several different supports are shown in Figure 7.

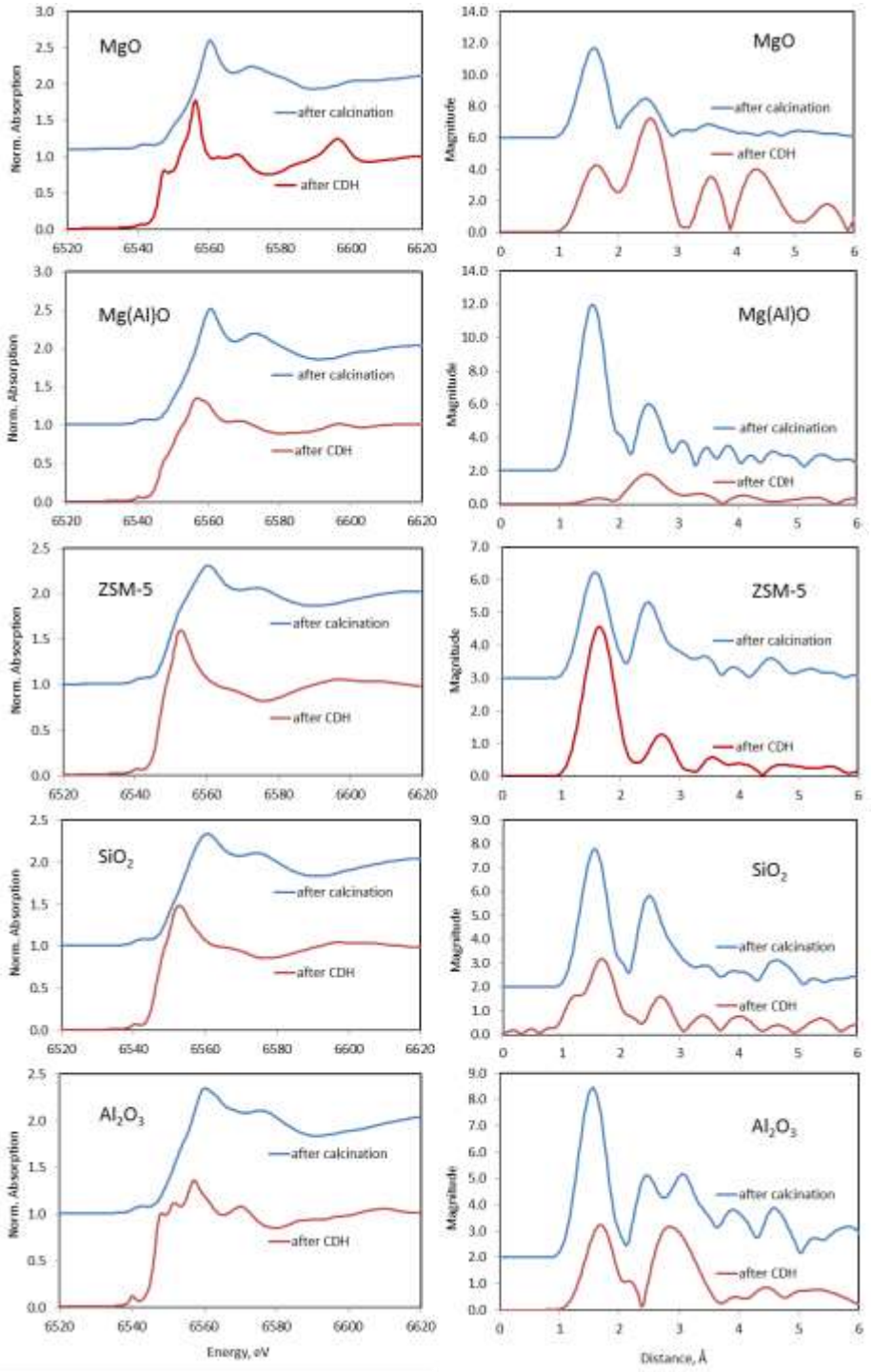


Figure 7. Mn XANES spectra (left) and EXAFS/RSF (right) spectra for ($Fe_2Mn$) catalyst supported on different oxide materials.

Results were compiled for the hydrogen production over time for the decomposition of the methane into hydrogen and carbon at 700°C using the different $Fe_2Mn$ catalysts. It was discovered that the $Fe_2Mn$/Mg(Al)O catalyst was by far the most effective for the decomposition of methane, exhibiting a higher conversion for a much longer length of time than any of the other formulations. The other four catalysts exhibited a "transitory" effect consisting of a short duration (<1 hour) burst of marginally accelerated hydrogen production before becoming relatively inactive. The interesting question of course is why did the Mg(Al)O support prove so effective for the CDH reaction, while the other supports were much less effective? This question was addressed by performing Mn XAFS spectroscopy.

The Mn XAFS spectra are shown in Figure 7. The spectra of Mn after calcination vary somewhat, but substantially greater differences exist after the CDH reaction. The Mn XANES spectra for all five formulations exhibit a shift of the absorption edge to lower energy in going from the calcined to the reacted state (after CDH). Such shifts indicate a significant reduction in the Mn oxidation state as a result of exposure to the conditions of the CDH reaction. For the catalyst on the MgO and $Al_2O_3$ supports, the actual phase appear to be (Mn, Mg)O and $MnAl_2O_4$, respectively, based on the XANES spectra for the after CDH reaction samples. Such forms contain manganese as $Mn^{2+}$. There are clearly major differences between the spectra for Mn on pure MgO compared to that for Mg(Al)O, especially after reaction.

Mossbauer spectroscopy showed that the iron in the calcined material consisted principally of ferrihydrite, along with lesser amounts of iron as α-$Fe_2O_3$, except for the ZSM-5 supported catalyst in which iron as α-$Fe_2O_3$ was dominant (Figure 8). After the CDH reaction, up to five different phases were indicated as present in the Mössbauer spectrum. Such phases consisted of γ-Fe(Mn), α-FeMn?, possibly Fe-Mn carbides, and remnant $Fe^{3+}$ oxide phases.

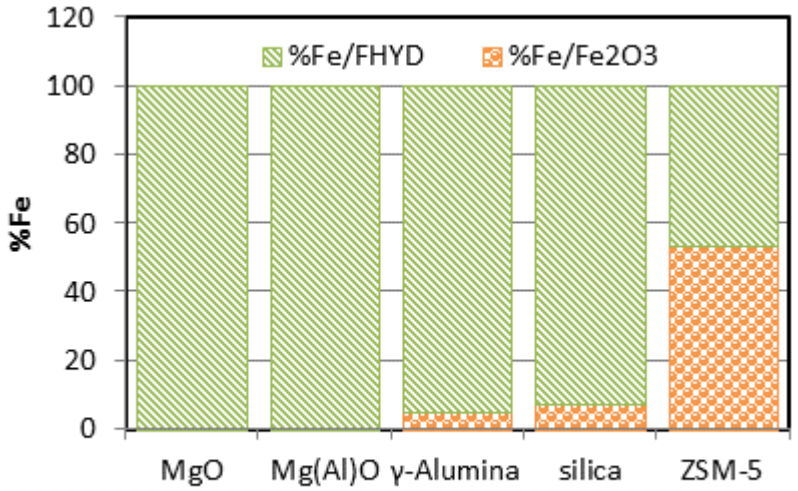


Figure 8: Distribution of iron between ferrihydrite and α-$Fe_2O_3$ for supported catalysts after calcination.

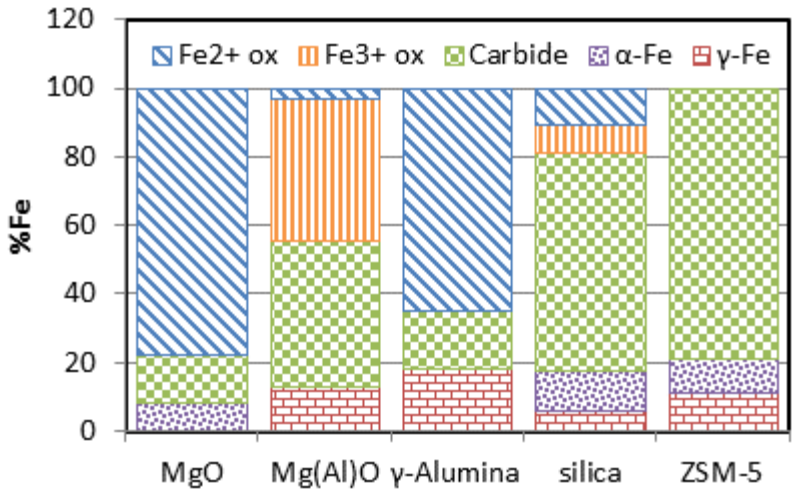


Figure 9: Distribution of iron among γ-Fe, α-Fe, Fe(Mn) carbides, $Fe^{2+}$ oxide phases, and $Fe^{3+}$ oxide phases for supported catalysts after exposure to CDH reaction conditions. It should be noted that the $Fe^{2+}$ phases vary according to support: $(Fe,Mn)Al_2O_4$ for the $\gamma$-$Al_2O_3$ support, $(Fe,Mn)_2SiO_4$ for the silica support, and (Mg,Fe,Mn)O for the magnesia support.

Evidence from both spectroscopic methods indicates that the support plays a major role in determining the actual forms of Fe and Mn present in the catalyst formulation after (and presumably during) the CDH reaction. Clearly, both the MgO and $Al_2O_3$ supports stabilize the $Mn^{2+}$ and $Fe^{2+}$ oxidation states in the form of oxide ((Mg,Fe,Mn)O) and spinel ($(Mn,Fe)Al_2O_4$) phases, respectively. The major difference in phase exhibited by the $Fe_2Mn$/Mg(Al)O catalyst compared to the other catalysts is the presence of a significant ferric iron phase.

The work summarized in the two projects D2 and D3 demonstrates how complex the preparation and pre-reduction of a single metal or mixed metal catalyst such as Fe, Co, or Mn on silica or alumina can be. Furthermore, the influence of the gaseous atmosphere and the role of the support on the reduction have also been demonstrated to be important. Yet, very rarely in the literature does one find detailed characterization of the state of the metals in catalysts as prepared or after pre-reduction. Usually, a preparation and reduction sequence is reported and the assumption is made as to the reduced nature of the catalyst. This characterization work clearly emphasizes the critical need for better characterization in order to understand properly the nature of catalysts in complex reactions such as FTS and CDH.

**E.1: M.S. theses completed:**

1. **Sukanya Ranganathan:** Carbon assisted electrolysis of water to produce hydrogen at room temperature, WVU, 2007.
2. **Shilpa Bollineni:** Hydrogen production via carbon- assisted water electrolysis at room temperature: Effects of catalysts and carbon type, WVU, 2008.
3. **Savan Suri:** Synthesis, structural and magnetic properties of copper-doped cerium oxide nanoparticles, WVU, 2010.

4. **L.P. Akkineni:** Hydrothermal pretreatment of biomass samples for producing energy efficient hydrogen electrochemically, WVU, 2011.
5. **Sai Pyapall :** in progress. WVU, 2012.

**E.2: Ph.D. dissertations completed:**

1. **Jenny Shim:** Size Effects in the Magnetic Properties of NiO nanoparticles, WVU, 2006.
2. **Wenqin Shen**, Novel catalysts for the production of CO- and $CO_2$-free $H_2$ and carbon nanotubes by dehydrogenation of methane. University of Kentucky, 2008.
3. **Vivek Singh:** Size Dependent Magnetic Properties of Nickel Nanoparticles embedded in silica matrix, WVU, 2009.
4. **James Rall:** Nanosize Effects in the Magnetic Properties of Two Layered Hydroxides of Nickel, WVU, 2011.

**E. 3: Ph.D. dissertations in progress:**

5. **Xuepei (Kathy) Shi:** Chemical Engineering, University of Kentucky, 2013.
6. **Abhijit Bhagavatula:** Chemical Engineering, University of Kentucky, 2013.

**A4: Catalyst characterization publications in peer reviewed journals under contract DE-FC26-05NT42456:**

1. S. Bali, G. Bali, F. Huggins, M. S. Seehra, V. Singh, J. Hancock, R. Harrison, G. Huffman, R. Pugmire, R. Ernst, and E. Eyring: Synthetic doped amorphous ferrihydrite for the Fischer-Tropsch synthesis of alternative fuels, Industrial & Eng. Chem. Res. 51,4515- 4522,(2012).

2. M. S. Seehra, S. Suri and V. Singh: Effects of Cu doping on the magnetism of $CeO_2$ nanoparticles, J. Appl. Phys. 111, 07B516/1-3,(2012).

3. D. B. Bacik, M. Zhang, D. Zhao, C. B. Roberts, M. S. Seehra, V. Singh and N. Shah: Green synthesis and characterization of supported polysugar stabilized Pd nanoparticle catalysts for enhanced hydro-dechlorination of trichloroethylene, Nanotechnology, 13, 294004/1-13,(2012).

4. M. S. Seehra, L. P. Akkineni, M. Yalamanchi, V. Singh, and J. Poston: Structural characteristics of nanoparticles produced by hydrothermal pretreatment of cellulose and their applications for electrochemical hydrogen generation, International Journal of Hydrogen Energy, 37, 9514-9523, (2012).

5. J. D. Rall and M. S. Seehra: Nature of magnetism in the quasi-2D layered alpha-$Ni(OH)_2$, J. Phys.: Condens. Matter , 24, 076002/1-8, (2012).

6. M. S. Seehra, J. D. Rall, J. C. Liu and C. B. Roberts: Core-shell model for the magnetic properties of Pd nanoparticles, Materials Letters, 68, 347-349 (2012).

7. V. Singh, M. S. Seehra, F. E. Huggins, N. Shah, and G. P. Huffman: Temperature and size dependence of magnetic and electron magnetic resonance parameters of Fe nanoparticles embedded in amorphous $SiO_2$ matrix, J. Appl. Phys. 109, 07B506/1-3, (2011).

8. V. Singh, M. S. Seehra, S. Bali, E. M. Eyring, N. Shah, F. E. Huggins and G. P. Huffman: Magnetic properties of (Fe, Fe-B)/$\gamma$-$Fe_2O_3$ core-shell nanostructure, J. Phys. Chem. Solids,72, 373-1376, (2011).

9. M. S. Seehra and V. Singh: Use of microwave heating in coal research and in materials synthesis, book chapter in " Microwave Heating " (edited by U. Chandra, Intech Publishers, Croatia, 2011) pages 163-180. ISBN: 978-953-307-573-0.

10. J. D. Rall, M. S. Seehra, and E. S. Choi: Metamagnetism and nanosize effects in the magnetic properties of quasi-2D system beta-$Ni(OH)_2$, Phys. Rev. B 82, 184403/1-9, (2010).

11. S. Bali, F. E. Huggins, G. P. Huffman, R. D. Ernst, R. J. Pugmire, and E. M. Eyring, Iron aerogel and xerogel catalysts for Fischer-Tropsch synthesis of diesel fuel. [doi: 10.1021/ef8005367] Energy & Fuels, 23, 14-18, (2009).

12. F. E. Huggins, D-J. Kim, B. C. Dunn, E. M. Eyring, and G. P. Huffman, An evaluation of least-squares fitting methods in XAFS spectroscopy: Iron-based SBA-15 catalyst formulations. [doi: 10.1016/j.saa.2008.12.026] Spectrochimica Acta A 72, 975-983, (2009).

13. V. Singh and M. S. Seehra: Temperature and size dependence of electron magnetic resonance spectra of Ni nanoparticles embedded in amorphous $SiO_2$ matrix, J. Phys: Condens Matter, 21, 456001/1-9, (2009).

14. M. S. Seehra, V. Singh, X. Song, S. Bali and E. M. Eyring: Synthesis, structure and magnetic properties of non-crystalline ferrihydrite nanoflakes, J. Phys. Chem. Solids, 71, 1362- 1366, (2010).

15. J. D. Rall, M. S. Seehra, N. Shah and G. P. Huffman: Comparison of the nature of magnetism in alpha-$Ni(OH)_2$ and beta-$Ni(OH)_2$, J. Appl. Phys. 107, 09B511/1-3,(2010).

16. P. Dutta, S. Pal and M. S. Seehra, N. Shah and G. P. Huffman: Size dependence of magnetic parameters and surface disorder in magnetite nanoparticles, J. Appl. Phys. 105, 07B501/1-3, (2009).

17. V. Singh, M. S. Seehra, and J. Bonevich: AC susceptibility studies of magnetic relaxation in nanoparticles of Ni dispersed in silica, J. Appl. Phys. 105, 07B518 /1-3, (2009).

18. M. S. Seehra and S. Bollineni: Nanocarbon boosts energy-efficient hydrogen production in carbon-assisted water electrolysis, Int. J. Hydrogen Energy. 34, 6078-6084, (2009).

19. V. Singh, M.S. Seehra and J. Bonevich: Nickel-silica nanocomposite: Variation of the blocking temperature with magnetic field and measuring frequency, J. Appl. Phys. 103, 07D524/1-3, (2008).

20. S. Bali, G. Turpin, R. Ernst, R. Pugmire, V. Singh, M.S. Seehra and E. Eyring: Water-gas shift catalysis using iron aerogels and iron aerogels doped with Pd by the gas phase incorporation method, Energy & Fuels, 22, 1439-1443, (2008).

21. P. Dutta, M.S. Seehra, S. Thota and J. Kumar: A comparative study of the magnetic properties of bulk and nanocrystalline $Co_3O_4$, J. Phys. Condens. Matter 20, 015218/1-8, (2008).

22. P. Dutta, M.S. Seehra, Y. Zhang and I. Wender: Nature of magnetism in copper doped oxides: $ZrO_2$, $SiO_2$, MgO, $SiO_2$, $Al_2O_3$ and ZnO, J. Appl. Phys. 103, 07D104/1-3, (2008).

23. H. Shim, P. Dutta, M.S. Seehra and J. Bonevich: Size dependence of the blocking temperature and electron magnetic resonance spectra in NiO nanoparticles, Solid State Commun. 145, 192-196, (2008).

24. S. Bali, F. E. Huggins, G. P. Huffman, R. D. Ernst, R. J. Pugmire, and E. M. Eyring, Synthesis of Fischer-Tropsch diesel using iron oxide aerogels and xerogels containing potassium and cobalt. ACS Fuel Chem. Div. Preprints (CD-ROM), 53(1), 160-161, (2008).

25. W. Shen, F. E. Huggins, N. Shah, G. Jacobs, Y. Wang, X. Shi, and G. P. Huffman, Novel Fe-Ni nanoparticle catalyst for the production of CO- and $CO_2$-free $H_2$ and carbon nanotubes by dehydrogenation of methane. [doi:10.1016/j.apcata.2008.09.004] Applied Catalysis A: General, 351, 102-110, (2008).

26. F. E. Huggins, W. Shen, N. Cprek, N. Shah, N. S. Marinkovic, and G. P. Huffman, In situ XANES spectroscopic investigation of the pre-reduction of iron-based catalysts for non-oxidative alkane dehydrogenation. Energy & Fuels, 22, 3620-3625, (2008).

27. S. Pal. P. Dutta, N. Shah, G.P. Huffman and M.S. Seehra: Surface spin disorder in $Fe_3O_4$ nanoparticles probed by electron magnetic resonance spectroscopy and magnetometry, IEEE Trans. Magnetics 43, 3091-3093, (2007).

28. P. Dutta, S. Pal. M.S. Seehra, M. Anand and C.B. Roberts: Magnetism in dodecanethiol-capped gold nanoparticles: Role of size and capping agent, Appl. Physics Lett. 90, 213102/1-3, (2007).

29. P. Dutta, F. Shi, Y. Zhang, I. Wender and M.S. Seehra: Characteristics of copper-based catalysts for methanol to $H_2$ conversion, ACS Division of Fuel Chem. 52(2), 467-468 (2007).

30. G.C. Turpin, B.C. Dunn, E. Fillerup, Y. Shi, P. Dutta, V. Singh, M.S. Seehra, E.M. Eyring, R.J. Pugmire and R.D. Ernst: Improved catalytic activity with gas-phase incorporated Pd on ceria for the water-gas shift reaction, Preprint paper, ACS Division of Fuel Chem. 52(2), 411-412, (2007).

31. M.S. Seehra, S. Bollineni, S. Ranganathan and P. Dutta: Effects of catalysts on carbon-assisted water electrolysis to produce $H_2$ at room temperature, Preprint paper, ACS Division of Fuel Chemistry 52(2), 457-458, (2007).

32. W. Shen, Y. Wang, X. Shi, N. Shah, F. Huggins, S. Bollineni, M.S. Seehra and G. Huffman: Catalytic non-oxidative dehydrogenation of ethane over Fe-Ni and Ni catalysts supported on Mg(Al)O to produce pure hydrogen and easily-purified carbon nanotubes, Energy & Fuels 21, 3520-3529, (2007).

33. M.S. Seehra, P. Dutta, V. Singh, Y. Zhang and I. Wender: Evidence for room temperature ferromagnetism in $Cu_xZn_{1-x}O$ from magnetic studies in $Cu_xZn_{1-x}O$/CuO composite, J. Appl. Phys.101, 09H107/1-3, (2007).

34. P. Dutta and M.S. Seehra: Effect of DNA coating on magnetic relaxation in $\gamma$–$Fe_2O_3$ nanoparticles, IEEE Trans. Magnetics 43, 2468-2470, (2007).

35. W. Shen, N. Shah, F. E. Huggins, and G. P. Huffman, Nanoparticle catalysts for the production of CO-free hydrogen and carbon nanotubes by non-oxidative dehydrogenation of methane. ACS Fuel Chem. Div. Preprints (CD-ROM), 52(2), 463-464, (2007).

36. G. P. Huffman, W. Shen, N. Shah, and F. E. Huggins, Catalytic decomposition of hydrocarbons to produce pure hydrogen and carbon nanotubes. Program and Full Papers, 2007 International Conference on Coal Science and Technology (Nottingham, U.K.), Paper 6D2, CD-ROM, 3 pp., (2007).

37. P. Dutta, S. Pal, M.S. Seehra, Y. Shi, E.M. Eyring and R.D. Ernst: Concentration of $Ce^{3+}$ and oxygen vacancies in cerium oxide nanoparticles, Chem. Mater. 18, 5144-5146, (2006).

38. G.C. Turpin, B.C. Dunn, E. Fillerup, Y. Shi, P. Dutta, V. Singh, M.S. Seehra, R.J. Pugmire, E.M. Eyring and R.D. Ernest: Gas-phase incorporation of Pd into ceria doped silica aerogel for water-gas-shift catalysis, Proceedings 23rd Annual International Coal Conference 2006, 13 pages.

39. P. Dutta, B.C. Dunn, E.M. Eyring, N. Shah, G.P. Huffman, A. Manivannan and M.S. Seehra: Characteristics of cobalt nanoneedles in 10% Co/aerogel Fischer-Tropsch catalyst, Chem. Materials,17, 5183-5186, (2006).

40. H. Shim, A. Manivannan, M.S. Seehra, K.M. Reddy and A. Punnoose: Effect of interparticle interaction on the magnetic relaxation of NiO nanorods, J. Appl. Phys. 99, 08Q503/1-3, (2006).

41. P. Dutta, A. Manivannan, M.S. Seehra, N. Shah and G.P. Huffman: Magnetic and structural properties of DNA-maghemite nanocomposite, J. Appl. Phys. 99, 08H105/1-3, (2006).

42. A. Manivannan, P. Dutta, G. Glaspell and M.S. Seehra: Nature of magnetism in Co and Mn substituted ZnO prepared by sol-gel technique, J. Appl. Phys. 99, 08M110/1-3, (2006).

43. P. Dutta, S. Pal, M.S. Seehra, Y. Shi, E.M. Eyring and R.D. Ernst: Concentration of $Ce^{3+}$ and oxygen vacancies in cerium oxide nanoparticles, Chem. Mater. 18, 5144-5146, (2006).

44. Y. Wang, N. Shah, W. Shen, F. Huggins, and G. P. Huffman, Production of hydrogen and carbon nanotubes by catalytic non-oxidative dehydrogenation of hydrocarbon gases. ACS Fuel Chem. Div. Preprints (CD-ROM), 51(2), 465, (2006).

45. D. J. Kim, B. C. Dunn, F. Huggins, G. P. Huffman, M. Kang, J. E. Yie, and E. M. Eyring, SBA-15 supported iron catalysts for Fischer-Tropsch production of diesel fuel. Energy & Fuels, 20, 2608-2611, (2006).

46. Y. Wang, N. Shah, F. E. Huggins, and G. P. Huffman, Hydrogen production by catalytic dehydrogenation of tetralin and decalin over stacked cone carbon nanotube-supported Pt catalysts. Energy & Fuels, 20, 2612-2615, (2006).

# "Co-gasification of Coal-Biomass",

Kaushlendra Singh; Jingxin Wang, and John Zondlo, West Virginia University

**The Project Goals:**

Develop a co-gasification system and process using coal-woody biomass feedstock for producing syngas with improved $H_2$/CO ratios for liquid fuel synthesis.

**Tasks:**

1. Develop a co-gasification process and customized co-gasification equipment for coal and woody biomass using experimental and modeling techniques. We will investigate the effect of down-draft gasifier operating conditions (Coal to biomass ratio, gas flow rate and gasifier temperature) on the composition of gas produced, syngas carbon conversion efficiency, and syngas energy conversion efficiency.
2. Characterize feedstock pretreatments and operating conditions. We will determine selected physical and thermo-chemical properties of biomass (wood residues), coal, and mixtures of coal and biomass.

**Status Report:**

Both objectives of the project have been achieved and a graduate student has finished his master's thesis which will be submitted to the graduate school, West Virginia University by August 2, 2012. In the duration of the project, the student had published **one** journal article, **three** conference proceeding papers, **one** master's thesis, and made **five** technical presentations. In addition, **two** journal articles are in preparation.

**Experiments Performed:**

Gasification tests were performed using coal (Bituminous) and hardwood pellets mixtures. Three mixtures hardwood pellets, 80WP20C (80% hardwood pellets and 20% coal), 50WP50C (50% hardwood pellets and 50% coal), 20WP80C (20% hardwood pellets and 80% coal) and coal were prepared. Hamilton air tight syringes were used to collect samples from gasifier and insert them into a gas chromatograph (GC) system (Clarus GC 580, Perkin Elmer, Waltham, MA), which was used for determining percentage composition of gas.

**Flow Rate Measurements**

Measurements on the flow rate of the gas produced in the gasfier were required to calculate the carbon efficiency and energy efficiency of the system. It was measured by installing an orifice flow meter supplied by All Power Labs (APL Berkeley, CA) in the gas outlet line. Two pressure sensors were installed across the orifice plate to measure pressure difference. Equation 1 was used for calculating the flow rate of gas produced by the gasifier.

$$Q = C_f * A_o\sqrt{2\Delta P/\rho} \quad (1)$$

Where Q is the volumetric flow; $C_f$ is friction coefficient, dependent on meter design; $A_o$ is the orifice area; $\Delta P$ is the measured pressure difference across the orifice; and $\rho$ is fluid density. Values of $C_f * A_o = 0.421233334$ in$^2$ and the density of syngas = 0.95 Kg/m$^3$ were used in the calculations.

**Syngas Carbon Conversion Efficiency and Syngas Energy Efficiency**

The syngas carbon efficiency is the ratio of the total carbon present in the syngas to that of the feedstock. The total carbon present in the syngas was calculated by measuring the amounts of carbon-dioxide, carbon-monoxide and methane in the syngas. By using the mole concept and with the known gas flow rate, the carbon content in the syngas was calculated by means of Equation 2. The amount of carbon in the feedstock was calculated from ultimate analysis data (Model: Clarus 2400 CHNS analyzer, Perkin Elmer, Waltham, MA).

$$C_{eff} = \frac{(CO_2 + CO + CH_4) * 12/22.4 * F_{gas} * 1000}{F_{feed} * (1 - X_m/100) * (1 - X_{ash}/100) * C/100} \quad (2)$$

Where $CO_2$, CO and $CH_4$ are the percentage composition of these components of the Syngas (%v/v), $F_{gas}$ is the flow rate of syngas (l/min), $F_{feed}$ is the flow rate of the feedstock (kg/min), $X_m$ (%wb) and $X_{ash}$ are the moisture and ash weight percentages of feedstock respectively, and C (%daf) is the carbon percentage in the feedstock.

The syngas energy efficiency is the ratio of the energy contained the syngas to the total energy supplied through the feedstock (Kumar et al., 2009). The syngas energy efficiency was calculated by using Equation 3. The energy contained in the syngas was estimated by using the gas composition data and the standard heating values of carbon-monoxide, methane and hydrogen. The energy of the feedstock was calculated by using gross heating values measured by a bomb calorimeter (Model: Parr 6300 Calorimeter, Parr Instrument Company, Moline, IL., USA). Feedrate was determined by calculating the total amount of feed used from the starting of flare till the shutting down of the system. Moisture content was determined by the oven drying method. Ash content was measured by weighting the residue after heating the feedstock at 700$^o$C in the presence of oxygen for 15 minutes.

$$E_{eff} = \frac{(35.81 * CH_4 + 12.62 * CO + 10.71 * H_2) * F_{gas}}{F_{feed} * (1 - X_m/100) * E} \quad (3)$$

Where $H_2$, CO and $CH_4$ are the percentage composition of these components of the Syngas (%v/v), $F_{gas}$ is the flow rate of syngas (l/min), $F_{feed}$ is the flow rate of the feedstock (kg/min), $X_m$ (%wb) is the moisture content of feedstock respectively, E is the gross heating value (KJ/kg).

**Results:**

**Temperature Profile:** - Fig. 1 shows the temperature profile in pyrolysis zone, combustion zone, top and bottom of the reduction zone and gas exit zone with time obtained from the gasification of Hardwood pellets. In the combustion zone, temperature increased to 1100$^o$C immediately after the ignition and it remained almost constant after that. The temperature of the reduction zone was much lower than that of the combustion zone. In the reduction zone, the temperature raised gradually till 30 minutes. A sudden rise of the temperature from 250$^o$C to 400$^o$C was observed at 30 minutes. This raise indicates heating up of the gasifier. The temperature in the top of reduction zone (450$^o$C) was higher than that of the bottom of the reduction zone (350$^o$C). In the pyrolysis zone, the temperature range of 400-500$^o$C was measured. The temperature of the gas exit zone remained less than 200$^o$C. This is because of the reason that gas cooled down when it moved from the bottom to the top of the reactor.

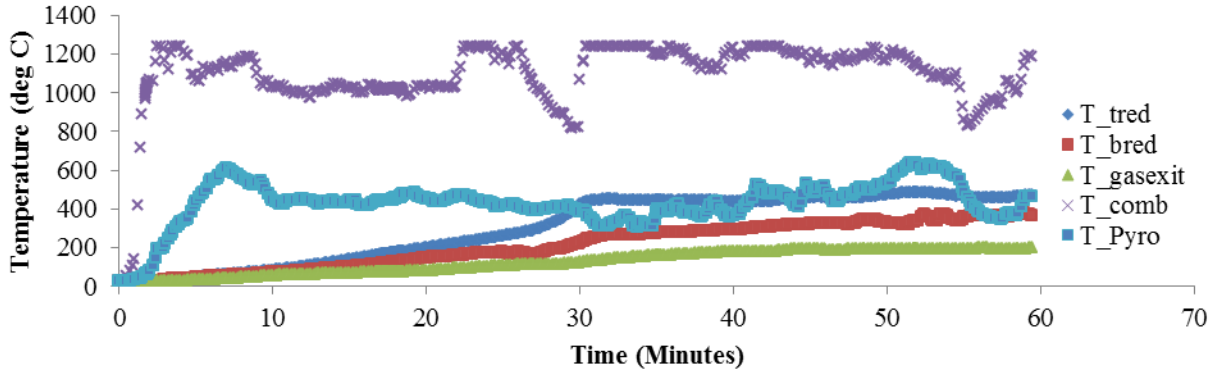


**Figure 1 Temperature ($^o$C) rise in top and bottom zones of gasifier after with respect to running time of gasifier**

**Gas flow rate**: - The gas production was started after 30 minutes from the ignition. To calculate gas flow rate, data range of 30 to 60 minutes was used. An average gas flow rate of 134.52 L/min was recorded during the gasification run of hardwood pellets. A reduction of gas flow rate was observed after 50 minutes of run. The reason could be clogging, due to fine particles, of grate beneath the reduction zone. The pressure drop inside the reactor was increased to overcome the effect of clogging.

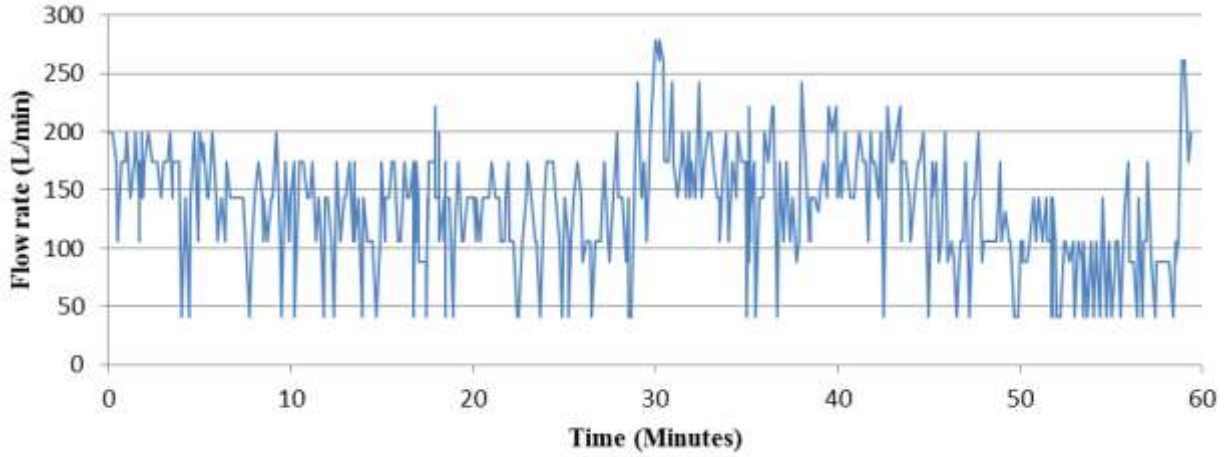


**Figure 2 Gas flow rate obtained by gasification of Hardwood Pellets with air as a gasification agent.**

**Gas Composition:** - Table 1 represents percentage composition of gas obtained by gasifying of wood pellets and coal-pellet mixtures with air as the gasification agent. Nitrogen percentage of the syngas produced was high due to high percentage of nitrogen in air. Hydrogen composition of 16.05% was obtained in the biomass gasification and it decreased significantly when 50% of coal was mixed with the biomass. It was found that high temperature favored hydrogen production in the co-gasification process due to the endothermic nature of most of the gasification reactions. Addition of coal into the feedstock decreased the maximum temperature of the system from around 1200$^{o}$C to around 850$^{o}$C (Figure 3). Moreover, low hydrogen content of coal might also be the reason for a reduction in the hydrogen content.

**Table 1 Syngas composition obtained by gasification of WP (Hard wood pellets); 80WP20C = (80% hardwood pellets and 20% coal), etc. No difference at CI**

| Sample | $N_2$ | CO | $H_2$ | $CO_2$ | $CH_4$ | $O_2$ |
|---|---|---|---|---|---|---|
| WP | 47.73 ± 3.82 | 20.95 ± 2.42 | 16.05 ± 2.95$^{a}$ | 11.27 ± 2.78$^{b}$ | 1.85 ± 0.45$^{a}$ | 2.14 ± 1.51 |
| 80WP20C | 54.93 ± 3.74 | 16.74 ± 2.45 | 12.78 ± 1.77$^{a,b}$ | 13.6 ± 1.00$^{a,b}$ | 1.21 ± 0.5$^{a}$ | 0.97 ± 0.41 |
| 50WP50C | 59.59 ± 3.05 | 13.22 ± 1.02 | 10.36 ± 1.52$^{b}$ | 14.89 ± 1.65$^{a,b}$ | 0.92 ± 0.99$^{a}$ | 1.03 ± 0.05 |
| 20WP80C | 64.17 ± 1.84 | 6.57 ± 0.63 | 9.99 ± 1.43$^{b}$ | 16.7 ± 1.48$^{a}$ | 1.43 ± 0.64$^{a}$ | 1.16 ± 0.2 |
| Coal | 74.78 ± 2.34 | 3.00 ± 1.68 | 3.09 ± 2.04 | 16.5 ± 1.06$^{a}$ | 0.44 ± 0.22$^{a}$ | 2.19 ± 0.5 |

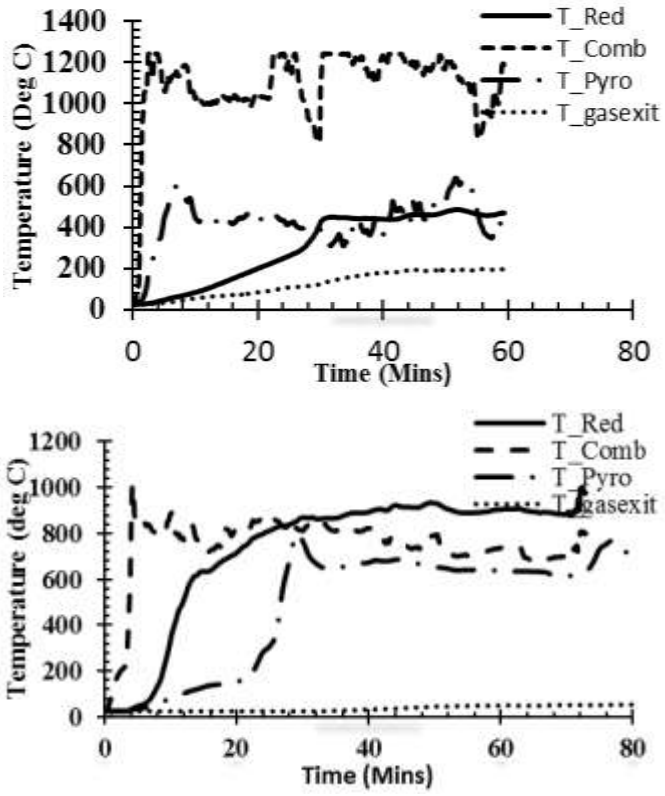


(a) (b)

**Figure 3 Temperature profiles obtained during the gasification of (a) hardwood pellets and (b) mixture of 50WP50C (50% hardwood pellets and 50% Coal) in a fixed bed down-draft gasifier.**

Additionally, carbon-monoxide composition of 20.95 (%v/v) was obtained by gasification of the wood pellets. It decreased significantly upon addition of coal into the feedstock. A mixture of 80% wood pellets and 20% coal produced syngas with 16.74% of carbon-monoxide. Also, a hard plate like layer of agglomerated coal was observed above the combustion zone after the gasification of mixtures with more than 50% coal. The maximum temperature of the gasification system reached up to 1000$^{o}$C for the gasification of the feedstock having 80% of coal and 20% of hardwood pellets. Despite of this temperature, carbon-monoxide content reduced in the syngas. The formation of agglomerates probably caused blockage of gas flow and restricted carbon combustion. We predict coal agglomeration to be the reason for significant decrease of carbon-monoxide in the syngas. As result, a higher amount of carbon-dioxide but less carbon-monoxide was produced when coal was added. This indicates that the reduction reactions, which produce CO and $H_2$, did not take place effectively.

**Syngas Carbon Efficiency and Syngas Energy Efficiency**

Syngas carbon and syngas energy efficiency values with different mixtures are presented in Table 2 Syngas carbon efficiency of 50.73% was observed in the gasification of wood pellets. An increase in syngas carbon conversion efficiency was observed when up to 50% coal was mixed with the hardwood pellets. Carbon efficiency increased because coal has higher carbon content than hardwood pellets and more carbon was available for conversion. The carbon conversion of the feedstock with 80% coal reduced to 58.48% from 70.02% calculated for feedstock with 50% coal. The agglomeration of coal could be the reason of the reduction in the carbon conversion. However, the increase in the carbon efficiency was due to increase in the carbon-dioxide content of the syngas. Hence, an increase in the overall energy output from the syngas was not expected. Energy efficiency was not disturbed by the inclusion of coal in the feedstock. It remained the same for wood pellets, 80WP20C and 50WP50C but it reduced significantly for 20WP80C.

**Table 2 Syngas carbon efficiency and energy efficiency obtained by gasification of WP (hardwood pellets) and mixtures of hardwood pellets and coal in air.**

| Sample | Syngas Carbon Efficiency | Syngas Energy Efficiency |
|---|---|---|
| Wood Pellets | 50.73 ± 1.80 | 38.94 ± 0.11[a] |
| 80WP20C | 62.48 ± 3.97[a] | 37.82 ± 3.55[a] |
| 50WP50C | 70.02 ± 3.95[a] | 35.02 ± 1.20[a,b] |
| 20WP80C | 58.48 ± 0.2[a] | 26.63 ± 2.77[b] |

[a, b] No significant difference at 95%CI

**Problems with Coal Gasification in the Fixed Bed Down-Draft Gasifier:**

Coal, with particle size in the range of 1”-2”, was fed into the fixed bed down-draft gasifier and syngas with only 3% of carbon-monoxide and 3.09% of hydrogen was produced even though the temperatures of the combustion zone and reduction zone were around 1100$^{o}$C. A flare was not detected when only coal was used as the feedstock due to low quantity of combustible gases in the syngas. The main reason was the un-burnt coal particles and blockage of the reactor caused by the agglomeration of the coal (Figure 4) which physically caused combustion in the reduction zone and hence the temperature of the physical reduction zone increased. The carbon-dioxide content of syngas increased because of the combustion of the coal. This problem may be reduced by using smaller particle size of coal and by increasing the cross-sectional area of the combustion zone and using a non-agglomerating coals (sub-bituminous and lignite)

(a) (b)

**Figure 4 (a) A layer formed by the coal agglomeration during the gasification of coal rich feedstock and (b) pieces of coal agglomeration obtained from the reactor.**

**JOURNAL ARTICLES**

Brar, J. S., K.Singh, J. Wang and S. Kumar. Co-gasification of Coal and Biomass – A review. *International journal of Forestry Research.* Hindawi Publishing Corporation Paper no. 363058, doi:10.1155/2012/36305

**THESIS**

Brar, J. 2012. Co-gasification of coal and biomass. M.S. Thesis, West Virginia University.

**PROCEEDINGS**

Brar, J. S., K. Singh, J. W. Zondlo. Technical challenges and opportunities in co-gasification of coal and biomass. 2012 Central Hardwood Conference Proceedings, In Review

Brar, J. S., K. Singh, J. Zondlo, J. Wang, and S. Kumar. 2011. Co-gasification of Appalachian hardwood residues and coal: Feedstock properties. ASABE Paper No. 1110685. St. Joseph, Mich.: ASABE

Brar, J. S., K. Singh, J. Zondlo, J. Wang, and S. Kumar. 2011. Co-gasification of Appalachian hardwood residues and coal: Feedstock properties. ASABE American Society of Agricultural and Biological Engineers' Annual International Meeting, Louisville, Kentucky, August 7-11, 2011.

Brar, J. S., K. Singh, J. Zondlo, W. Jin, and S. Kumar. 2012. Co-gasification of coal and Applachian harwood: American Society of Agricultural and Biological Engineers' 2012 Annual International Meeting, Dallas, TX, July 28-August 1, 2012.

Brar, J. S., K. Singh, J. Zondlo, J. Wang, and S. Kumar. 2012. Co-gasification of coal and biomass for electricity production. Presentation for Linking Innovation Industry and Commecialization Event, April 11, Morgantown, WV

# Scalable Production of Middle Distillate Range Transportation Fuels from Coal + Biomass using a Gas-to-Liquids Approach

Dr. Christopher B. Roberts and Dr. Mario R. Eden
Department of Chemical Engineering
Auburn University

**Abstract:**
There are a number of challenges facing Fischer Tropsch Synthesis (FTS) technologies for scalable applications including i) optimization of overall FTS product yields towards desired fuel fractions, ii) improvement of catalyst activity maintenance and overall reliability, iii) integrated product upgrading reactions to narrow the resultant product distribution toward middle distillate fuel fractions, and iv) significant improvements of heat and mass transfer to allow simple fixed bed operation. We have addressed these issues by engineering a tunable and scalable FTS unit that optimizes economy of operation and process intensification (smaller units) as well as integration of energy within the process. We have shown that modifications to the FTS process under dense phase conditions (including supercritical fluid recycle, supercritical fluid phase FTS or SCF-FTS) and optimization of the operating conditions results in significant enhancement of middle distillate products while also significantly reducing the production of undesirable methane, and significant extending catalyst lifetime due to in situ extraction. These modifications have included a novel utilization of undesired light products to improve heat and mass transfer within the media. Moreover, due to the process intensification in this configuration as a result of these changes, middle distillate targeted SCF-FTS were performed in a simple, small fixed bed reactor system. Additional work involved the integration of product upgrading stages, namely oligomerization and cracking/isomerization reactions, subsequent to the SCF-FTS catalyst bed to further narrow the FTS products to the fuel range in single pass operation. Specifically, we have successfully operated the continuous SCF-FTS reactor in a triple catalyst bed configuration with Fe and/or Co based FTS catalysts in stage 1, and supported Pd catalysts and zeolite catalysts in stages 2 and 3. This allowed for determination of process performance as indicated by reaction parameters including conversion, selectivity, product yields, and carbon number distribution as related to key reaction conditions including catalyst type, temperature and pressure.

**Introduction:**
FT product upgrading via catalytic oligomerization and hydrocracking/isomerization can convert light olefins into middle distillate ($C_8$ - $C_{22}$) range hydrocarbons, while also altering the long-chain hydrocarbons into fuel range products. Utilization of supercritical fluid (SC) media in FTS (SC-FT) has been demonstrated to reduce the selectivity towards $CH_4$ and $CO_2$ as a result of the enhanced heat transfer that the supercritical fluid offers compared to traditional gas phase Fischer-Tropsch synthesis (GP-FT). In addition, the improved product solubilities in the SC medium results in prolonged catalyst life and activity maintenance. In this study, a vertically aligned fixed bed reactor system with a cascade of three catalyst beds that are arranged sequentially has been designed and has been used to incorporate Fischer-Tropsch synthesis in the first bed, oligomerization (O) in the second bed and hydrocracking/isomerization (H) in the third bed (FTOC). Compared to GP-FT alone, gas phase FT with the subsequent upgrading beds (GP-FTOC) is demonstrated to result in a reduction in the olefin selectivity and $C_{26+}$ selectivity.

Moreover, GP-FTOC results in a marked enhancement in the production of branched paraffins as well as aromatics. Utilization of supercritical hexane as the reaction medium in SC-FT and supercritical phase FTOC (SC-FTOC) resulted in a significant reduction in both $CH_4$ selectivity and $CO_2$ selectivity, along with a well maintained catalyst activity compared to the gas phase operation. Interestingly, significant amounts of aldehydes and cyclo-parafins, were collected in SC-FT and in SC-FTOC, respectively, while not being observed in traditional gas phase operation (both GP-FT and GP-FTOC).

To improve the selectivity of the process to middle distillates requires additional upgrading reactions. To carry this out, a three bed reactor system (consisting of three sequential fixed bed reactors) has been designed and constructed in this work in order to promote the direct production of middle distillate range hydrocarbons from syngas in a single pass arrangement. FT is performed in the first catalyst bed, generating a variety of hydrocarbon lengths and types. The second bed is used for oligomerization to convert light olefins into gasoline and diesel range products (to promote branching and to enhance octane rating and cold-flow properties or aromatization to enhance density). The third bed is used for cracking and isomerization reactions to convert the heavy product into the middle distillate range and to increase branching. To achieve the optimum performance within each catalyst bed, this three bed reactor was arranged consecutively so that the operation parameters of each reactor can be adjusted and maintained individually. A precipitated iron-based FTS catalyst was used in the first FTS bed. Iron-based FTS catalysts offer lower hydrogenation activity than cobalt-based FTS catalysts, which therefore results in higher olefin selectivity in low temperature FT synthesis. Therefore, using a low-cost precipitated iron-based low temperature FTS catalyst can offer a more desirable feed (due to higher olefin content) when an oligomerization step is implemented sequentially downstream of the FTS step. Light olefins can therefore be oligomerized into the gasoline ($C_5$-$C_{12}$) and diesel ($C_{12}$-$C_{22}$) range fractions so as to increase the middle distillates selectivity in a single pass. Solid phosphoric acid (SPA) and ZSM-5 are used commercially in FTS refineries to convert raw FTS products via oligomerization and isomerization into different target product fractions including gasoline and diesel. Amorphous silica alumina (ASA) has been less studied and has been proposed to offer promising oligomerization performance. Researchers have shown that ASA offers higher distillate density and viscosity in the production of middle distillates by oligomerization compared to SPA and ZSM-5. In addition, it has been reported that oxygenates (in the range of 1-4 mass %) had little effect on the productivity of the ASA catalyst or the quality of the oligomerization product. Given the prospects that ASA offers as a potential oligomerization catalyst, we have decided to utilize ASA to initiate these oligomerization investigations in the second bed of this sequential reactor system.

The third bed of this sequential reactor system is intended to convert long chain FTS hydrocarbons into middle distillate range products through catalytic hydrocracking and isomerization. Common hydrocracking catalysts include Pd and Pt based solid acid catalysts. Pd exhibits a weaker hydrogenation-dehydrogenation activity compared to Pt, thus it can offer a higher cracking activity than Pt. Additionally, it has been reported that Pd based catalysts showed better catalytic performance maintenance than Pt based catalysts. As such, Pd has been chosen over Pt as the active metal in initiating these investigations. ASA has been selected as the support material in the following hydrocracking/isomerization investigations due to its high hydroisomerization performance.

In this study, supercritical fluid as reaction media is also utilized to allow for better heat management, improved product solubility in the bulk reaction media and enhanced catalyst maintenance. Hexanes were chosen as the supercritical solvent.

**Material and Methods**

In this three bed reactor system, the first reaction bed has been used for FTS thereby generating a variety of hydrocarbon lengths and types. The second reaction bed has been used for catalytic oligomerization to convert the light olefins from the FTS bed into gasoline and diesel range products (with potential branching). The third reaction bed has been used for cracking and isomerization reactions to convert the heavy product into the middle distillate range and to increase branching. A traditional precipitated Fe-based catalyst has been selected as the FTS catalyst in the first-bed of this reactor due to its low cost (compared to cobalt-based FTS catalyst) and its ability to yield olefinic products which can be used as feed for the following oligomerization step. In the second reactor, ASA catalysts have been examined for the oligomerization reaction due to the above-mentioned reasons. Pd-loaded ASA (1.0 wt.% prepared by wetness impregnation method) has been selected as the catalyst in the third reactor bed in order to investigate the subsequent hydrocracking/isomerization step. The hydrocracking and isomerization bed with Pd/ASA catalyst is intentionally placed last in this sequence of reaction steps. The Pd/ASA is also a functional hydrogenation and hydroconversion catalyst, and as such, this catalyst can convert olefins into their hydrogen-saturated state (i.e. paraffin). Therefore, if this hydrocracking and isomerization step was placed before the oligomerization bed, no potential oligomerization would occur because of the feed having been already hydrogenated. The reactor system has also been designed to allow the beds to operate at different temperatures so as to optimize each reaction stage, although, isobaric operation is required. A diagram of the three bed reactor system for Fischer-Tropsch synthesis with product upgrading under the supercritical phase conditions is shown in Figure 1.

Helium gas (Airgas, ultra high purity) was used during the system pressure test, reaction startup and shut down. Synthesis gas (Syngas) (Airgas, vol%: $N_2$: CO: $H_2$ = 1.5: 37: 61.5) was fed into the reaction system by a mass flow controller. Hexanes (Fischer, HPLC grade, CAS# 110-54-3) were used as the supercritical fluid reaction media in this investigation, and were delivered into the reaction system using an HPLC pump at a flow rate of 1ml/min in the case of supercritical phase operation. The syngas and hexanes were mixed in a static mixer and the mixture was initially heated in the pre-heating zone. The reactant (and the supercritical fluid medium in the case of supercritical phase operation) entered the top of the tubular fixed-bed reactor and then was passed through each reaction bed sequentially. The reactor effluent was passed through heated tubing to the back pressure regulator (BPR, Straval Valves Inc. model BPH0502T) which was employed to control the system pressure. The effluent was then passed through heated tubing to a cold trap (CT, Swagelok Inc. 304L-HDF4-1000). The cold trap was cooled by an ice-water-mixture. The condensable products were accumulated in the CT and were manually collected and tested periodically by injecting them into a gas chromatograph with a flame ionization detector (GC-FID, Varian GC 3300 with a DB-5 capillary column) and a GC-MS (Waters. Inc.). The incondensable gas mixture (syngas residue and light products) left the CT and was passed through a 10-port injection valve for periodic injection into a gas chromatograph

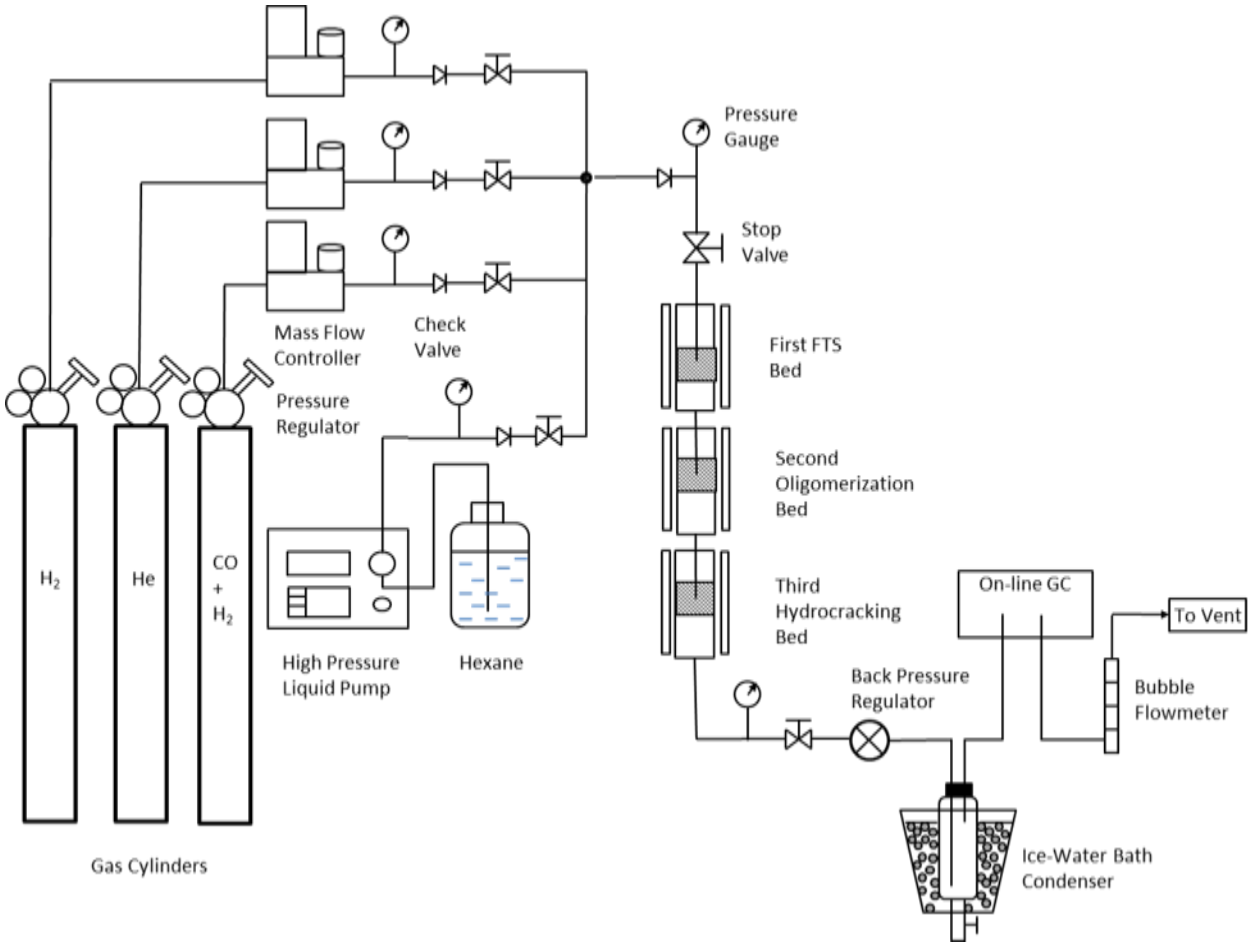


Figure 1 Schematic diagram of the three-bed catalytic reactor system for Fischer-Tropsch synthesis with subsequent oligomerization and hydrocracking/isomerization stages.

Helium gas (Airgas, ultra high purity) was used during the system pressure test, reaction startup and shut down. Synthesis gas (Syngas) (Airgas, vol%: $N_2$: CO: $H_2$ = 1.5: 37: 61.5) was fed into the reaction system by a mass flow controller. Hexanes (Fischer, HPLC grade, CAS# 110-54-3) were used as the supercritical fluid reaction media in this investigation, and were delivered into the reaction system using an HPLC pump at a flow rate of 1ml/min in the case of supercritical phase operation. The syngas and hexanes were mixed in a static mixer and the mixture was initially heated in the pre-heating zone. The reactant (and the supercritical fluid medium in the case of supercritical phase operation) entered the top of the tubular fixed-bed reactor and then was passed through each reaction bed sequentially. The reactor effluent was passed through heated tubing to the back pressure regulator (BPR, Straval Valves Inc. model BPH0502T) which was employed to control the system pressure. The effluent was then passed through heated tubing to a cold trap (CT, Swagelok Inc. 304L-HDF4-1000). The cold trap was cooled by an ice-water-mixture. The condensable products were accumulated in the CT and were manually collected and tested periodically by injecting them into a gas chromatograph with a flame ionization detector (GC-FID, Varian GC 3300 with a DB-5 capillary column) and a GC-MS (Waters. Inc.). The incondensable gas mixture (syngas residue and light products) left the CT and was passed through a 10-port injection valve for periodic injection into a gas chromatograph

with a thermal conductivity detector (GC-TCD, SRI MultiGas Analyzer #1). The gases were then passed through a bubble meter, which allowed for the measurement of the real-time gas effluent volumetric flow rates. The gas effluent was then vented into the fume hood.

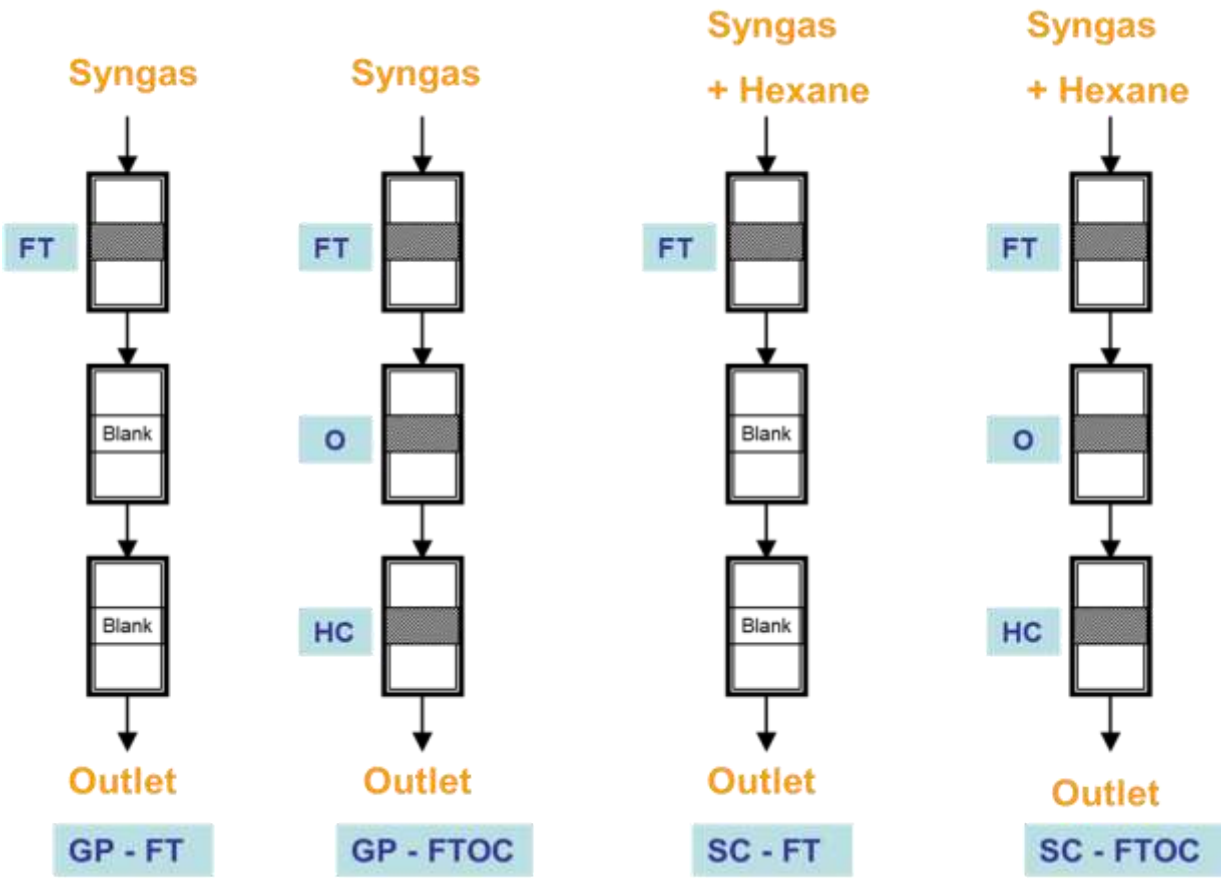


Figure 2 Catalyst loading and reactant/solvent feed schemes for gas phase **and supercritical phase Fischer-Tropsch synthesis with and without subsequent oligomerization** and hydrocracking/isomerization stages.

Figure 2 shows the catalyst loading for each bed during each different operation. The experiments were performed in four modes of operation: gas phase Fischer-Tropsch synthesis (GP-FT), supercritical phase Fischer-Tropsch synthesis (SC-FT), gas phase Fischer-Tropsch synthesis with product upgrading (GP-FTOC) and supercritical phase Fischer-Tropsch synthesis with product upgrading (SC-FTOC). 1 g of precipitated Fe/Zn/K/Cu (molar ratio, Fe : Zn : Cu : K = 1: 0.1 : 0.01 : 0.02) FTS catalyst in the first FTS bed, 1 g of ASA (Sigma-Aldrich, 343358-1KG) catalyst in the second bed, and 1 g of Pd/ASA (1.0 wt.%) hydrocracking/isomerization catalyst in the third bed were used for the corresponding experiments. Before the reactions were performed, a catalyst reduction step was performed using a $H_2$ flow of 50 SCCM at the desired reduction temperature for each reaction bed. The reduction temperature was ramped from room temperature to 270 ºC (the first FTS bed), 400 ºC (the second oligomerization bed), and 400 ºC (the third hydrocracking/isomerization bed) at a rate of 5 ºC/min, respectively. The bed

temperature was held at the desired temperature value for 10 hours. After the reduction, all the catalyst beds were cooled to room temperature. Hydrogen flow was then switched to helium flow at a rate of 100 SCCM in order to build up the system pressure by adjusting the BPR. The reaction temperature for each bed was: FTS at 240 ºC, oligomerization at 200ºC and hydrocracking/isomerization at 330ºC and syngas flow rate for all cases was 50 SCCM with a $H_2$: CO ratio of 1.75:1 (vol). The system pressure was uniform for all three reaction beds during each operation. The system pressure for GP-FT was 17.2 bar, for GP-FTS was 35 bar (the pressure preferred by the upgrading reactions) and 76 bar for all supercritical phase operations (with a hexanes flow rate of 1ml/min while maintaining the partial pressure of syngas at 17.2 bar by ensuring a constant flow rate of syngas). Table 1 shows the catalyst loading and reaction conditions for each operation. The carbon chain propagation probability (α) of the products was defined by the Anderson-Schulz-Flory (ASF) plot, in which the carbon number extended from $C_5$ to $C_{32}$.

**Table 1 Reaction conditions and catalysts employed in the Fischer-Tropsch synthesis with and without subsequent oligomerization and hydrocracking/isomerization stages under gas phase and supercritical phase conditions.**

| Reaction Conditions | | T (°C) (FT/O/C) | P (Bar) | Synthesis Gas Flow Rate (SCCM) [a] | Catalysts loading (FT/O/C) |
|---|---|---|---|---|---|
| Operation Phase | Reaction Stages | | | | |
| Gas Phase | FT[b] | 240/240/240 | 17.2 | 50 | 1g Fe[d] / - / - |
| Gas Phase | FTOC[c] | 240/200/330 | 35.0 | 50 | 1g Fe[d] / 1g ASA / 1g Pd-ASA |
| Supercritical Phase[e] | FT[b] | 240/240/240 | 76 | 50 | 1g Fe[d] / - / - |
| Supercritical Phase[e] | FTOC[c] | 240/200/330 | 76 | 50 | 1g Fe[d]/ 1g ASA / 1g Pd-ASA |

a: Syngas $H_2$: CO: $N_2$ ratio = 62.0: 36.5: 1.5, SCCM stands for standard cubic centimeter per minute
b: FT stands for Fischer-Tropsch synthesis
c: FTOC stands for Fischer-Tropsch synthesis with subsequent oligomerization and hydrocracking/isomerization
d: Fe -based FT catalyst, with a molar ratio of Fe: Zn: K: Cu = 1: 0.1: 0.02: 0.01
e: Supercritical media is Hexane with a media to syngas ratio of 3.5: 1, supercritical media flow rate is 1ml/min

## Results and Discussion

As shown in Figure 3, under supercritical phase conditions, the carbon monoxide (CO) conversion dropped slowly as a function of time on stream (over a 100+ hour period). The CO conversion under these SC conditions was distinguishably higher (ca. 75%) than that obtained in the gas phase studies (ca. 35%) while the syngas flow rate (50 SCCM) and the syngas composition ($H_2$: CO = 1.75:1) were held at consistent values in each of the GP-FT, SC-FT, GP-FTOC and SC-FTOC cases. The syngas partial pressure in the GP-FT, SC-FT and the SC-FTOC experiments were held constant at 17.2 bar, while the syngas partial pressure in the GP-FTOC was maintained at 35 bar. There are several possible reasons for the high CO conversion during

the supercritical phase experiments compared to the gas phase experiments. One potential reason is that the supercritical phase affords the ability to perform in-situ product extraction from the FT catalyst's surface, thereby improving the availability of catalytic active sites thus enhancing the reaction rate (which is proportional to the availability of catalytic active sites). As such, more CO (as well as hydrogen) would react on the catalyst's surface, thereby enhancing the CO conversion with all other conditions being held constant. Another possibility is that during the startup period of the FTS reaction, a tremendous amount of reaction heat is released once the FTS reaction conditions (temperature and pressure) are achieved since the FTS reactions are so highly exothermic. In gas phase operation, the local heat removal rate may not be sufficient such that catalytic hot spots can be generated which would inherently lead to catalyst sintering and fouling (deposition of inactive carbonaceous compounds such as amorphous carbon, graphitic carbon, coke) and thus loss of surface area and active catalyst sites. As a result, catalyst deactivation may have occurred due to a loss of catalyst active sites before steady state operation was achieved in GP-FT and GP-FTOC. However, in the supercritical phase operation, a large amount of reaction heat can be efficiently removed due to the presence of the bulk supercritical reaction media which basically serves as a thermal sink. As a result, the catalyst would not deactivate in the very initial period of the reaction as drastically under SC-FT conditions and SC-FTOC conditions as in the GP-FT and GP-FTOC.

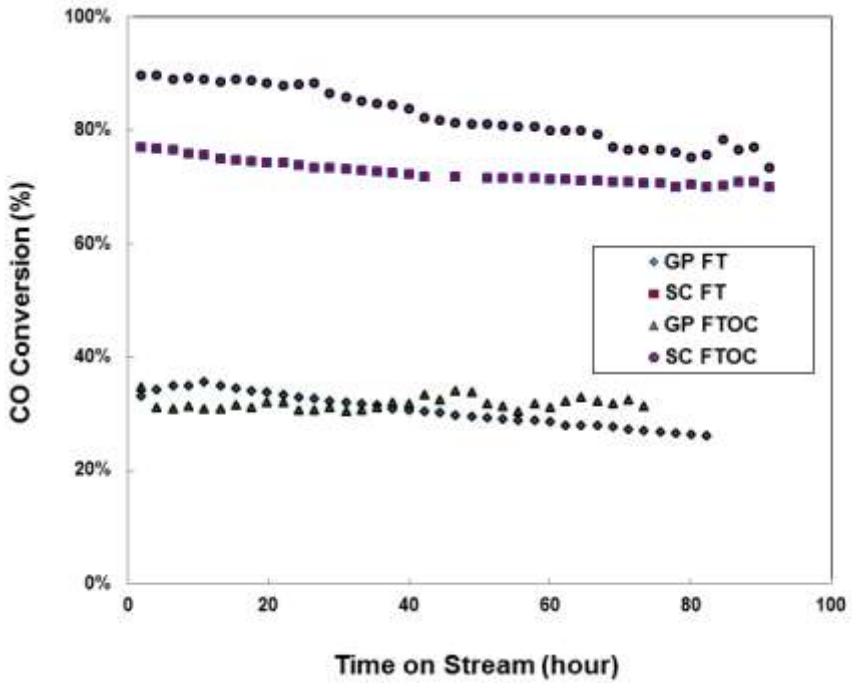


Figure 3. CO conversion as a function of time on stream for gas phase Fischer-Tropsch synthesis (GP-FT), GP-FT with oligomerization and hydrocracking/isomerization (GP-FTOC), supercritical phase Fischer-Tropsch synthesis (SC-FT) and supercritical phase Fischer-Tropsch synthesis with oligomerization and hydrocracking/isomerization (SC-FTOC).

The carbon dioxide ($CO_2$) selectivity obtained during SC-FT (ca. 17%) and SC-FTOC (ca. 13%) operation was lower than in the GP-FT (ca. 23%) and GP-FTOC (ca. 30%) operation (note that the CO conversion was also different), as shown in Figure 4. This result is consistent with our

group's previous investigations of SC-FT in that the $CO_2$ selectivity is decreased relative to GP-FT. Again, this can be attributed to the better heat management in the supercritical phase operation thereby suppressing side reactions that affect $CO_2$ generation. In addition, the $CO_2$ selectivity did not show an increasing trend as a function of time on stream (over a 100+ hour period) in the supercritical operations, which is different than that observed in the gas phase operations where there is a modest increase in $CO_2$ selectivity with time on stream. This observation indicates that the catalyst deactivation rate may be lower in the supercritical phase operations than in the gas phase operations. This may be due to better heat transfer (so as to prevent the formation of the hot spots) and better mass transport (so as to inhibit loss of catalytic active sites by removing heavy products and coke precursors). The methane selectivity was low in both of the supercritical phase operations, below 4%, as shown in Figure 5. Methanation and cracking reactions are promoted by high temperature operation, and as such, temperature uniformity within the catalytic reaction beds is important in suppressing methane formation. The results in Figure 5 indicate that better heat management is obtained in supercritical phase operations as a result of the integration of the superior properties of the supercritical fluid medium into the FTS and FTOC processes.

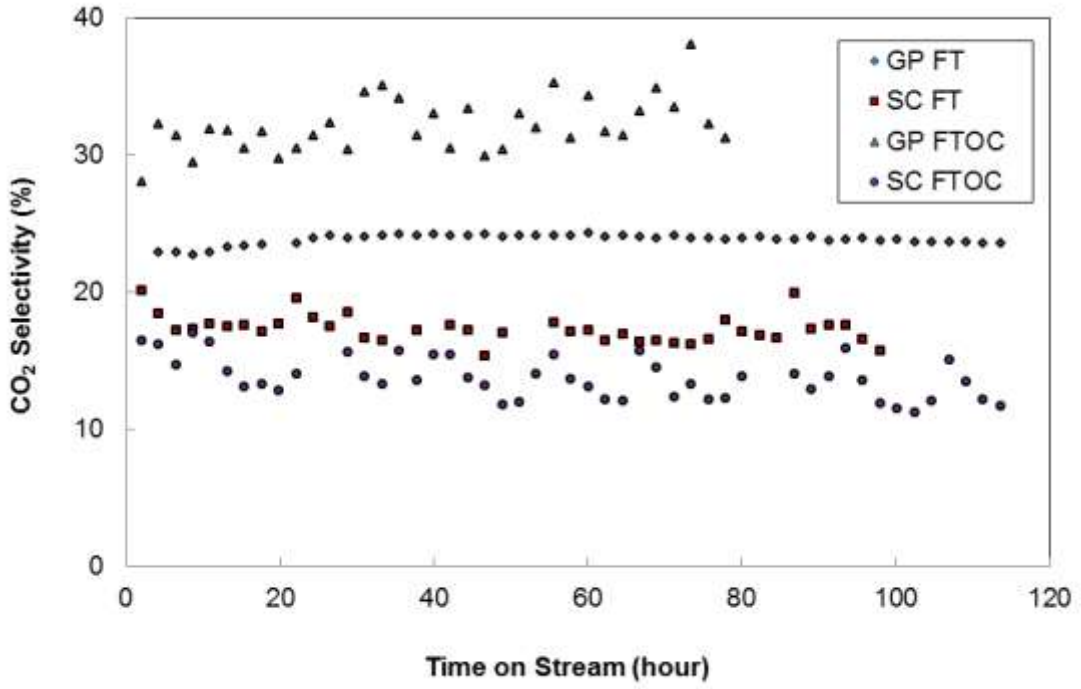


Figure 4. $CO_2$ selectivity as a function of time on stream for gas phase Fischer-Tropsch synthesis (GP-FT), gas phase Fischer-Tropsch synthesis with oligomerization and hydrocracking/isomerization (GP-FTOC), SC-FT and SC-FTS with oligomerization and hydrocracking/isomerization (SC-FTOC).

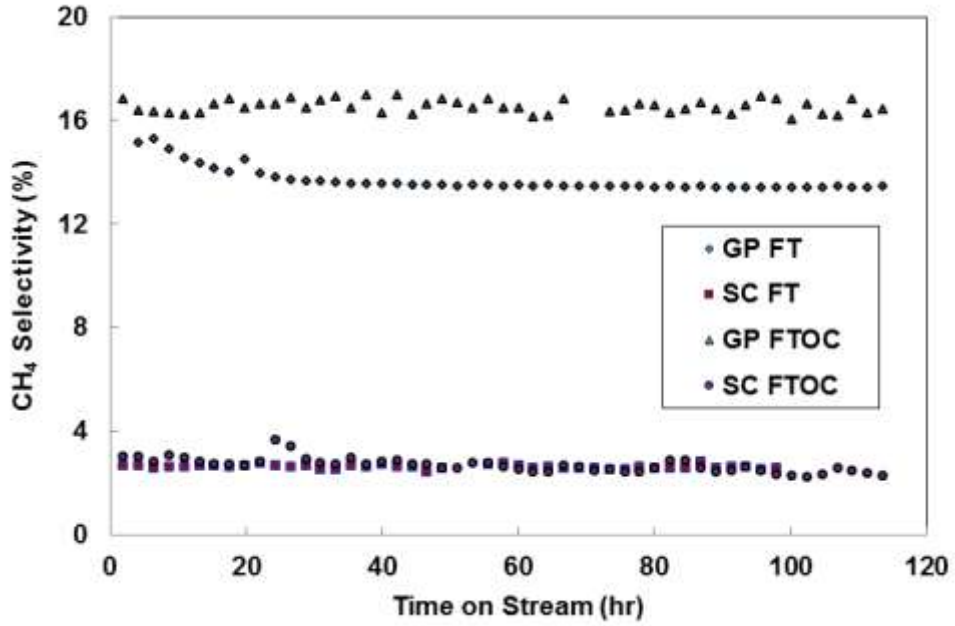


Figure 5. $CH_4$ selectivity as a function of time on stream for gas phase Fischer-Tropsch synthesis (GP-FT), gas phase Fischer-Tropsch synthesis with oligomerization and hydrocracking/isomerization (GP-FTOC), supercritical phase Fischer-Tropsch synthesis (SC-FT) and supercritical phase Fischer-Tropsch synthesis with oligomerization and hydrocracking/isomerization (SC-FTOC).

In both of the supercritical phase operations, $CH_4$ and $CO_2$ selectivity were reduced compared to GP-FT and GP-FTOC indicating that more carbon from CO was converted into heavier hydrocarbons, particularly in light of the higher CO conversion. Table 2 provides a summary of the experimental results of the GP-FT, GP-FTOC, SC-FT and SC-FTOC studies. It is noted that the CO conversion, $CH_4$ and $CO_2$ selectivity listed in table 2 are average values over the whole operation period.

A high propagation probability ($\alpha$ value of 0.94) was observed in SC-FT, as determined by the analysis of the liquid products using GC-FID and GC-MS. This $\alpha$ value is higher than that obtained in the GP-FT ($\alpha$ value of 0.78). This result is in keeping with literature that indicates that the liquid products shift towards the heavy hydrocarbon range under supercritical phase conditions. Figures 6 and 7 present product selectivities as a function of carbon number for GP-FT and SC-FT, respectively. These results indicate that using the supercritical fluid as the reaction medium can promote the carbon chain growth during the FT synthesis.

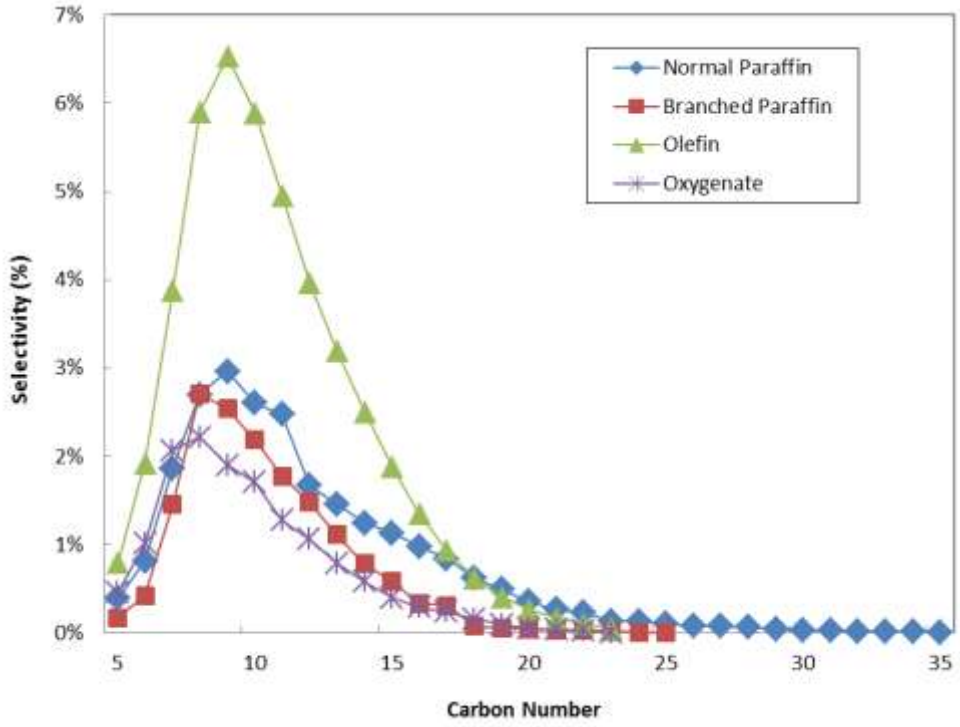


Figure 6. Liquid products selectivities from gas phase Fischer-Tropsch synthesis (GP-FT).

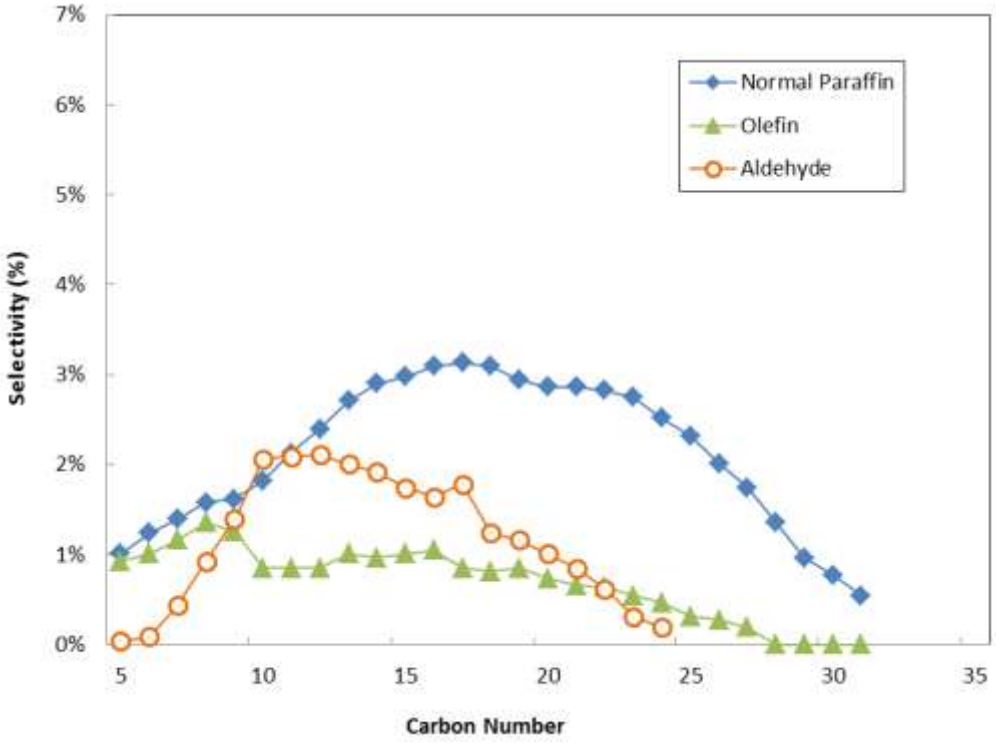


Figure 7. Liquid products selectivities from supercritical phase Fischer-Tropsch synthesis (SC-FT).

Consistent with our previous experience in operating SC-FT using an iron-based catalyst, a significant concentration of aldehyde (23.6%) was detected in the liquid products (rather than other oxygenates typically obtained from GP-FT such as alcohols). Our previous results show that these aldehydes are actually intermediates that are generated in the FTS reactions, which can be further converted to other oxygenates or olefins depending on various factors including residence time, catalyst acidity, and operating condition. We have found that the enhanced solubility afforded by the use of the supercritical fluid as the reaction medium allows these aldehydes intermediates to be efficiently solvated by the supercritical hexanes and extracted from the catalyst active sites and carried out of the catalyst bed as one of the reaction products. Durham et al. showed that aldehydes are primary products on an Fe-based catalyst under these SC-FT conditions, which are then converted to other oxygenates and olefins and be subsequently transformed into paraffins through secondary reactions.

Hydrocarbon product selectivity (expressed as mole percentage of a given compound or a group of compounds), and CO conversion obtained in these four tests are shown in Table 2. The synthesis gas flow rate for each of these four tests was kept constant at 50 SCCM in order to maintain the same apparent residence time.

**Table 1 CO conversion and product selectivities from Fischer-Tropsch synthesis with and without subsequent oligomerization and hydrocracking/isomerization stages under gas phase and supercritical phase conditions.**

| Operation Phase | Gas Phase | Gas Phase | Supercritical Phase | Supercritical Phase |
|---|---|---|---|---|
| Reaction Stages | FT[c] | FTOC[d] | FT[c] | FTOC[d] |
| X CO (%)[a] | 31.5 | 33 | 75 | 84 |
| S $CO_2$ (%)[b] | 23 | 32 | 17 | 13 |
| S $CH_4$ (%) | 14 | 17 | 3 | 3 |
| S $C_2$-$C_4$ (%) | 13.5 | 9.5 | 2.1 | 3.7 |
| S $C_5$-$C_{11}$ (%) | 27.5 | 12.2 | 23.8 | 27.5 |
| S $C_{12}$-$C_{22}$ (%) | 21.3 | 26.8 | 40.5 | 42.7 |
| S $C_{22}$+ (%) | 0.6 | 2.3 | 13.6 | 10.1 |
| S Normal Paraffin (% of $C_{5+}$ products) | 24.0 | 47.9 | 57.6 | 53.8 |
| S Olefin (% of $C_{5+}$ products) | 45.6 | 10.5 | 18.6 | 30.5 |
| S Branched Paraffin (% of $C_{5+}$ products) | 16.3 | 31.2 | - | 5.3 |
| S Alcohol (% of $C_{5+}$ products) | 14.8 | - | - | - |
| S Aldehyde (% of $C_{5+}$ products) | - | - | 23.6 | - |
| S Aromatics (% of $C_{5+}$ products) | - | 10.4 | - | - |
| S cyclo Paraffin (% of $C_{5+}$ products) | - | - | - | 10.3 |

a: X stands for conversion
b: S stands for selectivity
c: FT stands for Fischer-Tropsch synthesis
d: FTOC stands for Fischer-Tropsch synthesis with subsequent oligomerization and hydrocracking/isomerization

After introducing the catalytic oligomerization and hydrogenation reaction beds, the olefin selectivity was greatly reduced in GP-FTOC (Figure 8) compared to GP-FT (Figure 6). As shown in table 2, the olefin selectivity for the $C_{5+}$ liquid products decreased from 45.6% in GP-FT to 10.5% in GP-FTOC. In GP-FT, terminal olefins are predominant, while in GP-FTOC, internal olefins (middle olefin, etc) are also observed. The introduction of the oligomerization bed and the hydrocracking bed effectively modified the total olefin yield, thus, the olefin concentration is greatly reduced in the GP-FTOC products in which case the olefin concentration can better meet the olefin content limit in certain fuel regulations.

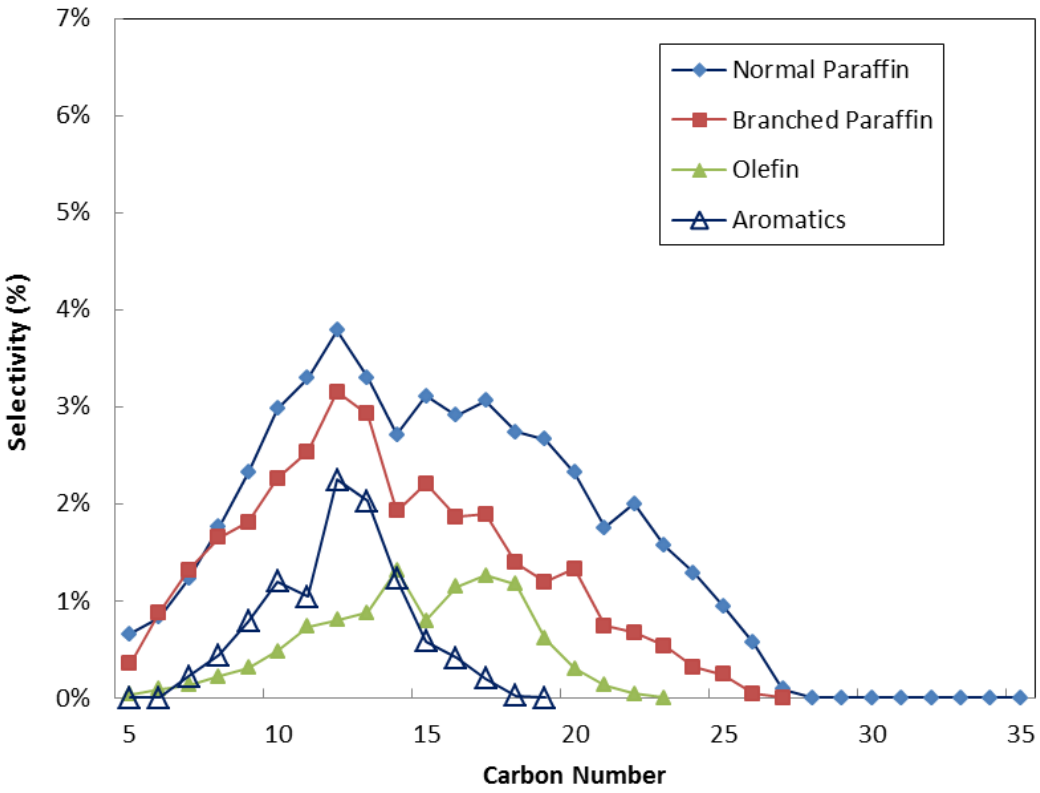


Figure 8. Liquid products selectivities from gas phase Fischer-Tropsch synthesis with subsequent oligomerization and hydrocracking/isomerization stages (GP-FTOC).

As shown in table 2, the olefin selectivity in SC-FT was around 18.6%, which was significantly less than that in GP-FT (45.6%). However, recall that the aldehyde selectivity was 23.6% under these conditions, and, in light of previous work, there appear to be aldehydes (which are produced as the primary product) that have not been converted to olefins under these SC-FT conditions. We note that the sum of the olefin selectivity and the oxygenate selectivity in this SC-FT experiment ($S_{olefin}$ +$S_{aldehyde}$ = 42.2%) was about 18% less than the value from the GP-FT experiment ($S_{olefin}$ + $S_{alcohol}$ = 60.4%). In addition, the paraffin selectivity (either normal paraffin or the sum of the normal paraffin and the branched paraffin) in the SC-FT experiment is higher than that in the GP-FT experiment, as shown in table 2. All together, the data show that hydrogenation is enhanced under these SC-FT conditions when compared to GP-FT. This observation is consistent with the fact that supercritical reaction solvents have be exploited for elimination interphase gas-liquid mass transport resistances so that it is possible to perform solid catalyzed hydrogenation with enhanced productivity. It is also in keeping with the suggestion that the enhanced readsorption of 1-olefins on the active sites can enhance the secondary reactions such as hydrogenation compared to gas phase operations. It is worth noting that both enhanced products extractability (desorption) and products readsorption can result from utilization of supercritical fluid solvent, though there should be a balance which is dependent on the reaction conditions. Moreover, due to the enhanced solubility and mass transport that can occur under supercritical phase conditions (compared to gas phase operation), the reaction intermediates can more readily readsorb on catalytic active sites therefore bringing about further carbon chain growth, and thus higher α-value in SC-FT compared to GP-FT. The bigger the

carbon number of the reaction intermediates, the longer residence time (as a result of slower diffusion rate) they will have within the catalysts thereby resulting in a higher probability of being hydrogenated. Overall, the product distribution shifts to longer chain hydrocarbons in SC-FT compared to that in GP-FT, which is consistent with general observations that have been made in supercritical phase Fischer-Tropsch synthesis by several research groups.

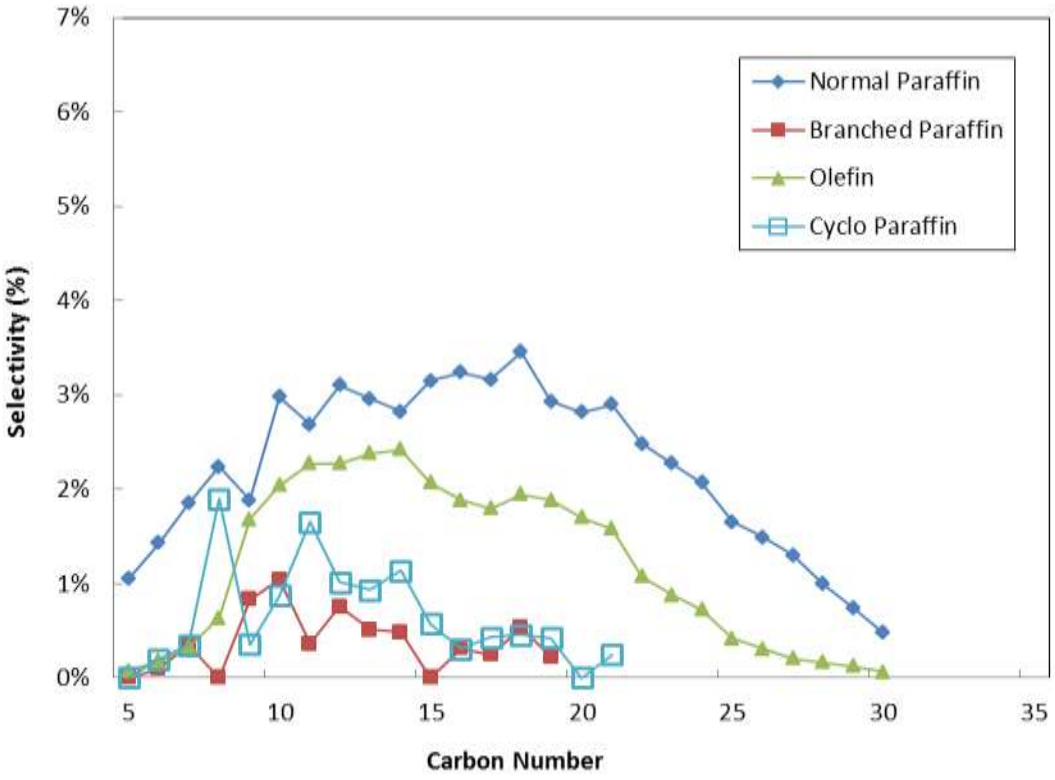


Figure 9. Liquid products selectivities from supercritical phase Fischer-Tropsch synthesis with subsequent oligomerization and hydrocracking/isomerization stages (SC-FTOC)

It has been reported that at 60 bar the oligomerization reaction using an ASA catalyst showed higher activity and better activity maintenance than that at 40 bar. Based on this, the oligomerization conversion would be expected to be higher in supercritical phase operation than that in gas phase since the system total pressure is higher. However, the results from SC-FTOC in table 2 show that the use of the supercritical phase reaction media resulted in a higher selectivity towards $C_{5+}$ olefins (30.5%) compared to GP-FTOC conditions (10.5%), noting that the CO conversions were different with values of 75% and 31.5%, respectively. This higher olefin selectivity in SC-FTOC could result from either olefinic products being generated from the cracking/isomerization reactions (as reaction intermediates as discussed below), or due to a suppression of the oligomerization function because of the presence of the supercritical medium (however, the later is not consistent with the positive effect of pressure on ASA catalyzed oligomerization).

The normal paraffin selectivity was increased from 24.0% in GP-FT to 47.9% in GP-FTOC due to the introduction of the hydrocracking reaction bed (on the 1 wt. % Pd/ASA catalyst) which

brings about hydrogenation of olefinic products and hydrogen-unsaturated hydrocarbons. The noble metal, in this case palladium, mainly contributes to hydrogenation as it is active towards electron transfer. The difference in the normal paraffin selectivities between the SC-FT (57. 6%) and the GP-FT (24.0%), and between the SC-FTOC (53.8%) and the GP-FTOC (47.9%) indicate that the supercritical phase operations exhibit higher hydrogenation activity. As widely discussed in other supercritical phase Fischer-Tropsch synthesis literature, reduced interphase gas-liquid mass transport resistance and enhanced hydrogen diffusivity can be contributing factors.

Due to the polymerization nature of FT synthesis, it is not particularly selective towards fuel range hydrocarbons. Additionally, the FT fuel that is produced possesses certain quality issues for use as both gasoline and diesel fuel, including poor cold-flow properties (cloud point, pour point, cold filter plugging point, etc.), low lubricity and low density, etc.. Increasing the content of branched hydrocarbons in FT fuels can improve these cold-flow properties. Branched hydrocarbons, especially asymmetrical isomers, are more difficult to crystallize than linear paraffins of the same molecular weight, and therefore possess a lower melting point and congealing point than linear paraffins. In addition, asymmetric branched hydrocarbons and most substituted cyclic hydrocarbons contribute to the lubricating capacity of fuels. Yet, the paraffinic hydrocarbons generated from FT synthesis are highly linear. As a result, typically derived FT hydrocarbon fuels that contain low content of branched compounds offer poor cold-flow properties and low lubricity. Various fuel additives can be added into the FT fuel blends to improve the cold-flow properties and lubricity, such as methyl ester. Aromatics can be used to increase the fuel density and octane number along with the other fuel additives.

In GP-FTOC, a significant amount of branched paraffin was generated. The branched paraffin selectivity in the GP-FTOC experiment increased from 16.3% in GP-FT up to 31.2% by adding the hydrocracking/isomerization stage. The branched paraffin types that were collected in GP-FTOC include 2-methyl-, 3-methyl-, 4-methyl-, 2-dimethyl-, 2,3-dimethyl, 4-ethyl-, etc. For the fuel range (in the carbon number range from 5-22) the branched paraffin selectivity was significantly promoted. In SC-FTOC, the presence of the supercritical solvent allows for efficient extraction of reaction intermediates and products (as was also the case in SC-FT), such that cyclo-paraffins (1-R, 2-R, cyclopropanes) and more olefins were collected as reaction intermediates from the cracking/isomerization reactor bed. This observation is consistent with the mechanisms described in the literature. It is well recognized that isomerization of n-paraffins is the first reaction step in this process while cracking is a subsequent reaction. Mono-branched paraffins show a lower tendency towards cracking than multi-branched paraffins. The bifunctional catalysts commonly used for hydrocracking/isomerization often contain metallic sites (for hydrogenation/ dehydrogenation) and acid sites (for skeletal isomerization via carbenium ions), in this case, Pd and ASA, respectively. In one of the popular cracking/isomerization pathways that has been proposed, paraffins are first activated and dehydrogenated on the metal sites, then the generated olefin intermediates protonate to corresponding carbenium ions (usually cyclic) on the acid sites. Through intramolecular reactions and intermolecular reactions, the carbenium ions are hydrogenated or dehydrogenated to produce branched paraffins with corresponding carbon number. The intramolecular reactions include type A rearrangements: hydride shift and alkyl shift, and type B rearrangements: PCP (protonated cyclopropane) branching and cracking by β - scission. In this study, the SC-FTOC results are consistent with this mechanism by having exhibited the presence of cyclo-paraffins

(1-R, 2-R, cyclopropanes) and the enhanced olefin selectivity. Note that there were negligible amounts of these cyclo-paraffins observed in GP-FT and GP-FTOC.

Though the isomer selectivity (isomerization activity) was substantial, the cracking of long chain hydrocarbons ($C_{22+}$) was insignificant when comparing GP-FTOC with GP-FT. Yet, the $C_{22+}$ product selectivity was higher in GP-FTOC than that in GP-FT, which suggests that the oligomerization activity was high for middle range compounds that were converted into $C_{22+}$ products to an extent greater than the cracking of the $C_{22+}$ compounds. However, the GP-FTOC $C_{26+}$ product selectivity (0.1%, not listed in Table 2) was lower than that in GP-FT(0.3%, not listed in Table 2), which means that hydrocracking using this Pd/ASA catalyst under these gas phase conditions favors the cracking of the heavier hydrocarbons ($C_{26+}$). This result is consistent with the observation that the heavier hydrocarbons are more likely to be involved in cracking. Under supercritical phase conditions, the selectivity of $C_{22+}$ compounds in SC-FTOC was 10.1% compared to 13.6% in SC-FT, thereby illustrating the impact of having introduced the hydrocracking stage. It is important to note that the production of $C_{22+}$ hydrocarbons was significantly greater in SC-FT than in GP-FT, as described above, yet the activity of the hydrocracking stage under supercritical conditions was sufficient to lower the overall $C_{22+}$ hydrocarbon selectivity. The balance between cracking and isomerization can be modified to further affect the product distribution by adjusting the catalyst for hydrogenation/dehydrogenation activity (noble metal) vs. the isomerization activity (acid sites).

There were some aromatics produced in the gasoline and jet fuel range in the GP-FTOC experiment, which can enhance the density of the derived FT fuels. Identified aromatics ranged from $C_7$-$C_{12}$, including toluene, ethyl-benzene, p-xylene, o-xylene, 1-ethyl, 3-methyl-benzene, 1,3,5-trimethyl-benzene, 1,3-diethyl-benzene, 1-methyl,4-propyl-benzene, 1-methyl, 4-(1-methylethyl)-benzene, pentamethyl-benzene, etc. Quantitatively, the aromatics concentration (as identified by GC-MS) was approximately 35% of the $C_7$-$C_{12}$ hydrocarbons. However, the generation of aromatics was only observed in the GP-FTOC operation. Potential contributing factors are that the aromatization process was suppressed thermodynamically or that the concentrations of reactants for aromatization were too low such that there were no distinguishable aromatics generated under supercritical phase conditions.

In examining the liquid products as a function of carbon number, it can be seen that gasoline range ($C_5$-$C_{11}$) products was dominate in GP-FT while diesel range ($C_{12}$-$C_{22}$) was more prominent in GP-FTOC. In both SC-FT and SC-FTOC, the selectivity towards liquid products was greatly enhanced due to lower production of gas phase products. This is especially true for SC-FTOC where the fuel range products were further intensified through higher selectivity towards gasoline range and diesel range products and less heavy hydrocarbon ($C_{22+}$) production compared to SC-FT.

**Summary:**

This study demonstrates that Fischer-Tropsch synthesis with subsequent oligomerization and hydrocracking/isomerization stages (FTOC) can be effectively performed using a newly designed three-bed catalytic reactor system. This three-bed reactor system consists of three

sequential fixed bed reactors (arranged vertically), using 1g Fe-based FT catalyst in the first FT stage, 1g ASA catalyst in the second oligomerization stage and 1g of 1.0 wt.% Pd/ASA catalyst in the hydrocracking/isomerization stage. This integrated FTOC process provides opportunities to effectively modify the Fischer-Tropsch synthesis product. For instance, the liquid product $C_{5+}$ olefin selectivity was observed to be greatly reduced to 10.5% in gas phase FTOC (GP-FTOC) compared to 45.6% in gas phase Fischer-Tropsch synthesis (GP-FT). The selectivity towards branched paraffins, which can help to improve the fuel's cold flow properties and lubricity, was significantly promoted to ca. 31.2% through the implementation of the hydrocracking and isomerization stages in the GP-FTOC experiment compared to 16.3% in the GP-FT experiment. In addition, appreciable amounts of aromatics, which can enhance the fuel density, were produced in the gasoline and jet fuel range ($C_5$-$C_{15}$) in the GP-FTOC experiment. The selectivity towards long chain hydrocarbons ($C_{26+}$) that are typically produced in GP-FT was diminished due to the introduction the hydrocracking stage. Overall, this work demonstrates that the resulting product distribution can be distinguishably modified towards fuel range products in GP-FTOC through the integration of the oligomerization and hydrocracking/isomerization stages immediately subsequent to FTS.

Consistent with related work in the literature, the utilization of supercritical fluid (SC) media (in this case supercritical hexanes) in Fischer-Tropsch synthesis (SC-FT) was shown to reduce the selectivity towards $CH_4$ and $CO_2$ compared to gas phase Fischer-Tropsch synthesis (GP-FT). Moreover, SC-FT resulted in a shift in the product distribution towards longer chain hydrocarbons along with an enhanced normal paraffin selectivity compared to GP-FT. These results indicate improved carbon chain propagation probability and elevated hydrogenation under supercritical phase conditions. Additionally, in accordance with our previous experience in operating SC-FT on an iron catalyst, a significant concentration of aldehyde (23.6%) was detected in the SC-FT liquid products (rather than the other oxygenates typically obtained from GP-FT such as alcohols). In the case of SC-FTOC, higher concentrations of cyclo-paraffins (1-R, 2-R, cyclopropane) and olefins were observed in the liquid effluent from the cracking and isomerization stage, when compared to the liquid obtained from the GP-FTOC. The selectivity towards $C_{22+}$ hydrocarbons was distinguishably less under SC-FTOC conditions compared to SC-FT. Overall, this work illustrates that the selectivity towards fuel rage hydrocarbons ($C_5$-$C_{22}$) can be enhanced in SC-FTOC while simultaneously reducing the selectivity towards the undesired products of $CH_4$ and $CO_2$.

**Students Supported by DOE Contract No. DE-FC26-05NT42456**

1. **Jennifer Boice, Ph.D**., Current Ph.D. Student
   Dissertation Title: Synthesis and Processing of Cobalt Nanoparticles in Functional Solvents for Catalysis Applications
2. **Sihe Zhang, Ph.D. 2012**
   Dissertation Title: Supercritical Fischer Tropsch Synthesis with Integrated Upgrading

Employment post graduation: Postdoctoral Fellow with Professor Iglesia at U. California Berkeley.

3. **Rui Xu, Ph.D. 2012**
   Dissertation Title: Supercritical Phase Mixed Alcohol Synthesis Using Cu Based Catalysts
   Employment post graduation: Postdoctoral Fellow at the Auburn Center for Bioenergy and Bioproducts.
4. **Deborah Bacik, Ph.D. 2011**
   Dissertation Title: Incorporating Green Chemistry Principles in Heterogeneous Catalysis Operations
   Employment post graduation: Engineer with the Bacik Group.
5. **Joseph E. Durham, Ph.D. 2010**
   Dissertation Title: Supercritical Fluids for Fischer Tropsch Synthesis and Related Reactions
   Employment post graduation: Evonik Industries
6. **Kendall M. Hurst, Ph.D. 2010**
   Dissertation Title: Nanoparticle Synthesis and Surface Modifications
   Employment post graduation: Chevron-Phillips Chemical Company
7. **Daniel Obrzut, Ph.D. 2008**
   Dissertation Title: Investigation of the Underlying Phenomena of Precipitation in Supercritcal Fulids
   Employment post graduation: Abbott Laboratories
8. **Madhu Anand, Ph.D. 2007**
   Dissertation Title: Synthesis, Fractionization, and Thin Film Processing of Nanoparticles Using the Tunable Solvent Properties of Carbon Dioxide Gas Expanded Liquids
   Employment post graduation: Conoco Phillips Corporation

**Publications**

1. Durham E., Xu R., Zhang S., Eden M.R., Roberts C.B. (2013): "Supercritical Adiabatic Reactor for Fischer-Tropsch Synthesis", *Industrial & Engineering Chemistry Research* (published online October 10, 2012, DOI: 10.1021/ie3008677).
2. Durham E., Zhang S., Xu R., Eden M.R., Roberts C.B. (2012): "Novel Adiabatic Reactor Design for Supercritical Fischer-Tropsch Synthesis", *Computer Aided Chemical Engineering*, 30B, pp. 1098-1102.
3. Durham, E.; Roberts, C.B.; "Supercritical Activity Restoration for Fischer Tropsch Synthesis", International Journal for Reactor Engineering, 10, A19, 2012.
4. Yuan W., Vaughan G.C., Roberts C.B., Eden M.R. (2011): "Modeling and Optimization of Supercritical Phase Fischer-Tropsch Synthesis", *Computer Aided Chemical Engineering*, 29B, pp. 1929-1933.
5. Bacik, D.B.; Yuan W.; Roberts, C.B.; Eden, M.R.; "Systems Analysis of Benign Hydrogen Peroxide Synthesis in Supercritical CO2", Computer Aided Chemical Engineering, 29A, 387-391, 2011.

6. Liu, J.; Ruffini, N.; Pollet, P.; Llopis-Mestre, V.; Dilek, C.; Eckert, C.A.; Liotta, C.L.; Roberts, C.B.; "More Benign Synthesis of Palladium Nanoparticles in Dimethyl Sulfoxide and Their Extraction into an Organic Phase," Industrial and Engineering Chemistry Research, 49(17), 2010.
7. Durham, E.; Zhang, S.; Roberts, C.B., "Diesel-Length Aldehydes and Ketones via SCF-FTS on an Iron Catalyst." Applied Catalysis A., 386 (1-2), 2010.
8. Durham, E.; Roberts, C.B., "Diesel-length aldehydes from SCF-FTS on an iron catalyst." Preprints of Symposia - American Chemical Society: Division of Fuel Chemistry, 2010.
9. Elbashir, N.O.; Bukur, D.B.; Durham, E.; Roberts, C.B.; "Advancement of Fischer-Tropsch Synthesis using Supercritical Fluid Reaction Media." AIChE Journal, 56(4), 2010.
10. Feng He, Juncheng Liu, Christopher B. Roberts, and Dongye Zhao, "One Step Green Synthesis of Pd Nanoparticles of Controlled Size and their Catalytic Activity for Trichloroethene Hydrodechlorination" Ind. Eng. Chem. Res., (2009), 48, 6550.
11. Kitchens, C. L., Roberts, C. B.; Liu, J.; Ashurst, W.R.; Anand, M.; Von White, G.; Hurst, K.M.; Saunders, S.R., "Application of Gas Expanded -Liquids for Nanoparticles Processing: Experiment and Theory" In ACS Symposium series 1006, "Gas-Expanded Liquids and Near Critical Media: Green Chemistry and Engineering" Editors: Keith W. Hutchenson, Aaron M. Scurto, Editor, Bala Subramaniam. (2009)
12. Liu, Juncheng; He, Feng; Gunn, Tyler; Zhao, Dongye; Roberts B. Christopher, "Precise Seed-mediated Growth and Size-controlled Synthesis of Palladium Nanoparticles Using a Green Chemistry Approach" Langmuir, (2009), 25, 7116.
13. Anand, M.; You, S.S.; Hurst, K.M.; Saunders, S.R.; Kitchens, C.L.; Ashurst, W.R.; Roberts, C.B, "Thermodynamic Analysis of Nanoparticle Size Selective Fractionation Using Gas-Expanded Liquids", Industrial & Engineering Chemistry Research, 47 (3), (2008)
14. Liu, J.C.; He, F.; Durham, E.; Zhao, D.Y.; Roberts, C.B., "Polysugar-Stabilized Pd Nanoparticles Exhibiting High Catalytic Activities", Langmuir, 24 (1), (2008)
15. Liu, J.C.; Sutton, J.; Roberts, C.B., "Synthesis and Extraction of Monodisperse Sodium Carboxymethylcellulose-Stabilized Platinum Nanoparticles for the Self-Assembly of Ordered Arrays", Journal of Physical Chemistry C, 111 (31), (2007)
16. Durham, J.E.; Bordawekar, M.; Roberts, C. B.. "Effects of Super-Critical Fluid Extraction on the Activity and Selectivty of Fischer Tropsch Catalysts," Fuel Chemistry Preprints - American Chemical Society, 52(2), (2007).
17. Dutta, P.; Pal, S.; Seehra, M.S.; Anand, M.; Roberts, C.B., "Magnetism in Dodecanethiol-Capped Gold Nanoparticles: Role of Size and Capping Agent" Applied Physics Letters, 90 (21): Art. No. 213102, (2007).
18. He F.; Zhao, D.Y.; Liu, J.C.; Roberts, C.B. "Stabilization of Fe-Pd Nanoparticles with Sodium Carboxymethyl Cellulose for Enhanced Transport and Dechlorination of Trichloroethylene in Soil and Groundwater ," Industrial and Engineering Chemistry Research 46 (1), (2007)

**Performance Evaluation of Coal and Biomass Based Fuel Production Strategies**

Dr. Mario R. Eden and Dr. Christopher B. Roberts
Department of Chemical Engineering
Auburn University

Experimental researchers in the Consortium for Fossil Fuel Science (CFFS) developed novel technologies for the production of transportation fuels from coal and biomass. Many of these new technologies also have the potential for producing valuable co-products that can significantly increase the overall profitability of the process. Unfortunately, the economic and environmental viability of such new technologies are most often evaluated separately rather than in an integrated manner. In this project, we aimed to address this gap through the development of integrated system engineering strategies for modeling, integration and optimization of fuels production from coal and biomass. The complexity of the co-product allocation problem for such processing facilities demanded a process systems engineering approach utilizing process integration and mathematical optimization techniques to ensure a targeted approach and serve as an interface between theoretical modeling/simulation work and the experimental efforts. In our work, a generic, robust optimization framework was developed that enables identification of economically optimal production schemes for carbon resource processing in hydrogen polygeneration plants. The flexibility of the developed framework enables a seamless transition to focus on general fuels production. We adapted the original framework was adapted to enable evaluation of the novel coal/biomass conversion technologies emerging from the experimental efforts in CFFS. The framework enables identification of the most profitable set of fuels and co-products to be manufactured given current market prices. By utilizing process integration methods, the processing steps were optimized to ensure efficient use of energy and materials resources. In addition, the framework serves as an important screening tool for directing further research, as enables ruling out certain production routes and/or co-products for either economic or environmental reasons. Furthermore, targeted solution approaches allow for identifying the specific performance characteristics required in a given subprocess for it to overcome economic and/or environmental restrictions.

We have developed a generic modeling framework that allows for representation of coal and/or biomass gasification processes for the production of the synthesis gas needed for subsequent downstream conversion to liquid fuels via Fischer-Tropsch Synthesis (FTS). Furthermore, models were developed for both gas-phase FTS and the Supercritical Phase FTS (SCF-FTS) under investigation in Dr. Christopher Roberts' laboratory at Auburn University. The focus of the modeling work has been on these processes as they provided the most comprehensive datasets. Economic and environmental impact analyses were performed for the two FTS processes to compare the performance benefits of the supercritical phase media to the current standard of gas-phase operation. Our work showed clearly that while the supercritical operating conditions results in an increased operational cost, the increased production rate of fuel range compounds makes up for it.

Process simulation models were developed for the traditional gas-phase FTS process (Gas-FTS) and for a novel supercritical phase FTS process (SCF-FTS). Detailed analyses of the process economics and environmental impact of the two FTS alternatives are performed to evaluate if the increased fuel production outweighs the increased operating costs resulting from higher temperatures and pressures. The simulation models for each process were developed by extracting knowledge on yield, conversion, and energy usage from empirical as well as experimental data collected in the Roberts Laboratory at Auburn University. The models include all feed pretreatment, conversion and product fractionation steps. Process integration techniques, i.e. thermal pinch analysis, are used to identify the minimum energy requirements and optimize the simulation models. Aspen Energy Analyzer is used to design the corresponding minimum cost heat exchanger networks. Finally, the optimized models are used to generate data for the economic as well as environmental performance metrics. The estimation of environmental performance is achieved through the use of the US-EPA Waste Reduction (WAR) algorithm. The Fischer-Tropsch reaction is a surface catalyzed polymerization type reaction, that produces longer chain hydrocarbons from synthesis gas (hydrogen and carbon monoxide):

$$(2n + 1)H_2 + nCO \rightarrow C_nH_{2n+2} + nH_2O$$

The fuel production models include all the feed pretreatment steps along with the reactors, i.e., FTS reactor and hydrocracker (to convert the heaviest hydrocarbon waxes back to lighter compounds), as well as fuel production fractionation units. The product distribution obtained from the FTS reactor is modeled using the Anderson-Schulz-Flory model, which is shown below with the chain growth probability (α) provided from the experimental studies in Dr. Roberts' laboratory.

$$W_n = n \cdot \alpha^{n-1}(1-\alpha)^2$$

where, $W_n$ represents the weight percentage of all hydrocarbon products with carbon number $n$ and $\alpha$ represents the chain growth probability. The downstream processing is focused on the production of two products, i.e. a gasoline range fuel and a jet fuel similar to JP-8. The heavy products are hydrocracked back to the middle distillate range, while the light compounds are reformed to produce additional synthesis gas (only in gas phase FTS), or recycled to the reactor to create the dense media for SCF-FTS.

Screenshots of the models developed in Aspen Plus are provided in Figure 3, Figure 4 and Figure 5 below. It should be noted that the initial SCF-FTS model presented in Figure 4 was intended to mimic the process configuration in Dr. Roberts' lab and as such the dense supercritical phase is established through the use of an external hexane solvent. Once the performance of this model was validated, the hexane stream was removed and replaced by a recycle stream composed of the light fraction from the SCF-FTS reactor product. The refined model is provided in Figure 5.

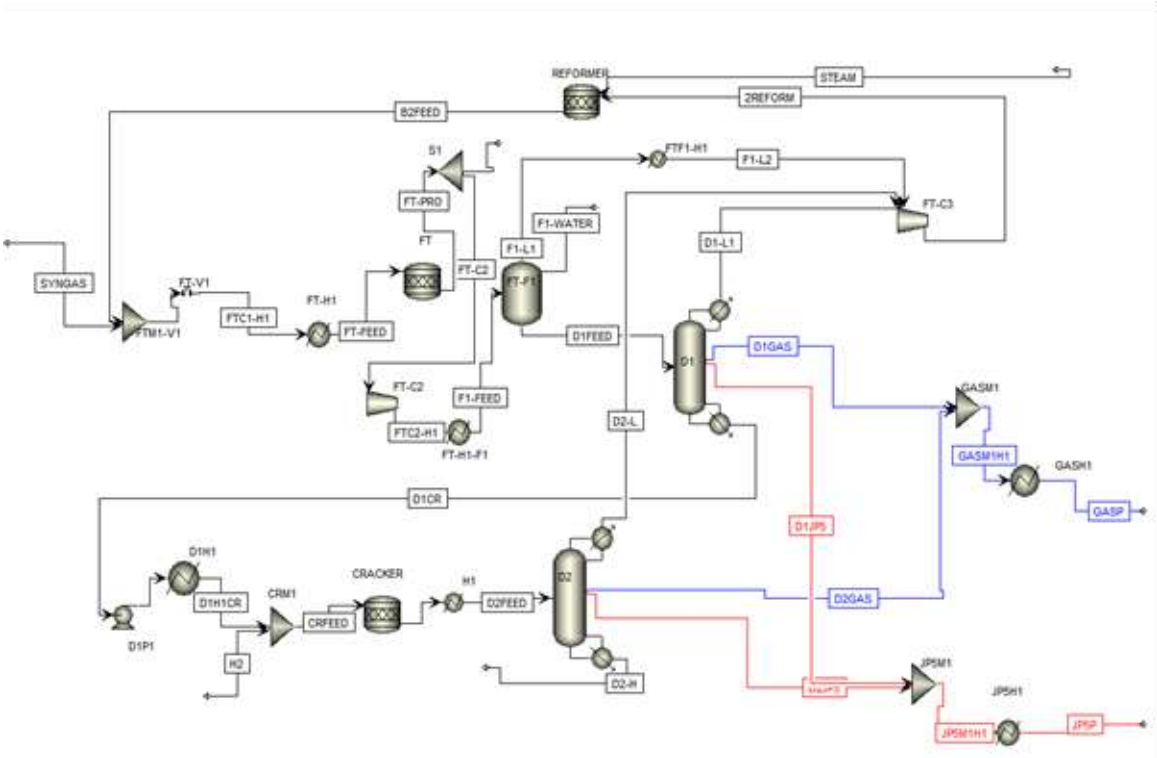


**Figure 3: Gas-phase FTS model developed in Aspen Plus.**

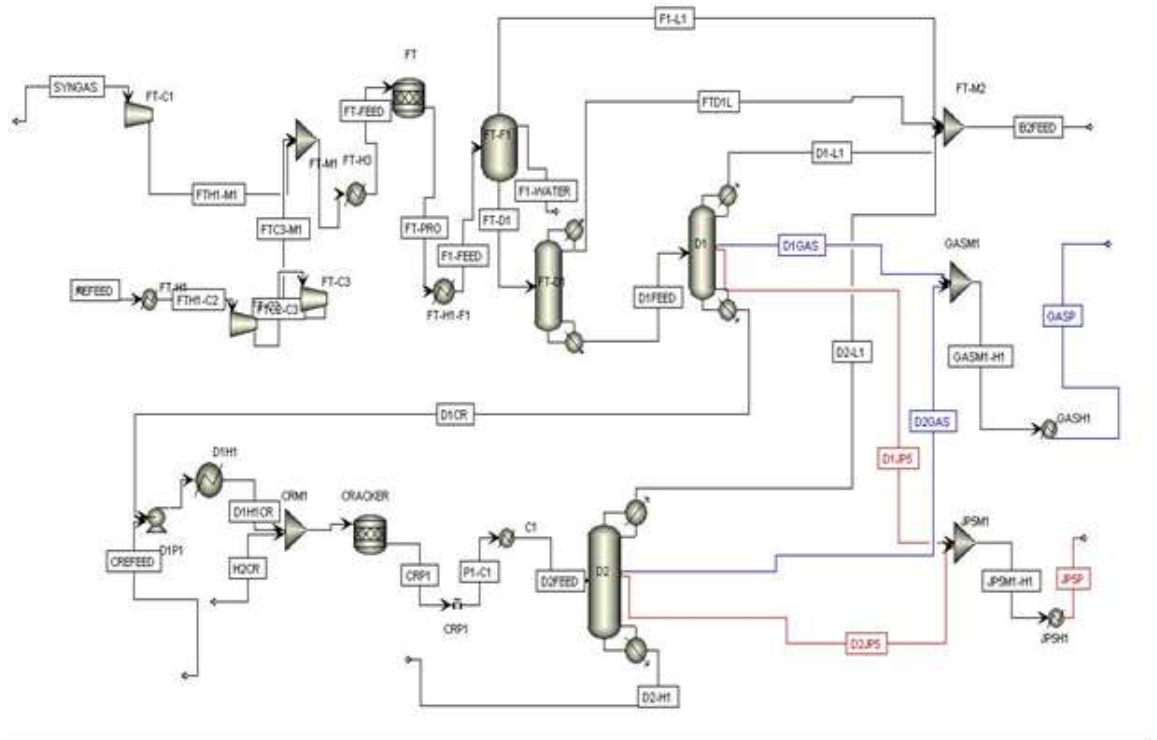

**Figure 4: Initial SCF-FTS model developed in Aspen Plus (uses hexane to create dense phase).**

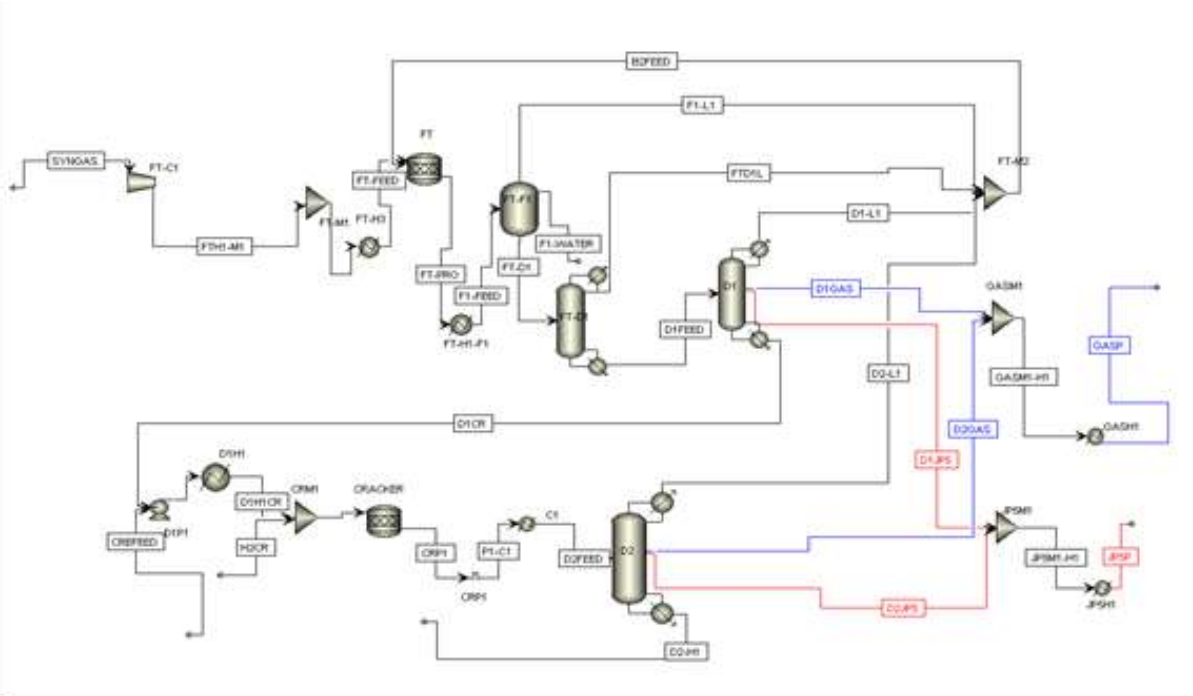

**Figure 5: Refined SCF-FTS model developed in Aspen Plus (dense phase created by recycling light fraction).**

In order to determine the optimal SCF-FTS operating conditions, simulation models are developed for a variety of reaction conditions based on the CO conversion at different pressures and temperatures based on the experimental data from Dr. Roberts' lab at Auburn. Sensitivity analysis was performed by varying the reaction temperature and pressure.

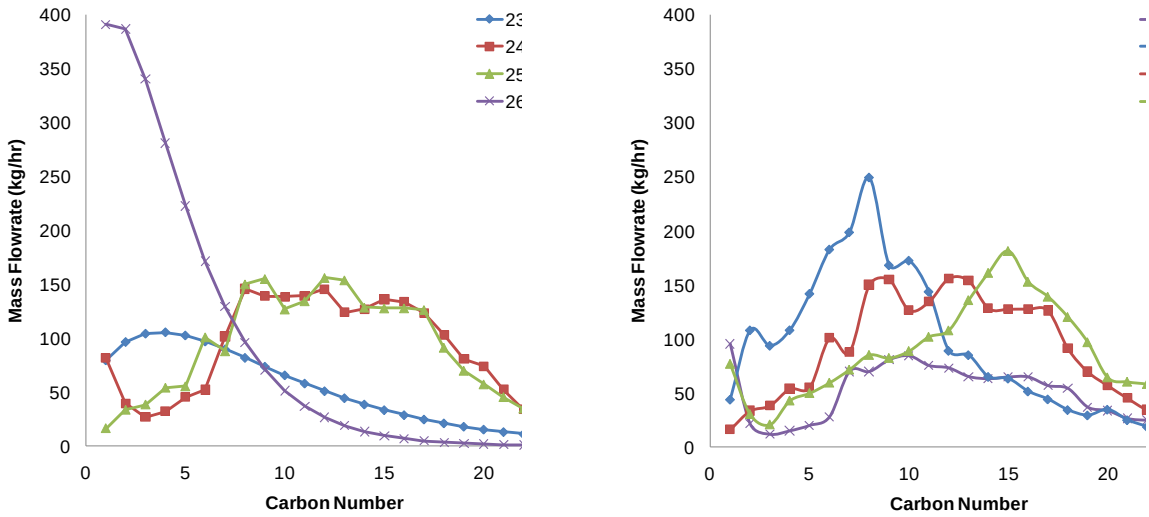

**Figure 6: SCF-FTS reactor simulation results of hydrocarbon product distribution changes with temperature and pressure; fixed pressure at 65 bar (left) and fixed temperature at 250°C (right).**

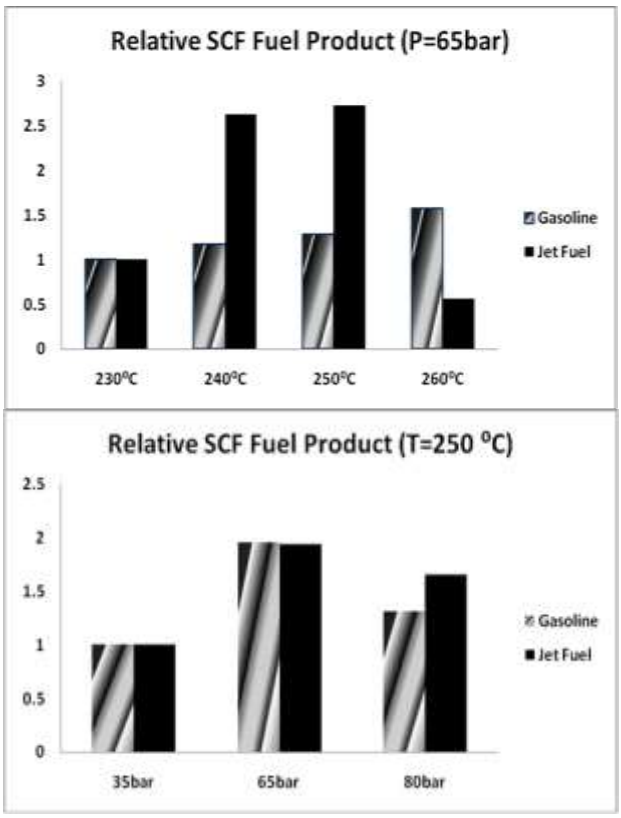


**Figure 7: SCF-FTS reactor simulation results of relative fuel product (gasoline and jet fuel) distribution changes with temperature and pressure; fixed pressure at 65 bar (left) and fixed temperature at 250°C (right).**

Figure 6 and Figure 7 shows the simulation results for different SCF FT reaction conditions. At a fixed pressure of 65 bar, by increasing the temperature from near the critical point (230°C, 240°C) to the supercritical region (250°C, 260°C), more fuel range hydrocarbons are produced. This is mainly because temperature affects the chain growth mechanism directly. It should be noted that there is an obvious optimal temperature at this pressure between 240 and 250°C, where the $C_6$-$C_{16}$ compounds are maximized. At higher temperatures the longer chain hydrocarbons decompose to produce a lot of methane. At a fixed temperature of 250°C, by increasing the pressure from below the critical point (35 bar) to the critical pressure (80 bar), the production distribution does not change as drastically, but more heavy hydrocarbons are still produced. This is due to the bed residence time (defined as the volume of feed at the applied pressure passing through the volume of the catalyst bed per second) is influenced by the total pressure which affects the equilibrium of the FTS products. The results indicate that the SCF-FTS reactor produces the largest amount of fuel range products at 250°C and 65 bar.

Economic analyses of both case studies were performed to evaluate the fuel production cost. Standardized process economics methods were employed to translate the equipment and utility cost into the total production cost, which accounts for everything from engineering to construction, monitoring, supervision and operation. It should be noted that both the gas phase FTS process and the supercritical phase FTS process were modeled using the same synthesis gas feed, and as such the raw material cost are the same. Furthermore, the capital investments are similar for the two pathways as well (SCF-FTS is approximately 10% higher as a result of the pressure ratings of the equipment). This means that the major cost difference between the two processes lies in the utility cost. The results have been normalized in terms of the gas phase FTS process and are presented in Figure 8, where the production cost is defined per kg of fuel produced.

By operating the FTS reaction in the dense supercritical phase, the direct benefits are two-fold, i.e. vapor-like transport properties and liquid-like thermal properties. This results in a product distribution that is much narrower than traditional gas phase FTS, thus yielding a higher middle distillate (fuel) fraction. Therefore, with the same FT reactor feed, the fuel production rate of SCF-FTS model is approximately three times higher than the gas phase model. The significantly increased production rate results in a lower production cost per kg of fuel, which is approximately half of the gas phase production process.

The environmental impact of the two process options was also evaluated as shown in Figure 9. It is important to make sure that the comparison is performed on a per kg of product basis. The US-EPA WAR algorithm takes both the chemical process as well as the energy generation processes that provide the utilities into account. If the analysis is done in terms of the same feedstock amounts, then the SCF-FTS process is penalized significantly as a result of the higher utility requirements for both heating and compression. In general, the two processes have similar environmental impacts when evaluated per kg of fuel range products. The gas phase process has a higher impact from the chemical process due to the lower efficiency of the FTS reactor, while the supercritical phase process has a higher impact stemming from the energy generation process.

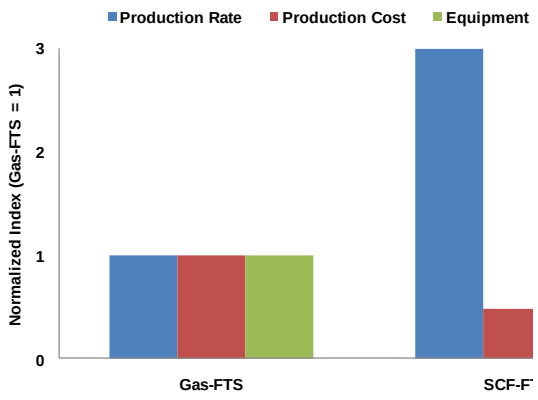


**Figure 8: Production rate and cost comparison for different FTS production processes.**

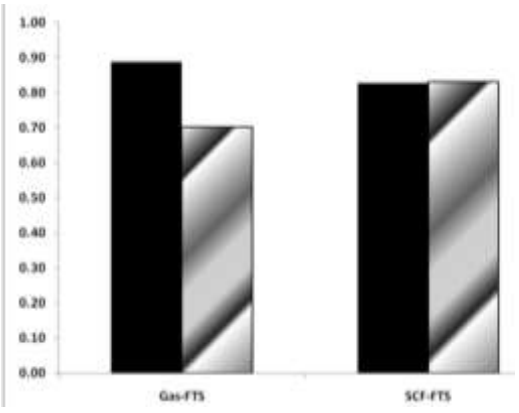


**Figure 9: Environmental impact per kg product ($I_{cp}$ and $I_{ep}$ are the chemical and energy processes respectively).**

The objective of this study was to evaluate the large scale potential of operating the Fischer-Tropsch synthesis reaction under supercritical phase condition and compare to the conventional gas phase configuration. Using a combination of literature and experimental data, models were developed for the entire fuel production process starting with the gasification of coal and/or biomass resources. The results show that although the SCF-FTS process is more energy intensive, the overall fuel production is reduced due to markedly increased production rate.

The analysis of the economic performance and energy usage of the FTS processes was provided above. The economic analysis showed that the capital expenditures for the gas phase FTS and supercritical phase FTS were similar using traditional process economics estimation techniques. The basis for the comparison was the Sasol ARGE reactor setup, which is a 900 bbl/day facility. The gas-phase process was developed using this scale and the experimental data obtained from Dr. Roberts' lab was used to develop the supercritical phase FTS model and then the flowrates were adjusted to match the processing rate of the Sasol process. Therefore the economics and equipment sizes were compared on a relative rather than an absolute basis. This was necessary for some specific units, e.g. the reactors as the detailed rate expressions were not available for the FT reaction schemes. In order to perform a detailed sizing of the reactor vessels this information is necessary, however shortcut methods based on volumetric gas flow, residence time and pressure drop were used to provide reasonable estimates instead.

We also studied the influence of the supercritical environment on the adiabatic temperature rise of the highly exothermic FTS reaction system. The presence of the supercritical fluid affords a sufficient dilution effect such that the adiabatic temperature rise can be reduced from 800°C (typical for GP-FTS operating at 50% CO conversion) to 30°C under supercritical operation at the same conversion level, thus making adiabatic operation feasible. Note that this involves 3.5 moles of hexane per mole of syngas. It should also be noted that adiabatic operation has been employed in FTS by recycling syngas or the produced liquid.

The traditional fixed bed FTS reactor design consists of a large number of parallel, narrow catalyst tubes. For example, the initial Sasol LTFT reactor (ARGE) managed the heat release by having a high velocity in a large number of narrow packed tubes, resulting in a reactor with 2050 12m long, 5cm ID tubes having a capacity of 900 BPD. In the supercritical adiabatic reactor (SCAR) design presented here, the catalyst would be loaded into fewer, larger tubes, with the reactor effluent then passing through a heat exchanger to remove the generated heat.

The SCAR reactor system is designed to match the catalyst bed length and total cross-sectional area of Sasol's ARGE reactor, while the heat exchangers were sized using standard dimensionless design expressions, i.e. the Colebrook and Dittus-Boelter equations:

$$f_f^{-0.5} = -4 \cdot \log\left(\frac{\varepsilon}{4.7D} + \frac{1.256}{N_{\mathrm{Re}}(f_f^{0.5})}\right)$$

$$Nu = 0.023 \cdot \mathrm{Re}^{0.8} \cdot \mathrm{Pr}^{0.3}$$

The reaction products were assumed to be water and 1-decene and the heat generation and adiabatic temperature rise were determined from literature values and simulations in Pro/II using the Peng-Robinson equation of state. In addition, the simulation studies yielded estimates of the bulk properties of the supercritical reaction media as follows: Density = 400 kg/$m^3$; viscosity = 0.0001 Pa·s; heat capacity = 2500 J/kg·K; thermal conductivity = 0.075 W/m·K. Moreover, boiling water at 28 bar (230$^o$C) was used as the heat transfer medium.

Four different design scenarios were considered. The first involved an analysis of the original ARGE design (for baseline comparison) consisting of 2050 12m long, 5cm ID tubes, while the second considered the same configuration upgraded for supercritical phase operation at the elevated pressures. The third design consists of a single module with one SCF-FTS reactor tube followed by a single heat exchanger designed to manage/dissipate a 30°C adiabatic temperature rise generated in the upstream reactor. This single module configuration operates between 240°C and 270°C and results in a logarithmic mean temperature difference of 21.6°C. The fourth design used six SCF-FTS reactor-heat exchanger modules in series, where each reactor consisted of single 2m long tube with 2.3m ID (same cross-sectional area as original ARGE design), while each heat exchanger was responsible for handling an adiabatic temperature rise of 5°C from the preceding reactor. This six module configuration operates between 240°C and 245°C, resulting in a logarithmic mean temperature difference of 12.3°C. From the simulation it was established that each heat exchangers employed in this 6 reactor SCAR system must manage a total duty of 2.2 MW. The heat exchangers were designed to consist of 128 0.062m ID tubes with a tube length of 9.74m yielding a overall drop of 0.005 bar per module and a total heat exchange area of 241 $m^2$ considering an overall heat transfer coefficient of 750 W/$m^2$·K.

Equipment pricing was performed using a combination of standard process economic estimation methods coupled with a cost estimate of \$130/$ft^2$ of heat transfer area for the high operating pressure in SCF-FTS. This estimated was provided by an industrial collaborator, and it should be noted that this is approximately twice the cost of corresponding equipment for the lower pressures used in GP-FTS.

**Table 1. Reactor and Heat Exchanger Cost Estimates for 4 Reactor Configurations**

| | ARGE | ARGE Modifieor SCF-FTS Operation | SCAR (Single Reactor Configuration) | SCAR (Multi-Reactor Configuration) |
|---|---|---|---|---|
| Number of Reactors | 1 | 1 | 1 | 6 |
| Pressure (bar) | 45 | 200 | 200 | 200 |
| Reactor Volume ($m^3$) | 48 | 48 | 48 | 8 |
| Adiabatic Temperature Rise (K) | N/A | N/A | 5 | 30 |
| Surface Area per Reactor ($m^2$) | 3864 | 3864 | 85.4 | 14.2 |

| | | | | |
|---|---|---|---|---|
| Reactor Cost | $2,700,000 | $5,500,000 | $240,000 | $40,000 |
| Number of Heat Exchangers | N/A | N/A | 1 | 6 |
| Surface area per HX ($m^2$) | N/A | N/A | 825 | 241 |
| Cost per HX | N/A | N/A | $1,160,000 | $340,000 |
| Equipment Cost | $2,700,000 | $5,500,000 | $1,400,000 | $2,300,000 |
| Equipment Cost ($/BPD) | $3,000 | $6,000 | $1,600 | $2,500 |

The traditional fixed-bed ARGE reactor was estimated to cost $3,000/BPD, while modifying the ARGE reactor design for the high pressure SCF-FTS resulted in a doubling of the cost to $6,000/BPD. The single SCAR reactor design which allowed for a 30°C adiabatic temperature rise at the assumed 50% CO conversion results in a reduction in capital investment to $1,600/BPD. The six-module SCAR reactor design which allowed only a 5°C adiabatic temperature rise, leads to a capital investment of $2,500/BPD. Each of the SCAR reactor configurations provides significant savings over either of the ARGE designs. The single SCAR reactor design allowed for the lowest cost given the greater logarithmic mean temperature difference across the heat exchanger, however it would need to be determined if this temperature rise would be acceptable for continuous operation or whether additional modules provide benefit due to greater thermal uniformity.

It should be noted that the size and cost values are only estimates and that the SCAR system has not been fully optimized at this time. Nonetheless, the supercritical adiabatic reactor system enables significantly lower capital investments compared to the traditional ARGE reactor upgraded for the high pressures necessary for supercritical phase operation.

Both the reaction and the heat removal processes have to be considered in the design and operation of the traditional fixed-bed ARGE reactor system. However, one of the advantages of this SCAR system is that it allows us to separate the reaction step from the thermal management step. As such, there is significant potential for added design flexibility that could lead to a more optimized and robust reactor/heat management system. For example, there is inherently more flexibility available for optimizing the catalyst design since the catalyst bed is no longer used as a means of heat transfer. Also, the lower pressure drop in the single tube SCAR system allows alternative catalyst structures to be employed. In addition to this, there are certain mechanical advantages to this single tube reactor system, such as the improved ease with which catalyst can be removed and replaced. Moreover, the multi-module SCAR configuration may yield additional advantages from an operational standpoint by allowing for the reactor inlet temperatures to be independently controlled accounting for differences in catalyst activity and feed compositions. Furthermore, some studies have indicated that when operating the FTS reaction under high chain-growth probability (α) conditions that single phase operation cannot be guaranteed

throughout the reactor due to the high molecular weight of the products. In this case, the multi-module configuration would allow for heavy products to be separated between modules through phase separation so as to not negatively impact the subsequent modules. Finally, additional levels of temperature control could be achieved by distributing the syngas feed to each module. This would enable the cooler syngas to partially absorb some of the generated thermal energy contained in the effluent the preceding reactor module. This would reduce the amount of heat exchanger capacity necessary for maintaining the desired overall temperature rise, and as such would further reduce the capital investment necessary.

In the work described above, we examined the operating costs associated with operating the Fischer-Tropsch Synthesis reaction under supercritical phase conditions compared to the conventional gas phase configuration. It was determined that even though the operating cost increases as a result of the higher pressure, the increased production of fuel range products more than makes up for this difference. These result coupled with the capital investment improvements shown here further illustrate the potential of the supercritical FTS process.

A novel supercritical adiabatic reactor design for Fischer-Tropsch Synthesis has been introduced, which illustrates significantly lower capital cost requirements compared to traditional fixed-bed FTS reactors under both gas-phase and supercritical phase scenarios. This system enables the benefits of SCF-FTS to be cost-effectively realized (e.g. suppressed methane production, increased selectivity towards higher value products like olefins and oxygenates, better thermal uniformity leading to reduced risk of runaway reactions, etc.) Additionally, this reactor configuration results in a more easily controlled and operated system due to improved thermal management and the simplicity of the mechanical design compared to conventional systems with large numbers of internal reactor tubes.

**Summary Statement**

We have performed simulation studies of a number of CFFS processes and used the generated information for process economic analyses of the performance. In the early stages of the project, several hydrogen production processes were simulated and evaluated, while in the later stages of the project, the focus was switched to the production of liquid fuels. Based on experimental data collected by other CFFS researchers, we developed process simulation models of both traditional gas-phase and supercritical phase Fischer-Tropsch Synthesis processes. Due to difficulties in aligning the available data with the requirements of the DOE baseline models, we chose to perform the economic comparisons by using established process economic estimation methods on both the traditional processes and the new processes developed within CFFS to provide a qualitative and quantitative evaluation. It was shown that the supercritical FTS (SCF-FTS) process exhibits very attractive economic performance in terms of the overall production costs per unit of liquid fuel. In addition, we studied the capital investments necessary if adiabatic operation of the SCF-FTS process was desired. Again, the presence of the supercritical media provided attractive performance attributes that illustrates the potential of this novel process.

**Students Supported by DOE Contract No. DE-FC26-05NT42456**

1. **Kristin H. McGlocklin, M.S.,** "*Process Integration and Optimization of Various Hydrogen Production Schemes*", December 2006. Ms. McGlocklin now works as a product engineer with 3M Corporation in Decatur, AL.

2. **Norman E. Sammons Jr., Ph.D**., "*A Framework for Optimal Biomass-based Polygeneration Facility Product Allocation*", December 2009. Dr. Sammons was the recipient of the prestigious EPA STAR Fellowship. Dr. Sammons was selected as one of only 25 US graduate students to receive an all-expense paid trip to attend the 2006 PASI workshop in Iguazu Falls, Argentina. Dr. Sammons was selected as an Auburn University Distinguished Outstanding Doctoral Student for 2007-2008 and was the recipient of the 2008-2009 Harry Merriwether Fellowship, which is the top award for Ph.D. students at Auburn University. Dr. Sammons now works as a process engineer with Codexis in San Francisco, CA.

3. **Wei Yuan, Ph.D.,** "*Modeling and Optimization of Novel Fuel Production Strategies*", December 2011. Dr. Yuan was selected as the 2011 Outstanding International Graduate Student for the Department of Chemical Engineering. Dr. Yuan is now working at Shell in Houston, TX.

4. **Susilpa Bommareddy, Ph.D.**, "*Property Integration for Simultaneous Process and Product Design*", expected 2013. Ms. Bommareddy is the recipient of the 2012-2013 Harry Merriwether Fellowship, which is the top award for Ph.D. students at Auburn University.

5. **Gregory C. Vaughan, M.S.**, "*Modeling and Optimization of Biomass Gasification*", Final defense is planned for 2013. Mr. Vaughan has accepted a position with KBR in Birmingham, AL.

6. **Subin Hada, Ph.D.,** "*Molecularly Informed Design of Structured Products*", expected 2013. Mr. Hada was selected as one of only 44 US and South American graduate students to receive an all-expenses paid trip to attend the 2011 PASI workshop in Angra dos Reis, Brazil. Mr. Hada is the recipient of the 2013 Auburn University President's Award for Outstanding Graduate Student, which recognizes one graduate student for outstanding scholarship, leadership, citizenship, character and professional ability. It is the highest honor bestowed by the Auburn University Graduate School.

**Publications**

19. Durham E., Xu R., Zhang S., Eden M.R., Roberts C.B. (2013): "Supercritical Adiabatic Reactor for Fischer-Tropsch Synthesis", *Industrial & Engineering Chemistry Research* (published online October 10, 2012, DOI: 10.1021/ie3008677).

20. Batsy D.R., Solvason C.C., Sammons N.E., Chambost V., Bilhartz D., Eden M.R., El-Halwagi M.M., Stuart P.R. (2012): "Product Portfolio Selection and Process Design of the Forest Biorefinery", invited chapter in *Integrated Biorefineries: Design, Analysis, and Optimization*, P.R. Stuart and M.M. El-Halwagi, Eds., CRC Press, ISBN 9781439803462 (published December 12, 2012).

21. Durham E., Zhang S., Xu R., Eden M.R., Roberts C.B. (2012): "Novel Adiabatic Reactor Design for Supercritical Fischer-Tropsch Synthesis", *Computer Aided Chemical Engineering*, 30B, pp. 1098-1102.

22. Hada S., Solvason C.C., Eden M.R. (2011): "Molecular Design of Biofuel Additives for Optimization of Fuel Characteristics", *Computer Aided Chemical Engineering*, 29B, pp. 1633-1637.

23. Odjo A.O., Sammons Jr. N.E., Yuan W., Marcilla A., Eden M.R., Caballero J.A. (2011): "A Disjunctive-Genetic Programming Approach to Synthesis of Process Networks", *Industrial & Engineering Chemistry Research*, 50(10), pp. 6213-6228.

24. Tay D.H.S., Ng D.K.S., Sammons Jr. N.E., Eden M.R. (2011): "Fuzzy Optimization Approach for Optimal Integrated Biorefinery Product Allocation", *Industrial & Engineering Chemistry Research*, 50(3), pp. 1652-1665.

25. Yuan W., Vaughan G.C., Roberts C.B., Eden M.R. (2011): "Modeling and Optimization of Supercritical Phase Fischer-Tropsch Synthesis", *Computer Aided Chemical Engineering*, 29B, pp. 1929-1933.

26. Bacik, D.B.; Yuan W.; Roberts, C.B.; Eden, M.R.; "Systems Analysis of Benign Hydrogen Peroxide Synthesis in Supercritical CO2", Computer Aided Chemical Engineering, 29A, 387-391, 2011.

27. Sammons Jr. N.E., Yuan W., Bommareddy S., Eden M.R., Aksoy B., Cullinan H.T. (2009): "A Systematic Framework to Calculate Economic Value and Environmental Impact of Biorefining Technology", *Computer Aided Chemical Engineering*, 27, pp. 2007-2012.

28. Yuan W., Odjo A.O., Sammons Jr. N.E., Caballero J., Eden M.R. (2009): "Process Structure Optimization using a Hybrid Disjunctive-Genetic Programming Approach", *Computer Aided Chemical Engineering*, 27, pp. 669-674.

29. Sammons Jr. N.E., Yuan W., Bommareddy S., Eden M.R., Aksoy B., Cullinan H.T. (2009): "Systematic Approach to Evaluate Economic and Environmental Impact of Biorefineries", *Computer Aided Chemical Engineering*, 26, pp. 1135-1140.

30. Yuan W., Odjo A., Sammons Jr. N.E., Caballero J., Eden M.R. (2009): "Process Optimization using a Hybrid Disjunctive-Genetic Programming Approach", *Design for Energy and the Environment*, pp. 767-776, Taylor and Francis.

31. Sammons Jr. N.E., Yuan W., Eden M.R., Aksoy B., Cullinan H.T. (2008): "Optimal Biorefinery Product Allocation by Combining Process and Economic Modeling", *Chemical Engineering Research and Design*, 86(7), pp. 800-808.

32. Sammons Jr. N.E., Yuan W., Eden M.R., Aksoy B., Cullinan H.T. (2008): "A Systematic Framework for Biorefinery Production Optimization", *Computer Aided Chemical Engineering* 25, pp. 1077-1082.

33. Yuan W., Sammons Jr. N.E., McGlocklin K.H., Eden M.R. (2008): "Economic Analysis and Process Integration of Hydrogen Production Strategies", *Computer Aided Chemical Engineering* 25, pp. 1083-1088.

34. Sammons Jr. N.E., Yuan W., Eden M.R., Cullinan H.T., Aksoy B. (2007): "A Flexible Framework for Optimal Biorefinery Product Allocation", *Journal of Environmental Progress* 26(4), pp. 349-354.

35. McGlocklin K.H., Sammons Jr. N.E., Yuan W., Wilder J.L., Eden M.R. (2007): "Systematic Framework for Economic Evaluation of Hydrogen Production Strategies", *Preprints Am. Chem. Soc., Div. Fuel Chem.* 52(2) pp. 465-466.

36. Durham E., Xu R., Zhang S., Eden M.R., Roberts C.B. (2013): "Supercritical Adiabatic Reactor for Fischer-Tropsch Synthesis", *Industrial & Engineering Chemistry Research* (published online October 10, 2012, DOI: 10.1021/ie3008677).

37. Batsy D.R., Solvason C.C., Sammons N.E., Chambost V., Bilhartz D., Eden M.R., El-Halwagi M.M., Stuart P.R. (2012): "Product Portfolio Selection and Process Design of the Forest Biorefinery", invited chapter in *Integrated Biorefineries: Design, Analysis, and Optimization*, P.R. Stuart and M.M. El-Halwagi, Eds., CRC Press, ISBN 9781439803462 (published December 12, 2012).

38. Durham E., Zhang S., Xu R., Eden M.R., Roberts C.B. (2012): "Novel Adiabatic Reactor Design for Supercritical Fischer-Tropsch Synthesis", *Computer Aided Chemical Engineering*, 30B, pp. 1098-1102.

39. Hada S., Solvason C.C., Eden M.R. (2011): "Molecular Design of Biofuel Additives for Optimization of Fuel Characteristics", *Computer Aided Chemical Engineering*, 29B, pp. 1633-1637.

40. Odjo A.O., Sammons Jr. N.E., Yuan W., Marcilla A., Eden M.R., Caballero J.A. (2011): "A Disjunctive-Genetic Programming Approach to Synthesis of Process Networks", *Industrial & Engineering Chemistry Research*, 50(10), pp. 6213-6228.

41. Tay D.H.S., Ng D.K.S., Sammons Jr. N.E., Eden M.R. (2011): "Fuzzy Optimization Approach for Optimal Integrated Biorefinery Product Allocation", *Industrial & Engineering Chemistry Research*, 50(3), pp. 1652-1665.

42. Yuan W., Vaughan G.C., Roberts C.B., Eden M.R. (2011): "Modeling and Optimization of Supercritical Phase Fischer-Tropsch Synthesis", *Computer Aided Chemical Engineering*, 29B, pp. 1929-1933.

43. Bacik, D.B.; Yuan W.; Roberts, C.B.; Eden, M.R.; "Systems Analysis of Benign Hydrogen Peroxide Synthesis in Supercritical CO2", Computer Aided Chemical Engineering, 29A, 387-391, 2011.

44. Sammons Jr. N.E., Yuan W., Bommareddy S., Eden M.R., Aksoy B., Cullinan H.T. (2009): "A Systematic Framework to Calculate Economic Value and Environmental Impact of Biorefining Technology", *Computer Aided Chemical Engineering*, 27, pp. 2007-2012.

45. Yuan W., Odjo A.O., Sammons Jr. N.E., Caballero J., Eden M.R. (2009): "Process Structure Optimization using a Hybrid Disjunctive-Genetic Programming Approach", *Computer Aided Chemical Engineering*, 27, pp. 669-674.

46. Sammons Jr. N.E., Yuan W., Bommareddy S., Eden M.R., Aksoy B., Cullinan H.T. (2009): "Systematic Approach to Evaluate Economic and Environmental Impact of Biorefineries", *Computer Aided Chemical Engineering*, 26, pp. 1135-1140.

47. Yuan W., Odjo A., Sammons Jr. N.E., Caballero J., Eden M.R. (2009): "Process Optimization using a Hybrid Disjunctive-Genetic Programming Approach", *Design for Energy and the Environment*, pp. 767-776, Taylor and Francis.

48. Sammons Jr. N.E., Yuan W., Eden M.R., Aksoy B., Cullinan H.T. (2008): "Optimal Biorefinery Product Allocation by Combining Process and Economic Modeling", *Chemical Engineering Research and Design*, 86(7), pp. 800-808.

49. Sammons Jr. N.E., Yuan W., Eden M.R., Aksoy B., Cullinan H.T. (2008): "A Systematic Framework for Biorefinery Production Optimization", *Computer Aided Chemical Engineering* 25, pp. 1077-1082.

50. Yuan W., Sammons Jr. N.E., McGlocklin K.H., Eden M.R. (2008): "Economic Analysis and Process Integration of Hydrogen Production Strategies", *Computer Aided Chemical Engineering* 25, pp. 1083-1088.

51. Sammons Jr. N.E., Yuan W., Eden M.R., Cullinan H.T., Aksoy B. (2007): "A Flexible Framework for Optimal Biorefinery Product Allocation", *Journal of Environmental Progress* 26(4), pp. 349-354.

52. McGlocklin K.H., Sammons Jr. N.E., Yuan W., Wilder J.L., Eden M.R. (2007): "Systematic Framework for Economic Evaluation of Hydrogen Production Strategies", *Preprints Am. Chem. Soc., Div. Fuel Chem.* 52(2) pp. 465-466.

# E.L. Kugler and D.B. Dadyburjor
# Department of Chemical Engineering
# West Virginia University


Fischer-Tropsch (FT) synthesis using Fe-based catalysts supported on activated carbon with multiple promoters: Mo, Cu, and K

During this time period, research was carried out in a number of areas: molybdenum-carbide-based catalysis, partial oxidation catalysis, dry reforming, and Fischer-Tropsch (FT) processing. This work has led to advances in all these areas, including the preparation of nanosized Mo catalysts of fixed stoichiometries, techniques for determining pathways for fast oxidation reactions and the effect of different catalysts, novel bimetallic carbide catalysts that overcome the deactivation disadvantages of conventional Ni-based catalysts, and the effects of individual components in a multi-metal Fe-based FT catalyst, with and without added zeolite for product upgrading. These are briefly discussed below. Refereed publications are cited separately.

A. MOLYBDENUM CARBIDE STOICHIOMETRY, PREPARATION AND REACTIVITY

Nanometer-sized molybdenum carbide particles have been shown to have hydrogenation and other catalytic properties similar to those of the more-expensive noble metals. However, previous preparation techniques for molybdenum carbide required the high-temperature reduction of unsupported molybdenum oxide in the presence of $CH_4$ and $H_2$. Although this method is effective, it yields particles of relatively large size, 11 nm. We showed [1] that different, simpler, synthesis procedures starting with ammonium heptamolybdate (AHM) impregnated on carbon yield carbides of different stiochiometries, $Mo_2C$ and MoC. Particle sizes are in the 2-10 nm range, which are generally smaller than those previously obtained, and can be altered by changing the method of preparation.

Nanometer-size molybdenum carbide particles were prepared on a carbon support by heating AHM in inert or reducing environments. Reduction in hydrogen produces the smallest $Mo_2C$ particles, observed to be 1-3 nm. Hydrogen consumption begins below 500$^o$C but $MoO_2$ reduction is not observed by XRD until 700$^o$C. When methane is used as the reducing gas, reaction occurs at 700-725$^o$C. $MoO_2$ diffraction lines disappear as $Mo_2C$ forms, producing carbides with an average size of 8 nm. When the $MoO_2$ (on carbon) is heated in inert gas, the transition to $Mo_2C$ occurs about 800$^o$C, producing 9 nm carbides. In all cases, the carburization source is the carbon support. Furthermore, the reduction temperature and annealing time allow the size of hexagonal $Mo_2C$ to be tuned. In contrast, reduction in CO leads to the formation of cubic MoC particles, with an average size of 3 nm; see Figure 1. Finally, further reduction of the cubic MoC in $H_2$ changes the carbide structure back to hexagonal $Mo_2C$ (Figure 2), as was observed for reaction in $H_2$, $CH_4$ and inert gas.

Activity data were obtained over these catalysts for hydrogenation of benzene and (with K promotion) for synthesis of higher alcohols (HAS) from synthesis gas [2]. For benzene hydrogenation, of the three supported catalysts tried, the only active material is the $Mo_2C$/C obtained by reduction in $H_2$. Further, to be active, these catalysts have only a small range of reduction temperatures, 675-825°C, and they need to be "soaked" at the final reduction temperature. However, as soak time increases, the initial activity decreases. The loss of activity is correlated to the appearance of graphitic carbon in the spent catalyst, as detected by XRD.

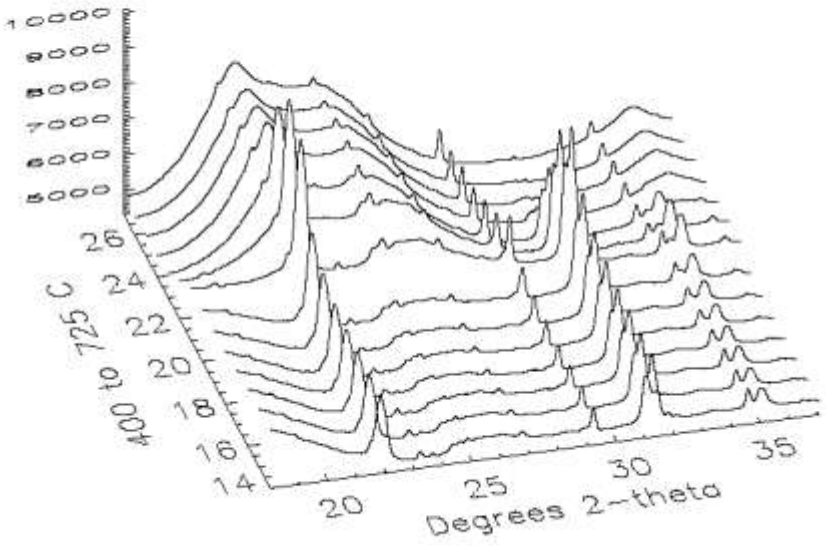


Figure 1. *In situ* x-ray diffraction results for $MoO_2$ on activated carbon heated in 5% CO at 5°C/min. Temperature range is 25 to 825°C. Scans on the Y-axis are separated by 25°C. [1]

For HAS, all three catalysts, MoC, $Mo_2C$ and $MoO_2$ (all K promoted), were active between 250-300°C. $MoO_2$ made the most alcohols initially, but $Mo_2C$ made the most alcohols overall and MoC the least. $Mo_2C$ was the most stable. Carbon nanotubes were seen on spent MoC, while carbon deposits were found on spent $Mo_2C$ and $MoO_2$.

Characterization was carried out with partial support from Brookhaven National Laboratory, the National Synchrotron Light Source (XRD) and the Center for Functional Nanomaterials (STM). NETL personnel helped with TPR-MS experiments.

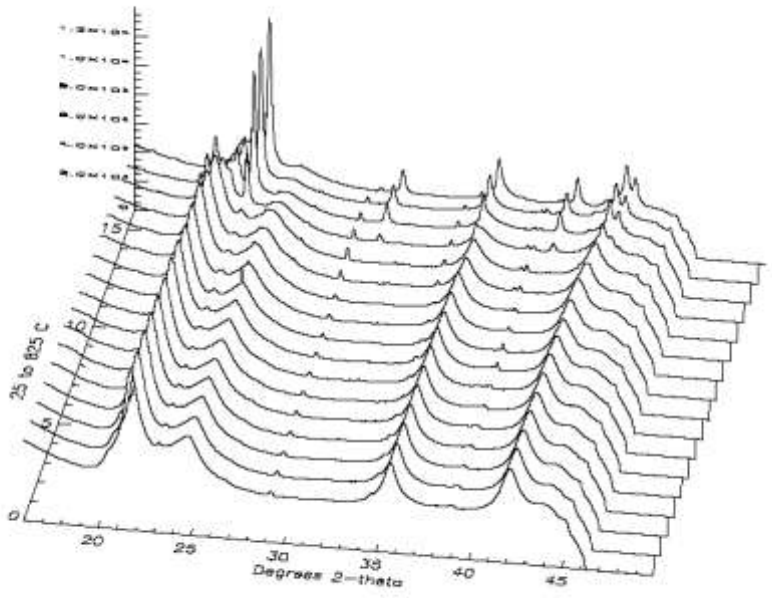


Figure 2. *In situ* x-ray diffraction results for reduction in 5% $H_2$ of MoC-on-carbon prepared as in Figure 7. The sample was heated from 25 to 825°C at 10°C/min. Scans on the Y-axis are separated by 50°C. [1]

B. PARTIAL OXIDATION OF PROPANE: EFFECT OF REACTION CONDITIONS, EFFECT OF CATALYST TYPE ON PATHWAYS OF THE REACTION

This work arose as an attempt to mimic the on-board reforming of gasoline to hydrogen by using propane as a model for gasoline. The initial catalyst used was $Pt/CeO_2$, to take advantage of the high activity of Pt and the ability of ceria to transition easily between two oxidation states. A variety of reactions can be assumed to occur:: partial oxidation (PO), total oxidation (TO), steam reforming (SR), autothermal reforming (ATR), as well as side reactions water-gas shift (WGS), dry reforming (DR), methanation (ME), dehydrogenation (DH), cracking (CR), water formation (WF) and carbon deposition (CD).

In the initial study [3], the formation of synthesis gas from propane oxidation was investigated on 1.0%$Pt/CeO_2$ catalysts in a fixed-bed flow reactor over a temperature range of 200°C to 800°C at atmospheric pressure using ~90% inert. Three kinds of ceria, with different surface areas, were used.. The catalysts were characterized using XRD, TPR, TPO, $H_2$ chemisorption and BET surface area. Pt catalyzes the reduction of the surface shell of the ceria support, and therefore shifts the low-temperature TPR peak of the support to lower temperature. Pt has little effect on the bulk reduction of ceria, so the high-temperature reduction peak is unchanged. Low-surface-area ceria shows negligible surface reduction, whereas the high-surface-area materials show considerable reduction of surface ceria.

The oxidation of propane occurs with two sets of products. At low temperatures ($T \leq 500$°C), propane oxidizes exclusively into $CO_2$ and $H_2O$ with little $H_2$. Above 500°C, $O_2$ is completely consumed and the selectivities of CO and $H_2$ increase steadily with increase in

temperature. In the region 500-700°C, high-surface-area catalysts show higher activity and selectivity to $H_2$ and CO than do low-surface-area catalysts. Propane conversion at high temperatures (T≥750°C) is similar for all the catalysts.
A large decrease in BET surface area is observed in Pt supported on higher-surface-are $CeO_2$(B and C) after high-temperature treatment. This may be the reason for the decrease in activity and selectivity with temperature. The lower-surface-area Pt/$CeO_2$(A) catalyst shows promising catalytic activity and selectivity during several hours of operation at 800°C. Propane conversion increases, and the selectivities of $H_2$ and CO decrease, with increase in $O_2/C_3H_8$ ratio.

In later work [4,5], analysis of the reaction data when varying flow rates and catalyst loadings (and hence contact times) led to a useful technique which can be used generally for determining the sequence of reactions of complex reaction sets. In this case, reactions were carried out at 600°C, and six species (CO, $H_2$, $CO_2$, $C_3H_8$, $C_3H_6$ and $O_2$) were analyzed at the exit of the reactor. Using the Gauss-elimination procedure, it was found that the number of independent reactions is 4. A material balance of the exit species can be used to determine a set of independent reactions which are physically meaningful under a given set of conditions. (Of course, dependent reactions are obtained by algebraic manipulations of the independent reactions chosen.) The set of reactions comprising PO, TO, WF and DH is a possible sequence of reactions for the low-surface-area catalyst, for both metal loadings. For the high-surface-area catalyst, the same set of reactions is also a possibility for the 0.01 g loading, but not for the 0.02 g loading. For that case, there is a net loss of water, so the water-formation reaction (WF) in the set above is replaced by the water-gas-shift (WGS) reaction. The net loss of water is shown to be due to the effect of the ceria support. To confirm the choice of the above sets, independent runs involving WGS, DR and SR were carried out over the catalysts. Neither DR nor SR can take place in appreciable amounts over any of the catalysts, while WGS occurs over the catalyst with the largest total surface area. This is consistent with the choice of reaction sets above.

Finally, the nature and relative importance of the reactions in these sets are obtained [5] by combining the parameters metal loading and flow rate as the weight-hourly space velocity (WHSV, in [scc/min/g]). Figure 3 shows the effect of WHSV on rates of loss of propane by the individual reactions TOX, POX, WF and DH per 100 sccm of inlet reactant flowrate. Figure 3 indicates that an increase in the contact time between reactants and catalyst, i.e., a decrease in WHSV, increases TOX rates while POX rates are comparatively higher at lower contact times. This indicates that the Pt/$CeO_2$ catalyst is most effective for hydrogen production at low contact times, while the catalyst is most effective for TOX at higher contact times. Accordingly, the POX reaction occurs before the TOX reaction. Hence for the Pt/$CeO_2$ catalyst, oxidation of propane occurs through the exothermic POX route.

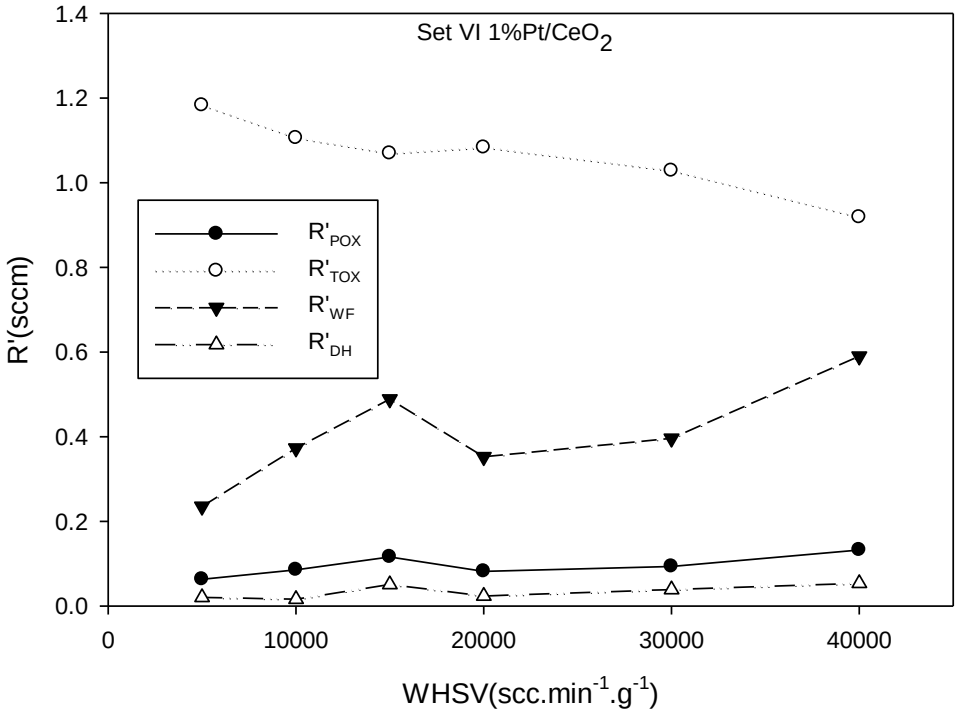


Figure 3. Effect of WHSV on 1%$Pt/CeO_2$ catalyst on reaction rates of TOX, POX, WF and DH per 100 sccm of inlet flow rate [5].

Figure 4 shows the corresponding data for 1% $Ni/CeO_2$ . The predominant reactions are TOX and SR, rather than POX and TOX for the Pt-based catalyst of Figure 3. Also, while the Pt-based catalysts the most active at the lower contact times (higher WHSV values), the Ni-based catalyst is the most active at the higher contact times (lower WHSV values). For the Ni-based catalyst, SR, rather than POX, is responsible for the production of $H_2$. Figure 4 suggests that, over the $Ni/CeO_2$ catalyst, the TOX reaction occurs first, and SR, which forms $H_2$, occurs at larger contact times. This is in contrast to the behavior over the $Pt/CeO_2$ catalyst.

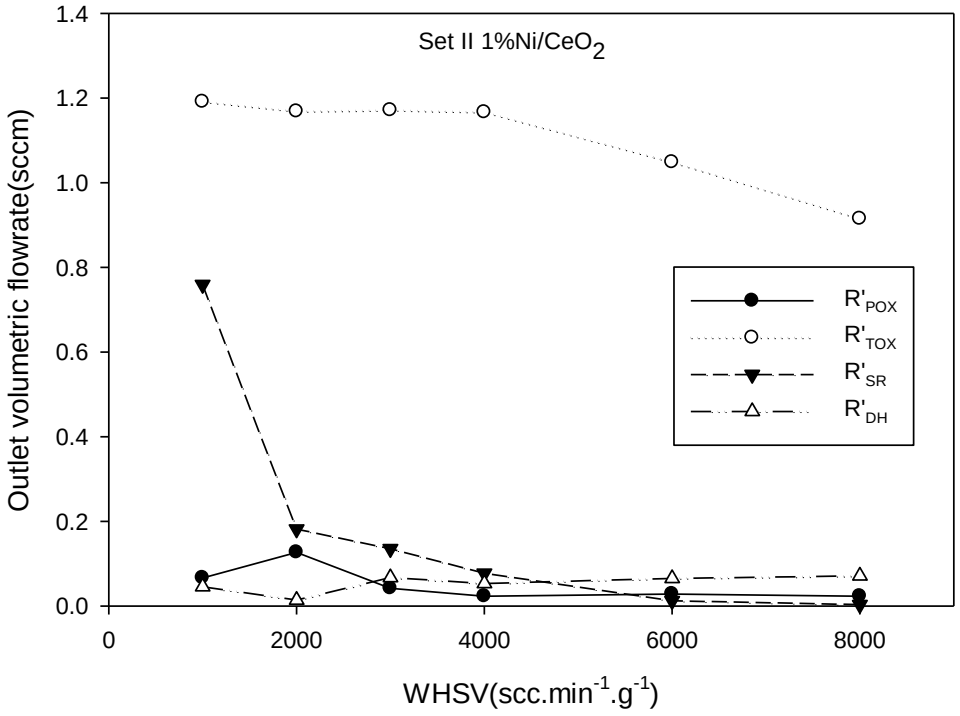


Figure 4. Effect of WHSV on 1%Ni/$CeO_2$ catalyst on reaction rates of TOX, POX, SR and DH per 100 sccm of inlet flow rate [5].

C. NOVEL BIMETALLIC CARBIDE CATALYSTS FOR DRY REFORMING OF METHANE

Conventional supported-nickel catalysts used in steam reforming have been modified in attempts to make them more resistant to coking for use in DR. Alkali or alkaline-earth metal promoters presumably function by making the catalyst support more basic, increasing the strength and coverage of adsorbed $CO_2$, thereby decreasing the probability of carbon deposit. Due to the similarities between noble metals and transition metal compounds, carbides and nitrides of transition metals have been used as catalysts. Our initial expectation with bimetallic carbides was that the second metal would counter the disadvantages of the monometallic carbide as a DR catalyst. We found rather that (at least some) eta-carbides can be used to form active species which serve as stable, low-pressure catalysts for DR. In initial experiments [6] with flowing $CH_4$ and $CO_2$ at relatively low pressures (3-5 atm), $Co_6W_6C$ was an unremarkable catalyst. After prolonged contact with the feed mixture at high temperatures, conversions were found to reach 90% and stayed at that level for over 160 hours. XRD indicates that, after an induction period, the bulk species is no longer $Co_6W_6C$ but a mixture of Co, C and WC. This is consistent with the Co-W-C phase diagram when excess C is added to $Co_6W_6C$. It is reasonable to expect that the carbon has come from the reactant $CH_4$. Hence, not only is the active species stable to coking, but the active species requires carbon (coke) to be formed (during the induction period). Careful rate measurements indicate that this catalyst has specific activities, i.e., activities per $m^2$ metal, from 20% greater to an order of magnitude greater than those of supported Ni and unsupported $Mo_2C$. (These comparisons are for initial values only; the comparisons do not take into account the greater deactivation expected for the monometallic carbide and the supported Ni catalysts while the bimetallic-carbide-based catalyst remains stable.)

In later work (7), we studied the effects of preparation conditions and reaction temperature history on the catalyst activity, selectivity and stability. The important parameter for preparation is the ratio of $CO_2$ to CO (termed x) in the carburization stage. For example, while x = 0.75 yields a material with XRD peaks corresponding only to $Co_6W_6C$, using a carburizing gas with x = 0.1 leads to a material with XRD peaks corresponding to Co, WC, C and $Co_3W_3C$. Preliminary data (8) indicate that both materials result in DR after an induction time, but the induction time is much shorter for the material with x = 0.1, i.e., when Co and WC peaks are initially present after carburization.

Extensive reactivity studies have been carried out on the material corresponding to x = 0.75, and some characterization work has been performed, both before and after reaction. The material was exposed to reactants $CH_4$ and $CO_2$ at a series of increasing and decreasing temperatures. The material was maintained at each temperature until steady state was reached, reactivities were measured, and then the material was quickly cooled or heated to the next temperature. Figure 5 shows the results. Here the points denote the values of conversion, yield and carbon balance at the temperatures on the x-axis, while the columns reflect the magnitude of the respective temperatures. At the first (leftmost) 700°C stage, conversions are low and the $H_2$/CO ratio is low. The carbon balance is high, reflecting the fact that most of the carbon entering the reactor (as $CO_2$ and $CH_4$) leaves the reactor (as CO); in other words, there is very little carbon deposition on the material. At the next stage, 600°C, catalyst performance is weaker, reflecting the Arrhenius relationship. When the material reaches steady state at 850°C, however, conversion and $H_2$/CO ratio rise dramatically, and the carbon balance drops. The deposition of carbon leads to an active phase of the catalyst. The following stage is the second time that the material has been exposed to 700°C. Now the values of the activity and $H_2$/CO ratio are much higher than those in the first 700°C stage. At the last two values, 600°C and 500°C, the reaction parameters are greater than they were at the first 600°C stage. This is observed even though the carbon balance is relatively high, i.e., little incremental carbon is being deposited. Clearly the nature of the carbide has changed after exposure to 850°C, which can be considered to be a trigger temperature.

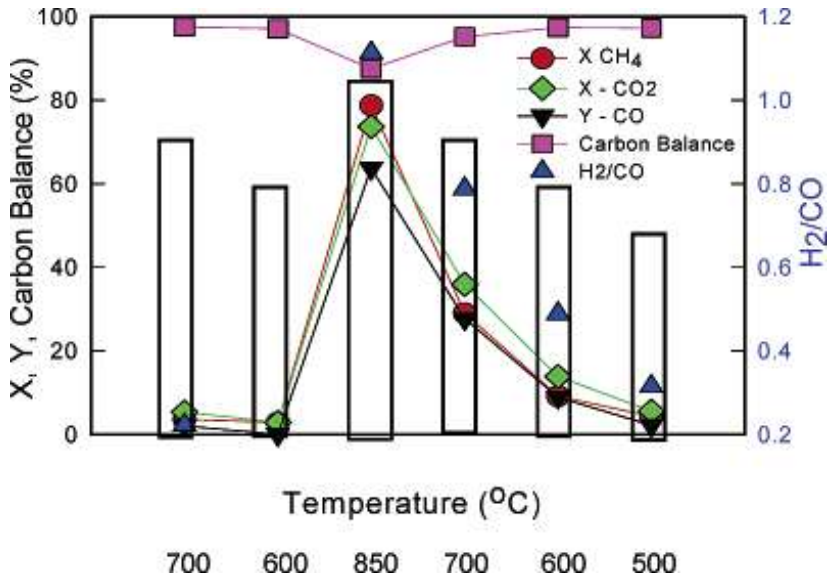

Figure 5. Summary of steady-state catalytic performance during temperature progression for $Co_6W_6C$ with x (= $CO_2$/CO) = 0.75.

Characterization data (7, 8) on this and similar starting materials shed some light on this. TPR peaks indicate the presence of some oxide, at least on the surface of the fresh material. XRD indicates that the spent catalyst after the first 700°C stage, i.e., the ineffectual catalyst, contains bulk phases of the original $Co_6W_6C$ as well as $CoWO_4$ and WC. After exposure to 850°C and after the second 700°C (when the material has been exposed to 850°C earlier), the tungstate is not seen; the XRD patterns contain only Co, WC and C, and in some cases, various stoichiometries of Co-W-C. SEM and EDX results indicate that C is present after 850°C and with the second 700°C stage, whereas O is seen in the first 700C stage. NEXAFS results [9] indicate that Co, carbide carbon and significant oxides are present in the fresh material. After the first 700°C stage, graphitic carbon begins to replace carbide carbon, and the oxide features decrease. After exposure to 850°C, only graphitic carbon is seen, although some oxygen features can still be seen.

A possible sequence of events is as follows. Some oxygen is left on the surface of the freshly-prepared eta-carbide, probably from the starting material. When the reaction temperature is less than 850°C, the surface oxygen (Os) is converted to $CoWO_4$, perhaps by a formal reaction of the type:

$$Co_6W_6C + (26\text{-}y)\ Os \rightarrow 6\ CoWO_4 + y\ CO + (1\text{-}y)\ CO_2 \qquad (1)$$

$CoWO_4$ in the solid makes for an ineffective catalyst. At temperatures equal to or higher than 850°C, the oxide can be removed, perhaps by reactant methane, leaving the active species Co, WC and C, perhaps by a formal reaction of the type:

$$CoWO_4 + 2\ CH_4 \rightarrow Co + WC + C + 4\ H_2O \qquad (2)$$

However, we expect that most of the Co and WC are formed by interaction of the eta-carbide as shown below:

$$Co_6W_6C + 5\ C \rightarrow 6\ Co + 6\ WC \qquad (3)$$

using carbon from deposited coke and/or from the reaction of Eqn (2). Unpublished experiments (8) show that WC prepared separately and mixed with elemental Co does not constitute a viable catalyst for DR.

The procedure for preparing $Co_6W_6C$ was modified [8] to prepare other eta-carbides. XRD measurements on Ni-based materials are different from XRD on Co-based materials, even when prepared in the same way. When x = 0.75, XRD measurements indicate that the resultant material contains not only $Ni_6W_6C$, but also WC and a small amount of Ni-W alloy. The difference between this material and that prepared using Co with the same value of x (pure $Co_6W_6C$) can be ascribed to the different interactions between the solid material and the carbon laid down. TPR measurements on the Ni-based materials indicate that some oxides are present, even if XRD does not indicate their presence in the bulk; this is consistent with the Co-based material.

Reactivity results for the Ni-based material can be seen in Figure 6 [8], in the form of a temperature-ramp study as in Figure 5. However, Figure 6 shows a symmetric pattern around the peak temperature, i.e., the performance of the catalyst at 700°C prior to exposure to 850°C is not markedly different from that at 700°C after exposure to 850°C. Catalytic performance at 700°C

either before or after exposure to 850°C is comparable to the performance of the $Co_6W_6C$ after exposure to 850°C. XRD patterns for the Ni-based materials after reaction show the presence of Ni, WC and $Ni_6W_6C$, whether or not the material has been exposed to 850°C. NEXAFS results indicate that the Ni-based material has much more graphitic carbon than does the Co-based material, and the oxide features are decreased more.

Clearly the solid-state transformation takes place at lower temperatures for the Ni-based material than it does for the Co-based material. Also, clearly, by the choice of the Ni-based catalyst, we have removed the need to operate or activate the catalyst at high temperatures. Hence we have a potential DR catalyst that can operate at relatively low pressures and low temperatu

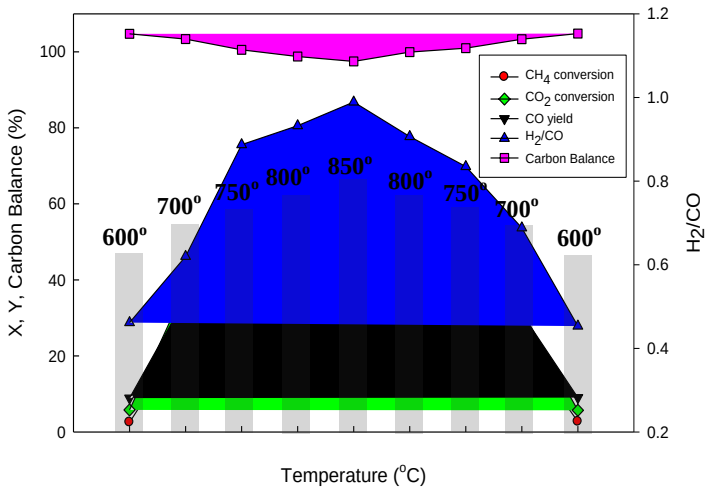


Figure 6. Summary of steady-state catalytic performance as in Figure 5, but for Ni-W-C (x = 0.75).

Finally, the catalysts are not suitable for steam reforming (SR) of methane or alcohols. This is consistent with our working hypothesis above. The presence of carbon is essential to the formation of WC and Ni or Co. The presence of large amounts of steam in SR clearly prevents carbon deposition, and consequently does not allow the eta-carbides to form suitable catalysts.

NEXAFS measurements were performed by S.A. Rykov and J.G.Chen, then at the University of Delaware, with financial support from the U.S. Department of Energy, Office of Sciences, Division of Chemical Sciences.

## D. FISCHER-TROPSCH CATALYSIS: EFFECT OF ADDITIVES ON IRON / ACTIVATED-CARBON-BASED CATALYSTS

Iron-based catalysts are advantageous for Fischer-Tropsch (FT) reactions because of their cost (relative to Co) and because their activity for water-gas shift (WGS) makes them suitable for syngas with low $H_2/CO$ ratios. Work in our laboratory has concentrated on these catalysts on activated-carbon (AC) supports with multiple promoters, Mo, Cu, and K. First, in a series of experiments, we investigated the effects of each of these promoters on activity, selectivity and stability. More recently, we investigated the effects on product selectivity (upgrading) when zeolites are combined with these FT catalysts.

The effects of physical and surface chemistry properties of four ACs on the distribution and reduction of metal precursors of FT catalysts were noted [10]. The four ACs used were derived from peat (PT), generic wood (WD), pecan (PN) and walnut (WT). Characterization techniques used included BET, SEM and EDS, surface pH, TPD-MS, TEM and TPR. The four ACs showed considerable differences in surface area, pore structure and surface chemistry. Results from BET and TEM indicated that the pore structure of the support ACs primarily affects the distribution of metal crystallites and the particle size on the AC surface. Larger numbers of wide pores for PN-AC, WT-AC, and PT-AC lead to a better overall distribution of metal on the AC surface and smaller metal crystallites. During the impregnation, micro-pores likely do not distribute metal on ACs as effectively as the wide pores do, due to mass transfer limitation. More micro-pores on the WD-AC support induce more aggregation of metals, and more large crystallites on the external surface.

EDS indicated that all four ACs contain 5.6-7.5% oxygen; the wood- and peat-based varieties include smaller amounts of other impurities in addition. The results of pH and TPD indicated that the surface of all four ACs are primarily covered by neutral and/or basic oxygen-containing groups, along with small amounts of acidic oxygen groups. TPD, TEM and BET demonstrated that the metals are uniformly dispersed on all ACs. TEM showed different metal dispersions on the four AC-supported catalysts resulting from their different surface and pore structure. The TPD study revealed that the species (primarily CO) emitted from the support ACs are due to neutral or basic groups on the support. The increase of species emitted from the catalyst after 500°C primarily stems from the reaction of active carbon with partially oxidized metals.

All four catalysts (4 different ACs, each impregnated with 15.7% Fe, 6% Mo, 0.8% Cu, and 0.9% K) were used in FT reactions. Estimated values of the turnover frequency and activation energy are consistent with values reported in the literature for similar catalysts. The activity of the catalysts was linear with respect to the parameter δ as shown in Figure 7. This parameter is the product of the metal particle size, the fractional decrease of the surface area attributed to wide pores after impregnation of the metals, and the fraction of total surface area associated with the wide pores after impregnation. The rationale is as follows: the metal particle size reflects metal dispersion; the fractional decrease of the surface area attributed to wide pores after impregnation can be related to metal crystallites present in the wide pores; and the fraction of total surface area associated with the wide pores after impregnation can be related to the ease of mass transfer.

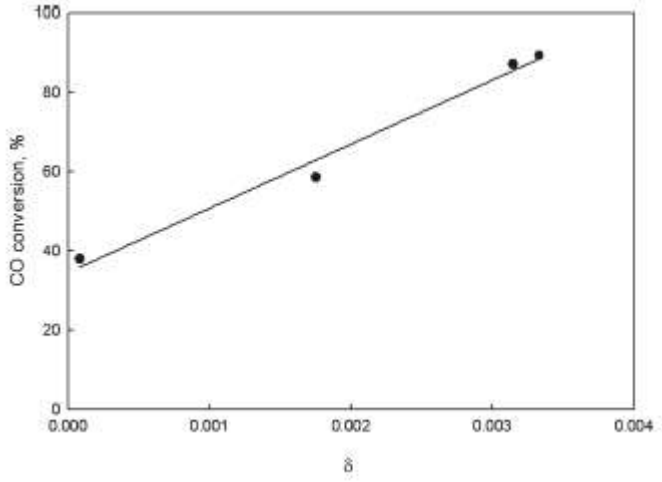

Figure 7. Conversion of CO vs. parameter δ defined in text. The points correspond to the four types of AC used [10].

Some selectivity data using each of the four ACs as supports are shown in Table 1 [10]. The selectivity towards $C_{5+}$ products is related to the amount of species evolved during the TPR of the AC support, i.e., the number of basic and neutral species on the surface. High selectivity towards $C_1$ correlates well to low pH of the external surface of the support.

Table 1. Fischer-Tropsch reaction results over AC-supported catalysts [10] [(a)]

| AC Support [(b)] | T = 320°C | | | | | T = 310°C | |
|---|---|---|---|---|---|---|---|
| | Time on stream [h] | CO Conversion $X_{CO}$ [%] | Hydrocarbon Selectivity [wt%] | | | Time on stream [h] | CO Conversion $X_{CO}$ [%] |
| | | | $C_1$ | $C_2$-$C_4$ | $C_{5+}$ | | |
| PT | 49-73 | 87.1 | 10.9 | 40.9 | 48.2 | 173-175 | 81.7 |
| WD | 49-72 | 37.9 | 13.9 | 54.8 | 31.3 | - | - |
| PN | 47-70 | 90.1 | 15.3 | 32.4 | 52.3 | 173-175 | 71.6 |
| WT | 47-70 | 58.5 | 14.9 | 34.6 | 50.5 | - | - |

(a) Reaction conditions: 3 Nl/g-cat/h, 300 psig, $H_2$/CO=0.9.
(b) Catalysts are AC impregnated with 6% Mo, 15.7% Fe, 0.8% Cu and 0.9% K.
(c) Mean values over time range shown.

The peat-based AC was used for subsequent work. The effects of Mo loading (0-12 wt %) on the properties of activated-carbon- (AC-) supported Fe-Cu-K catalysts and their performance for Fischer-Tropsch synthesis can be described next [11] . As above, physicochemical properties studied included particle size, reducibility, and dispersion, and catalytic properties include activity, selectivity, and stability. Catalysts were characterized by $N_2$ adsorption, EDS, XRD, $H_2$ TPR, and CO chemisorption. Catalyst performance was studied at 310-320 °C, 2.2 MPa, 3 Nl/g-cat/h, and $H_2$/CO = 0.9.

A small amount of Mo does not change the pore characteristics appreciably, but larger amounts decrease the surface area and increase the pore diameter, perhaps because some of the pores are blocked by Mo. The Mo is highly dispersed on the support, and the addition of Mo improves Fe dispersion after the catalysts are reduced at 400 °C for 12 h. The addition of Mo prevents iron particles from agglomerating at reduction and reaction conditions. The TPR studies indicate a three-step reduction process of iron oxide on AC

$$Fe_2O_3 \rightarrow Fe_3O_4 \rightarrow FeO \rightarrow Fe \qquad (4)$$

in three distinctive temperature ranges, 200-300, 300-400, and 400-800 °C. The reducibility of Fe-Cu-K/AC catalysts is affected greatly by the Mo promoter. There is a strong interaction between Fe and Mo oxides. As a result, the extents of reduction of Mo-containing Fe-Cu-K/AC catalysts decrease. Quantitative TPR analysis confirms the results and shows the greater influence of the first- and second-stage reductions of iron oxide.

For the spent catalysts, the surface areas and pore volumes are decreased, but the average pore diameters increase, perhaps because of pore collapse or blockage of the pores by intermediates. On the spent catalysts, iron carbide ($Fe_2C_5$) and magnetite ($Fe_3O_4$) are detected by XRD. These are postulated to be active phases for the FTS and WGS reactions. At the higher Mo

loading, two additional peaks appear. Both the 6% and 12% Mo catalysts show much greater stability than the catalyst without Mo, perhaps because of the prevention of Fe agglomeration due to the presence of Mo, as noted above.

Figure 8 summarizes the reaction data for these catalysts. Over the 6% Mo catalyst, the activity is higher than that over the 12% Mo catalyst. This might be due to the higher degree of reduction of iron oxide on the 6% Mo catalyst, which allows more reduced Fe to be carbonized to active sites for the FTS reaction. The extent of WGS is high over all three catalysts but decreases with time on stream.

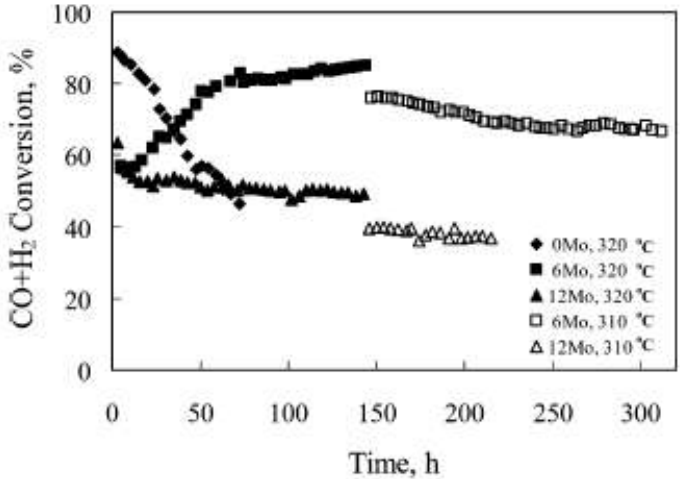


Figure 8. Syngas conversion over different Mo-loaded Fe-Cu-K/AC

Table 2. HC Productivity and HC Selectivity, and Olefin/Paraffin Ratios over Different Mo Loadings of Fe-Cu-K/AC FT Catalysts [a,b] [11].

| % Mo | 0 | 6 | 6 | 12 | 12 |
|---|---|---|---|---|---|
| temperature, °C | 320 | 320 | 310 | 320 | 310 |
| TOS, h | 25–72 | 73–144 | 200–315 | 72–143 | 168–215 |
| productivity, g-HC/g-cat/h | 426–330 | 495–480 | 420–380 | 310–290 | 240–220 |
| | | Hydrocarbon Selectivity, wt % | | | |
| $CH_4$ | 7.2 | 15 | 14.3 | 14.1 | 13.1 |
| $C_2$–$C_4$ | 39.6 | 45.6 | 42.4 | 40.6 | 37.4 |
| $C_{5+}$ | 51.6 | 39.4 | 43.3 | 45.3 | 49.6 |
| | | Olefin/Paraffin Ratio | | | |
| $C_2$–$C_4$ | 6.0 | 2.2 | 2.2 | 2.0 | 2.2 |
| $C_5$–$C_{11}$ | 1.4 | 0.9 | 1.2 | 1.4 | 1.5 |

[a] Process conditions: 3 Nl/g-cat/h, 300 psig, $H_2/CO = 0.9$. All catalysts contain 15.7 wt % Fe, 0.8 wt % Cu, and 0.9 wt % K. [b] Ranges are low TOS value to high TOS value. Single values are averaged over the TOS range.

more methane and less $C_{5+}$ hydrocarbons. This is probably due to Mo oxide in the catalyst weakening the C-O bond, resulting in a higher concentration of active C species on the surface of the Mo-promoted catalyst. The Mo addition decreases total olefin selectivity and increases

internal-olefin selectivity in the products. The role of $MoO_3$ in the Fe-Cu-K/AC catalysts is probably similar to that of an acid catalyst.

The effect of varying potassium (0-2wt%) was also studied [12]. As before, a fixed-bed reactor was used under the conditions of 260 - 300°C, 300 psig, and 3 Nl/g-cat/h, using syngas with a $H_2$/CO molar feed ratio of 0.9. From Table 3, the change of catalytic activity by potassium depends greatly on the K content of the catalyst. The addition of 0.9 wt% potassium into the Fe/AC catalyst increases the activity of the catalyst for both FTS and WGS, more so than the addition of 2 wt% K. The ratio of WGS to FTS reactions, $R_{WF}$, is also greatest for the 0.9 wt% K catalyst. Increasing K levels increase the deactivation rate.

From Table 4, for the selectivity of $C_{5+}$ (liquid phase) hydrocarbons, the 0.9 wt% K catalyst is far superior to the unpromoted catalyst, and a small improvement is obtained for the 2wt% K catalyst. The effect of K addition on $C_{1-4}$ (vapor phase) selectivity is opposite. This behavior can be attributed to the formation of more carbide phases by potassium. For the K-containing catalyst, as the temperature increases, the $C_{5+}$ selectivity decreases. The olefin/paraffin ratios are much greater for the 0.9 wt% K catalyst than for the unpromoted catalyst, with again a slightly higher value for the 2wt% K catalyst. This holds for hydrocarbons in the $C_2$-$C_4$ range and in the $C_5$-$C_{11}$ range. Finally, the ratios of internal-olefin/1-olefin are much larger for the unpromoted catalyst and least for the 2wt% K catalyst. This indicates that the promoter is less active for secondary reactions. At least for carbon numbers of 25 or less, increasing the K level to 0.9 wt% greatly decreases the amount of n-paraffins and *int*-olefins and dramatically increases branched paraffins and 1-olefins. These effects of K are smaller for the further increase of the K level to 2 wt%.

The effect of the final component, Cu, was studied over peat-based activated-carbon (AC) supported 15.7 wt% Fe and 0.9 wt% K catalysts [13]. The range of Cu used was 0-2%. As before, reactivity, selectivity and stability experiments were carried out in a fixed-bed reactor at 300 psig, 3 Nl/g-cat/h, and a syngas with a $H_2$/CO molar feed ratio of 0.9 in a temperature range 260 - 290 $^oC$.

Copper significantly promotes the reduction of the catalysts via decreased reduction temperatures and increased reduction rates. The lower Cu loading may lead to the formation of some Fe-Cu clusters, and/or the Cu promoter could suppress carbonization of Fe, and/or foster carbon deposition during the carbonization at the beginning of the process. This results in a decreased change in the activity of the FeK/AC catalyst, for both FTS and WGS activities; see Table 5. For FTS, Cu decreases both the activation energy and pre-exponential factor, but it predominately affects the latter parameter. For WGS, Cu affects the activation energy and pre-exponential factor similarly.

Addition of Cu changes the selectivities to hydrocarbons (olefin/paraffin, 1-olefins/2-olefins). These have been explained in terms of the altering of the surface chemistry of the catalysts. Addition of Cu does not significantly change the overall hydrocarbon distribution of the FeK/AC catalyst, but a change in the amounts of the longer-chain products may be noted.

Table 5**.** Activities and hydrocarbon selectivities over FeK/AC with and without Cu

| Catalyst | 15.7Fe/0.94K/AC (0Cu) | | | 15.7Fe/0.8Cu/0.94K/AC (1Cu) | | | | 15.7Fe/2Cu/0.94K/AC (2Cu) | | | |
|---|---|---|---|---|---|---|---|---|---|---|---|
| Temperature, $^{o}$C | 260 | 270 | 280 | 260 | 270 | 280 | 290 | 260 | 270 | 280 | 290 |
| TOS, h | 5-22 | 22-46 | 46-70 | 4-19 | 19-43 | 43-67 | 67-91 | 5--22 | 22-46 | 46-70 | 70-94 |
| Conversion, % | | | | | | | | | | | |
| $X_{CO}$ | 50.7 | 59.9 | 85.7 | 30.7 | 38.6 | 45.3 | 55.5 | 28.1 | 38.6 | 52.5 | 65.3 |
| $X_{H2}$ | 40.0 | 44.9 | 63.0 | 28.8 | 33.6 | 38.2 | 45.1 | 23.8 | 30.6 | 39.0 | 46.0 |
| $X_{CO+H2}$ | 45.5 | 52.7 | 74.8 | 29.8 | 36.2 | 41.9 | 50.5 | 26.0 | 34.8 | 46.0 | 56.0 |
| HC selectivity, wt% | | | | | | | | | | | |
| $CH_4$ | 7.8 | 6.6 | 8.6 | 8.9 | 7.5 | 8.8 | 9.4 | 8.1 | 7.0 | 7.9 | 8.9 |
| $C_2$-$C_4$ | 41.7 | 34.4 | 34.9 | 37.3 | 31.9 | 35.6 | 36.3 | 37.9 | 32.5 | 35.2 | 36.0 |
| $C_5^+$ | 50.5 | 59.0 | 56.5 | 53.8 | 60.6 | 55.6 | 54.3 | 54.0 | 60.5 | 56.9 | 55.1 |
| $r_{FT}$, mmol/h | 19.40 | 22.33 | 31.62 | 12.51 | 15.94 | 21.83 | 23.74 | 10.90 | 15.00 | 19.85 | 24.31 |
| $r_{WGS}$, mmol/h | 16.20 | 19.77 | 28.60 | 8.67 | 12.08 | 16.28 | 21.48 | 8.81 | 12.15 | 17.01 | 21.53 |
| $H_2$/CO usage ratio | 0.73 | 0.70 | 0.68 | 0.84 | 0.78 | 0.76 | 0.73 | 0.76 | 0.71 | 0.67 | 0.63 |
| $CO_2$ Selectivity, % | 45.5 | 47.0 | 47.5 | 41.9 | 43.1 | 45.2 | 45.7 | 44.6 | 44.9 | 46.1 | 47.0 |
| $J_p$ [(b)] | 22.2 | 27.9 | 39.8 | 9.9 | 7.2 | 10.5 | 16.6 | 10.6 | 7.5 | 12.6 | 21.1 |
| Total mass balance, % | | 101-98 | | | 96-99 | | | | 101-98 | | |

(a) AC is peat-derived. Metal compositions in wt%. Other process conditions: 3 Nl/g-cat/h, 300 psig, $H_2$/CO=0.9

$J_p = (P_{CO2}P_{H2})/(P_{CO}P_{H2O})$

Table 6. Olefin-to-paraffin ratios and internal-olefin percentages over FeK/AC catalysts with and without Cu [(a)] [13].

| Catalyst [(b)] | 0Cu | 1Cu | 2Cu | 0Cu | 1Cu | 2Cu |
|---|---|---|---|---|---|---|
| Temperature, °C | | 260 | | | 270 | |
| TOS, h | 21.0 | 3.0 | 3.0 | 85.0 | 25.0 | 30.0 |
| $X_{CO+H2}$, % | 40.9 | 34.4 | 32.0 | 41.5 | 41.1 | 38.5 |
| Olefin/paraffin ratio [(c)] | | | | | | |
| $C_2$ | 3.2 | 2.1 | 1.8 | 3.9 | 2.3 | 3.2 |
| $C_4$ | 5.1 | 3.4 | 3.2 | 6.4 | 3.7 | 5.2 |

| | | | | | | |
|---|---|---|---|---|---|---|
| $C_5$ | 2.4 | 2.3 | 1.7 | 3.6 | 2.3 | 2.2 |
| Internal olefin content [c,d] | | | | | | |
| $C_4$ | 8.6 | 10.5 | 14.3 | 6.0 | 7.9 | 6.2 |
| $C_5$ | 11.2 | 14.3 | 28.1 | 7.9 | 9.5 | 9.4 |

(a) Other reaction conditions: 300 psig, $H_2/CO = 0.9$, and 3 Nl/g-cat/h
(b) Support is a peat-derived carbon and all catalysts contain 15.7 wt% Fe and 0.9 wt% K
(c) From gas phase
(d) Internal olefin content, % = 100* internal olefins/(internal olefin +1-olefins)

From Table 6, an increase in the internal-olefin content and a reduction in the olefin content are observed under similar levels of CO conversion. This confirms that Cu promotes hydrogen adsorption and enhances hydrogenation and isomerization reactions of iron-based catalysts.

In the most recent work, in-reactor upgrading of the products of Fischer-Tropsch (FT) reactions using synthesis gas was studied by adding zeolite ZSM-5 to the FT catalyst consisting of 15.7% Fe, 6% Mo, 0.8% Cu, and 0.9% K impregnated on peat-based AC [14,15]. The influence of ZSM-5 amounts, bed arrangements, and the temperature on the product distribution were investigated. The stability of the combination was investigated up to 240 h time on stream. Two catalyst bed configurations were used. In the separate-bed configuration, the feed syngas was passed over the FT catalyst first, and the exit stream passed over the zeolite bed. In the mixed-bed configuration, the zeolite and the FT catalyst were well mixed.

WGS and FTS rates are constant for increasing ZSM-5 in the separate-bed arrangement, probably because ZSM-5 is inactive towards CO consumption. The separate bed shows high activity towards FTS, and results in high conversions and large amounts of high-octane gasoline-range hydrocarbons. In the mixed bed, FTS and WGS rates decrease with the addition of a small amount of ZSM-5, then increase with a further increase in ZSM-5, but these values are lower than those of the base catalyst. The lower activity towards FTS and WGS compared to the separate bed may be due to lowering of the alkali content of the iron catalyst because of alkali migration to ZSM-5 in the mixed bed. EDX analysis of the spent ZSM-5 after 72 h shows metal migration from the base catalyst to ZSM-5 in the mixed bed, but not in the separate bed. Both the separate bed and the mixed bed show conversion of alcohols to hydrocarbons and water, but the extent of conversion of alcohols is higher in the separate bed compared to the mixed bed. This is possibly because all alcohols pass over all the ZSM-5 in the separate bed, and so more amounts are reacted.

For the separate bed, the amounts of vapor-phase n- and i-paraffins increase with an increase in ZSM-5, probably because of enhanced cracking reactions. The amounts of olefins in the gas generally decrease with an increase in ZSM-5, probably because of an increase in the oligomerization reactions on ZSM-5. Liquid hydrocarbon production rates increase for small amounts of ZSM-5 because it converts alcohols formed by the base catalyst to hydrocarbons. Larger amounts of ZSM-5 provide additional cracking sites to give larger amounts of gas species. The production of alcohols decreases to nearly zero in the presence of even small amounts of ZSM-5. Heavier-chain hydrocarbon molecules ($C_{13+}$) formed by the base catalyst are effectively cracked and isomerized on the ZSM-5 catalyst surface. The base catalyst shows no selectivity towards aromatic compounds, but addition of ZSM-5 forms alkyl-benzene aromatic

compounds ($C_{7-10}$). The highest yields are for p-xylene, probably because of low steric hindrance compared to other aromatic compounds.

For the mixed bed, the amounts of vapor-phase n- and i-paraffins increase with an increase in ZSM-5, probably because of enhanced cracking reactions. The amounts of olefins in the gas generally decrease with a small amount of ZSM-5, probably because of an increase in the oligomerization reactions on ZSM-5. Further addition of ZSM-5 does not contribute much towards oligomerization reactions. Liquid hydrocarbon production rates decrease with an increase in ZSM-5, possibly due to metal migration from the FT catalyst to ZSM-5. As in the separate bed, ZSM-5 converts alcohols formed by the base catalyst to hydrocarbons, and larger amounts of ZSM-5 provide additional cracking sites to give larger amounts of gas species. However, for the mixed bed, even the largest amount of ZSM-5 used in this work is not sufficient to convert all the alcohols produced by the base catalyst. Heavier hydrocarbons ($C_{13+}$) formed by the base catalyst are effectively cracked and isomerized on the ZSM-5 catalyst surface. As in the separate bed, the base catalyst shows no selectivity towards aromatic compounds, but addition of ZSM-5 forms alkyl-benzene aromatic compounds ($C_{7-10}$). The aromatic yield shows a maximum at 0.5 g ZSM-5, and higher amounts of ZSM-5 decrease the yield.

When comparing both the beds, the maximum amount of i-$C_{5-12}$ plus aromatics (i.e., high-octane gasoline-range hydrocarbons) is formed in the separate bed with 0.5 g of the base catalyst and 0.5 g ZSM-5. For the mixed bed, the maximum gasoline-range hydrocarbons are found using 0.5 g base catalyst and 1.0 g ZSM-5.

The effect of increasing temperature on the product distribution was studied on the base catalyst and the separate bed. WGS and FTS rates are increased at 300°C, but higher temperatures do not enhance these rates further. The addition of ZSM-5 has a negligible contribution to FTS and WGS rates with an increase in temperature. Production of small-chain hydrocarbons ($C_{1-5}$) increases with an increase in temperature because of higher FTS rates. In the vapor phase, the amounts of species with low carbon number (like $CH_4$) increase more than those with higher carbon number (like n-$C_5H_{12}$), probably because of higher activation energy for the formation of species with low carbon number. The increase in the amounts of these species (except vapor-phase olefins in general, which undergo oligomerization over ZSM-5) with temperature in the separate bed is because of the combination of higher FTS rates (due to the base catalyst), cracking of long-chain molecules, and isomerization reactions. There is a greater increase of overall hydrocarbon liquid production rates between 280-300°C in the separate bed, compared to the base catalyst. This is because of reactions occurring on both the base catalyst and ZSM-5: FTS and WGS on the base catalyst, and oligomerization, aromatization and dehydration of alcohols to hydrocarbons occurring on ZSM-5. A further increase in temperature to 320°C decreases the production rate, both because of increased cracking of long-chain hydrocarbons, and also because production of $C_{1-4}$ is dominated by FTS at high temperature. Between 280-300°C, the activation energies for cracking and aromatization reactions involving n- and i-$C_{5-22}$ over ZSM-5 are greater than those for the formation reactions of these species. Further increases in temperature generally cause these species to crack to small-chain molecules. Aromatic yields are found to decrease, probably due to coke formation at 320°C. The total amount of alcohols formed by the base catalyst increases with an increase in the temperature. The extent of conversion of alcohols to hydrocarbons is not much changed with temperatures, and 280°C is sufficient for ZSM-5 to convert all the alcohols formed by the base catalyst.

In summary, the effect of adding ZSM-5 to the Fe-based AC supported FT catalyst can be seen in Figure 9. This shows in simplified form the reactions occuring over the base catalyst (Fe, unbroken arrows in the figure) and the zeolite (ZSM-5, dashed arrows). Addition of ZSM-5 to the iron-based FT catalyst alters the product distribution towards the formation of gasoline-range i-paraffins and aromatics. This occurs through the cracking of long-chain hydrocarbons, isomerization of n-paraffins, oligomerization of olefins and the formation of aromatics.

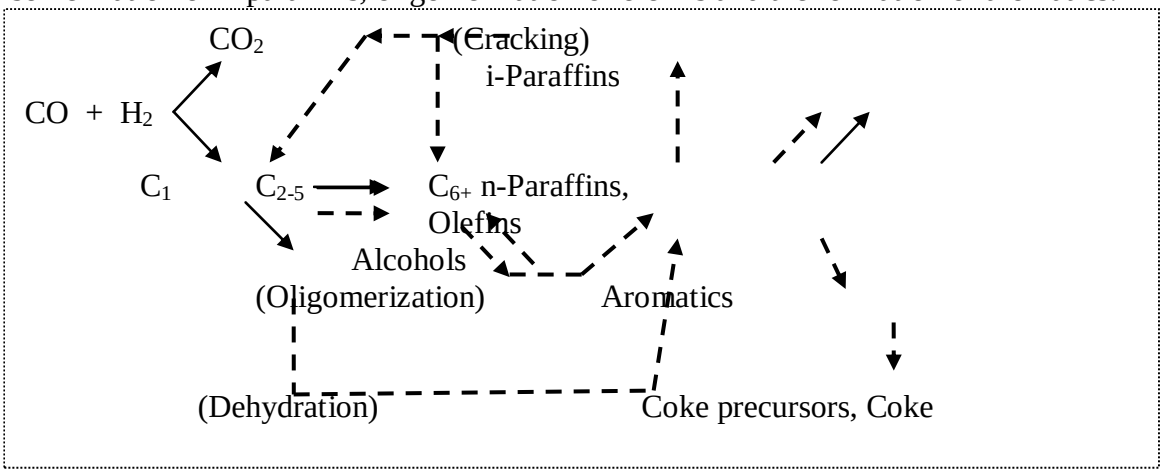


Figure 9. Summary of reactions occurring over base catalyst (Fe, unbroken arrows) and the zeolite (Z, dashed arrows).

A progressive loss of the activities of the base catalyst and the ZSM-5 occurs with increasing time on stream (TOS). The slow decline in activity of the base catalyst with TOS could be due to a decrease in iron carbide. EDX of spent ZSM-5 confirms that coke has been deposited with TOS. A loss of ZSM-5 activity is because of the decline in the active sites due to coke formation. The decline in liquid hydrocarbon production rate is partly due to increase in gas-phase hydrocarbons by a shift in the product spectrum of the FT catalyst, and partly due to coke deposition on ZSM-5. The coke deposition of ZSM-5 decreases the formation of aromatic species due to declining aromatization sites. Coke deposition on ZSM-5 has a negligible effect on the ability of ZSM-5 to convert alcohols to hydrocarbons and water.

1. Kugler, E. L., C. H. Clark, J. H. Wright, D. B. Dadyburjor, J. C. Hanson, Z. Song, T. Cai, and J. Hrbek, "Preparation, Interconversion And Characterization Of Nanometer-Sized Molybdenum Carbide Catalysts," Topics in Catalysis, 39(3-4) 257-262 (2006).
2. Clark, C.H., "Characterization and Investigation of Molybdenum Carbides on Activated Charcoal as Hydrogenation Catalysts," M.S.Ch.E. Thesis, WVU (2005); Wright, J., "Potassium-promoted Molybdenum Catalysts: Higher Alcohols from Synthesis Gas over MoC, $Mo_2C$ and $MoO_2$", M.S.Ch.E. Thesis, WVU (2006).
3. Das, T.K., E. L Kugler and Dady B. Dadyburjor, "Formation of Synthesis Gas from Propane Oxidation over Pt-on-Ceria: Effect of Ceria Surface Area, Reaction Temperature and Oxygen/Fuel Ratio", I&EC Res 48, 10796-802 (2009).
4. Dadyburjor, D.B., T.K. Das and E.L. Kugler, "Reactions for the Partial Oxidation of Propane over Pt-on-Ceria", Applied Catalysis A, 392, 127-135 (2011) .
5. Mukka, M., "Parametric Study of the Partial Oxidation of Propane over Ni- and Pt-based Catalysts", MSChE Thesis, West Virginia University (2010).

6. Iyer, M.V., L. P. Norcio, A. Punnoose, E. L. Kugler, M. S. Seehra and D. B. Dadyburjor, "Catalysis for synthesis gas formation from reforming of methane,", Topics in Catalysis 29, 197-201 (2004).
7. Shao, H.F., E. L. Kugler, W. P. Ma and D. B. Dadyburjor, "Effect of Temperature on Structure and Performance on In-house Cobalt-Tungsten Carbide Catalyst for Dry Reforming of Methane," Ind. Eng. Chem. Res. 44, 4914-4921 (2005).
8. Shao, H.F., "Bimetallic Carbides as Catalysts for Dry Reforming and Steam Reforming", Ph.D. Dissertation, West Virginia University (2006).
9. Shao, H.F., E.L. Kugler, D.B. Dadyburjor, S.A. Rykov, andJ.G. Chen "Correlating NEXAFS characterization of Co-W, Ni-W bimetallic carbide catalysts with reactivity for dry reforming of methane", Applied Catalysis A: General 356, 18-22 (2009).
10. Ma, W.-P., E.L. Kugler and D.B. Dadyburjor, "Effect of Properties of Various Activated-Carbon Supports and Supported Fe-Mo-Cu-K Catalysts on Metal Precursor Distribution, Metal Reduction and Fischer-Tropsch Synthesis," Energy and Fuels, 24, 4099-4110 (2010).
11. Ma, W.P., E. L. Kugler, J. H. Wright and D. B. Dadyburjor, "Mo-Fe Catalysts Supported on Activated Carbon for Synthesis of Liquid Fuels by the Fischer-Tropsch Process: Effect of Mo Addition on Reducibility, Activity and Hydrocarbon Selectivity" Energy & Fuels, 20, 2299-2307 (2006).
12. Ma, W.P., E. L. Kugler and D. B. Dadyburjor, "Potassium Effects on Activated-Carbon-Supported Iron Catalysts for Fischer-Tropsch Synthesis," Energy and Fuels, 21, 1832-1842 (2007).
13. Ma, W.P., E. L. Kugler and D. B. Dadyburjor "Promotional Effect of Copper on Activity and Selectivity to Hydrocarbons and Oxygenates for Fischer-Tropsch Synthesis over Potassium-Promoted Iron Catalysts Supported on Activated Carbon," Energy Fuels 25, 1931-1938 (2011).
14. Karre, A.V., A. Kababji, E. L. Kugler and D. B. Dadyburjor, "Effect of Addition of Zeolite to Iron-based Activated-carbon-supported Catalyst for Fischer-Tropsch Synthesis in Separate Beds and Mixed Beds," Catalysis Today, 198, 280-288 (2012).
15. Karre, A.V., A. Kababji, E. L. Kugler and D. B. Dadyburjor, "Effect of Time On Stream and Temperature on Upgraded Products from Fischer-Tropsch Synthesis when Zeolite is added to Iron-based Activated-carbon-supported Catalyst," Catalysis Today, accepted.

# Hydrothermal Conversion of biomass to produce biocrude, biochar and hydrogen

Ram B Gupta, Sandeep Kumar, Adam J Byrd and Hema Ramsurn
Department of Chemical Engineering, Auburn University, Auburn

**Abstract:**
Sub and supercritical water (SCW) treatment and pretreatment of biomass have been explored to obtain value-added products. In the first part of this project, microcrystalline cellulose was used as a biomass model. Pretreatment of cellulose in subcritical water reduced the degree of polymerizarion but did not affect the crystallinity of the cellulose. The overall enzymatic disgestibility of the pretreated cellulose increased, especially at temperatures above 300 °C. For the cellulose hydrolysis study, both sub and supercritical water were used to break down the feedstock into fermentable sugars. It was observed that cellulose completely dissolved at 330 °C with about 65% of cellulose converting to oligomers and monomers. When treated in the supercritical regime, the oligomers and monomers partially degrade to mainly anhydroglucose, dimers, 5-HMF and furfural. However, 80% of cellulose was converted in SCW. After studying the model compounds, the project then shifted to biomass pretreatment and treatment in sub and SCW. Switchgrass and cornstover were pretreated in an attempt to produce bioethanol and carbon microspheres. 80% of glucan digestibility was achieved by pretreatment at 190 °C for switchgrass. Cornstover required milder pretreatment conditons. A mechanism was postulated for the formation of the carbon microspheres through polymerization of phenolic compounds. As for the hydrothermal liquefaction of switchgrass, 50 wt% of the organic carbon present in the feedstock was converted to biocrude at 235 °C in the presence of 0.15 wt% potassium carbonate. Subcritical water was enough to breakdown the lignocellulosic structure of switchgrass. Reforming of feedstock in SCW to produce hydrogen was another avenue that was explored to use biomass as a fuel source. Glucose, ethanol, glycerol and biocrude were all reformed in SCW. In each study, a reaction mechanism was discussed and the activation energy of the reaction was calculated. $Ru/Al_2O_3$ was used as the catalyst, except in the case of biocrude where a suite of catalyst was tried because of the complexity of the feedstock. High temperature and dilute solutions gave high hydrogen yields while pressure did not have any effect on the yield. Finally, the biochar obtained from biomass was gasified in SCW to obtain high-quality syngas. In this study, the use of $Ca(OH)_2$ in the biochar preparation enhanced its subsequent gasification.

## 1. Study of the behavior of microcrystalline cellulose in subcritical and supercritical water

Prior to working with biomass, we studied the behavior of cellulose as a model compound in sub and supercritical water (SCW). Two main studies were carried out: hydrolysis of microcrystalline cellulose in sub and SCW and cellulose pretreatment in subcritical water to enhance subsequent enzymatic reactivity. In the first work, hydrolysis of crystalline cellulose to fermentable sugars was looked into for cellulosic ethanol production[1].Microcrystalline cellulose was treated with subcritical and supercritical water in a temperature range of 302−405 °C, at a pressure of 27.6 MPa, and residence times of 2.5−8.1 s. A cellulose/water slurry of 2.7 wt % was rapidly heated to the reaction temperature and then the reaction product was rapidly cooled in a continuous reactor. Cellulose partially dissolved in subcritical water at 302 °C and

completely dissolved at 330 °C. About 65% of cellulose converted to oligomers and monomers at 335 °C in 4.8 s and also at 354 °C in 3.5 s (Figure 1).

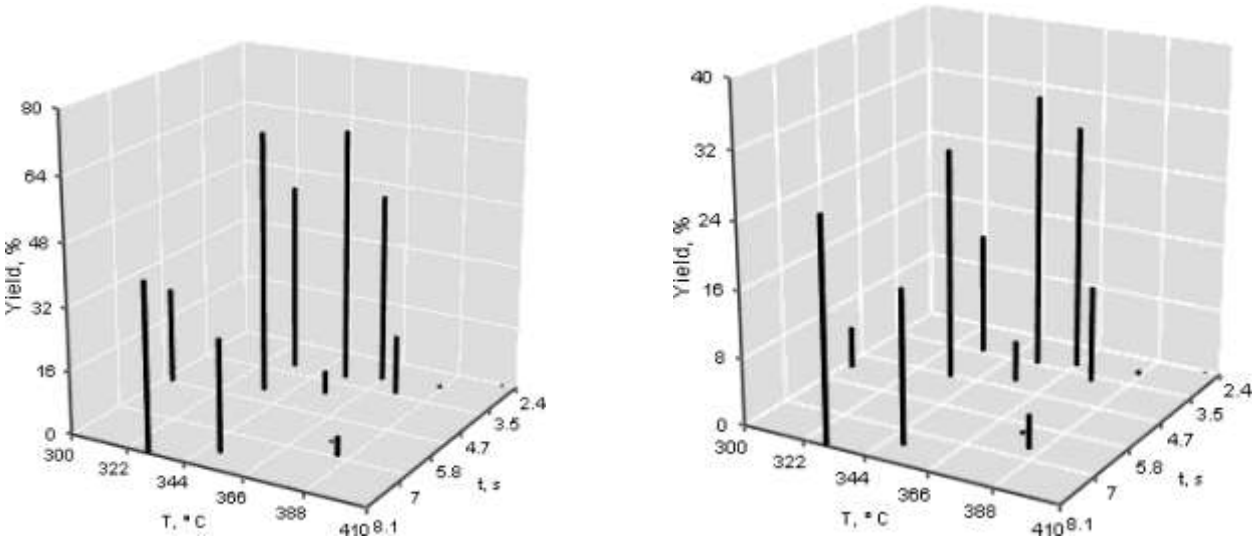


Figure 1. Yield of hydrolysis products (left) and glucose (right) obtained from cellulose treatment in subcritical and supercritical water at 27.6 MPa.

Upon increase in the reaction time or temperature to supercritical region, oligomers and monomers partially degraded to glycoaldehyde dimer, d-fructose, 1,3-dihydroxyacetone dimer, anhydroglucose, 5-HMF, and furfural. The yield of glycoaldehyde, a retro-aldol condensation product of glucose, increased with a decrease in the density of supercritical water, and the yield of degradation products, 5-HMF, and organic acids, increased with temperature and residence time. In supercritical water conditions, more than 80% of the cellulose converted into the degradation products and organic acids. The use of $K_2CO_3$ catalyst in the reaction mixture during depolymerization of cellulose in subcritical water substantially enhanced the gas formation. However, during the short residence time (4.8−5.2 s), carbonization of the residue solid did not occur.

In the second investigation [2], microcrystalline cellulose (MCC) was pretreated with subcritical water in a continuous flow reactor for enhancing its enzymatic reactivity with cellulase enzyme. Cellulose/water suspension was mixed with subcritical (i.e., pressurized and heated) water and then fed into the reactor maintained at a constant temperature and pressure. After the reaction, product was immediately cooled in a double-pipe heat exchanger. The solid portion of the product (i.e., treated MCC) was separated and tested for molecular structure and enzymatic reactivity. Experiments were conducted at temperatures ranging from 200 to 315 °C, at 27.6 MPa, and for 3.4–6.2 s reaction times. The treated MCC was characterized for degree of polymerization ($DP_v$) by viscosimetry (Figure 2), and crystallinity by X-ray diffraction (XRD).

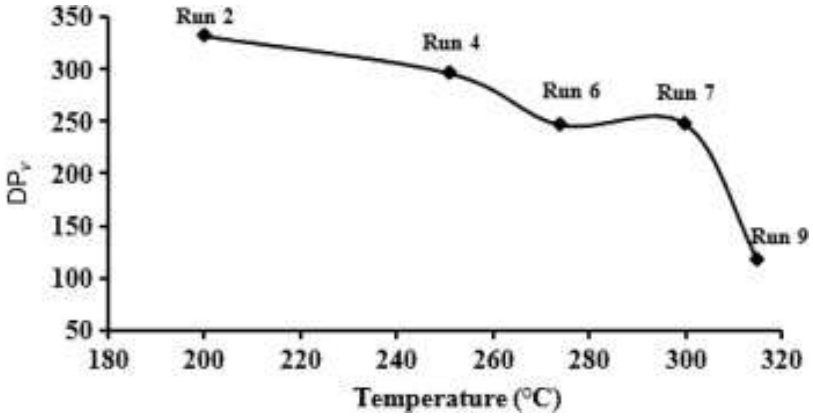


Figure 2. Degree of polymerization ($DP_v$) versus pretreatment temperature.

As expected, $DP_v$ of cellulose steadily decreased with increase in the pretreatment temperature, with a rapid drop occurring above 300 °C. On the other hand, XRD analysis did not show any decrease in crystallinity upon pretreatment but, partial transformation of celluloses I–II structure was noticed in the MCC treated at ⩾300 °C. Development of surface cracks and trenches were observed in the SEM images (Figure 3) for all the treated samples.

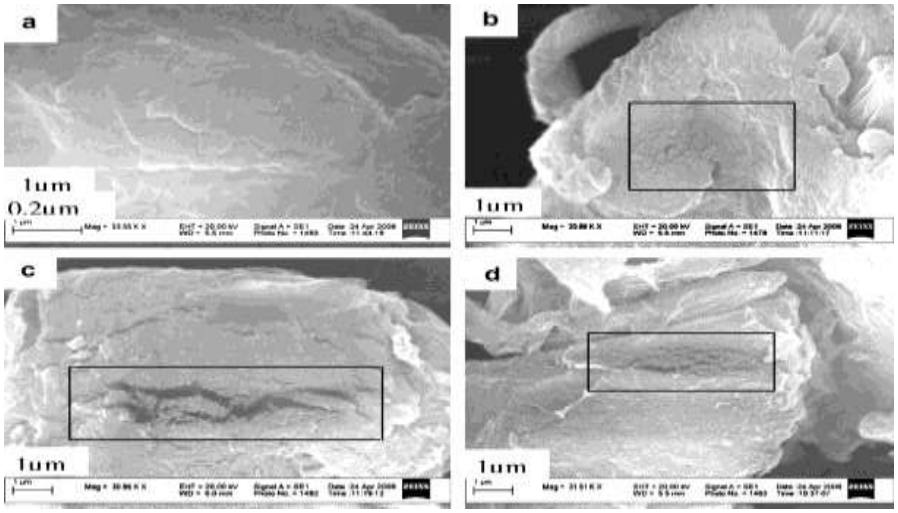


Figure 3. SEM images of samples: (a) MCC, (b) run 5 @ 275 °C, (c) run 7 @ 300 °C, and (d) run 9 @ 315 °C.

Overall enzymatic reactivity (with 60 FPU/g cellulose) of treated solid is a function of both reaction temperature as well as time. At a constant temperature, enzymatic digestibility of the treated solid increased with the reaction time, especially after the treatment at ⩾300 °C (Figure 4). Regression analysis of enzymatic hydrolysis data was carried out with Design of Experiment software (DOE PRO 2007 from Digital Computation).

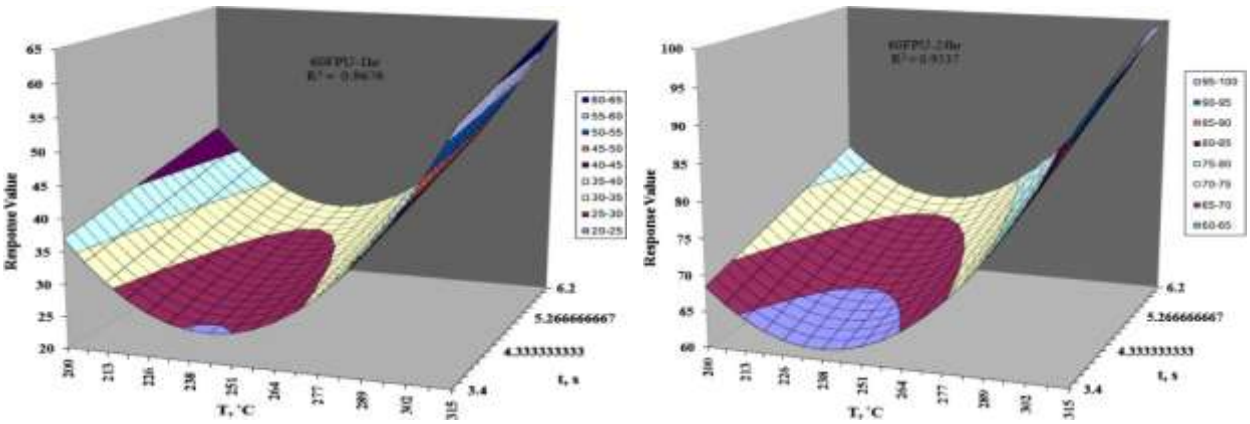

Figure 4. Plot after regression analysis of enzymatic hydrolysis data at 60 FPU and after 1 h (left) and 60 FPU and after 24 h (right).

## 2. **Hydrothermal pretreatment and treatment of switchgrass**

After cellulose was investigated in hydrothermal medium, pretreatment as well as treatment of biomass was performed. In the first study, switchgrass and corn stover were pretreated to produce ethanol and carbon microspheres. Subcritical water is an environmentally attractive solvent for organic matters and was also used to liquefy switchgrass to biocrude, which is a mixture of oxygenated hydrocarbons of varying molecular weights. Liquefaction of switchgrass in subcritical water was studied using a semicontinuous reactor in the temperature range of 235−260 °C [3]. Subcritical water was pumped through a tubular reactor packed with switchgrass particles of 40−60 mesh size. The effects of reaction temperature and catalysis by $K_2CO_3$ were examined. Potassium carbonate significantly enhanced the hydrolysis of macromolecular components of switchgrass into water-soluble products. More than 50 wt % of the organic carbon available in switchgrass was converted to biocrude after 20 min of steady operation at 235 °C in the presence of 0.15 wt % of $K_2CO_3$ (Figure 5).

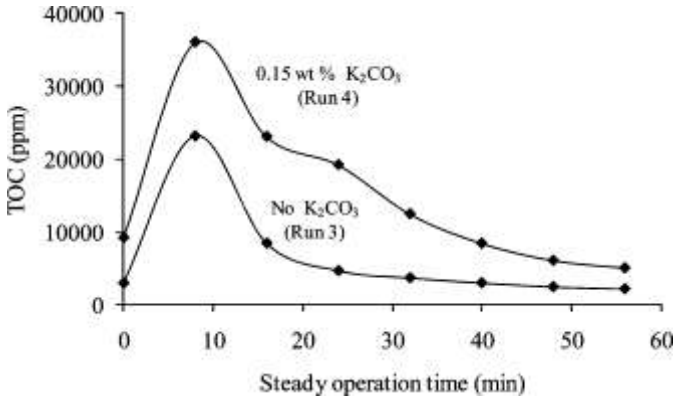


Figure 5. Total organic content (TOC) of aqueous phase versus steady operation time.

At higher temperature (260 °C), dehydration of biomass was favored over hydrolysis reactions. On the basis of chromatography and mass spectrometry analyses, biocrude

contained lignin derived products, sugars, and its decomposition products. The infrared spectroscopy and electron microscopy of residue solid revealed that the subcritical water treatment caused complete breakdown of lignocellulosic structure of switchgrass (Figure 6). In fact, the residue solid mainly contained lignin fractions.

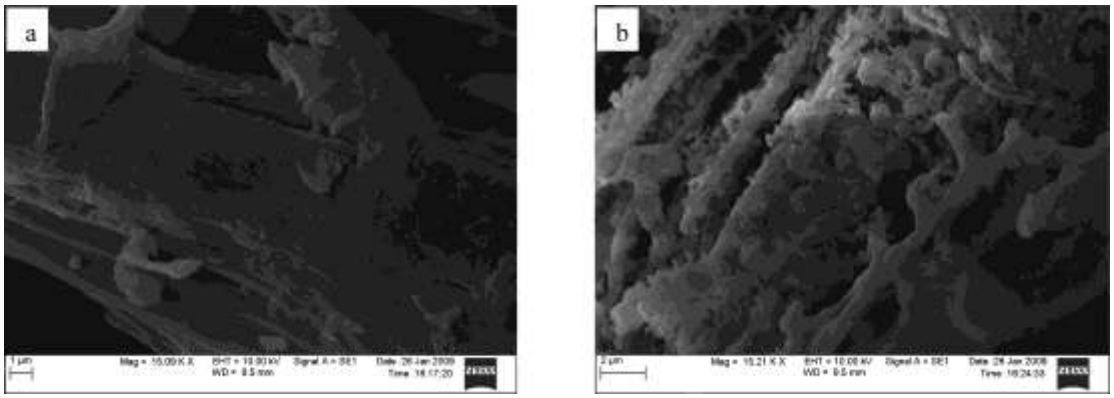


Figure 6. SEM image of (a) untreated switchgrass and (b) biochar from run 8 (235 °C & 0.15 wt% $K_2CO_{3)}$.

In order to make cellulose accessible to enzymes and for an adequate yield of fermentable sugars in ethanol production, pretreatment of switchgrass and corn stover was investigated [4] to produce bioethanol and carbon microspheres, as shown in Figure 7.

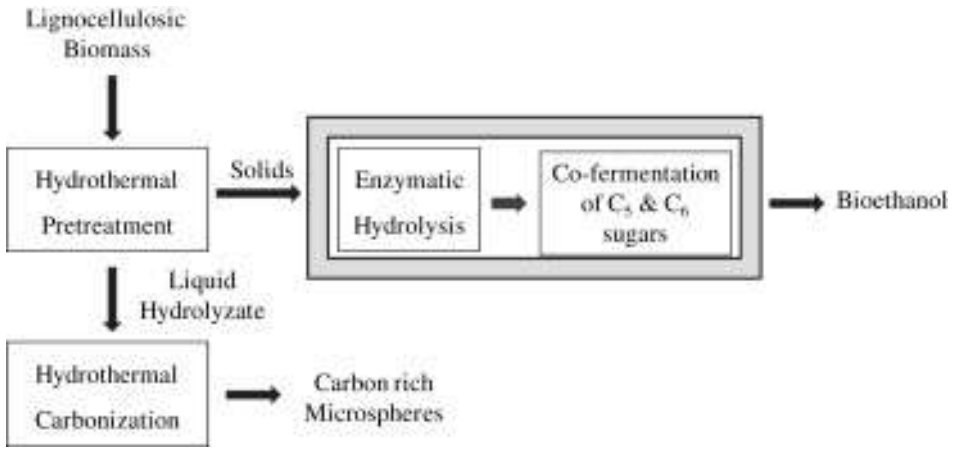


Figure 7. Proposed conversion scheme for lignocellulosic biomass to bioethanol and carbon microspheres.

Hydrothermal pretreatment was conducted in a flow through reactor to enhance and optimize the enzymatic digestibility. More than 80% of glucan digestibility was achieved by pretreatment at 190 °C. Addition of a small amount of $K_2CO_3$ (0.45–0.9 wt.%) enhanced the pretreatment and allowed the use of lower temperatures (Figure 8). Switchgrass pretreated at 190 °C only with water had higher internal surface area than that pretreated in the presence of $K_2CO_3$, but both the substrates showed similar glucan digestibility. In comparison to switchgrass, corn stover required milder pretreatment conditions.

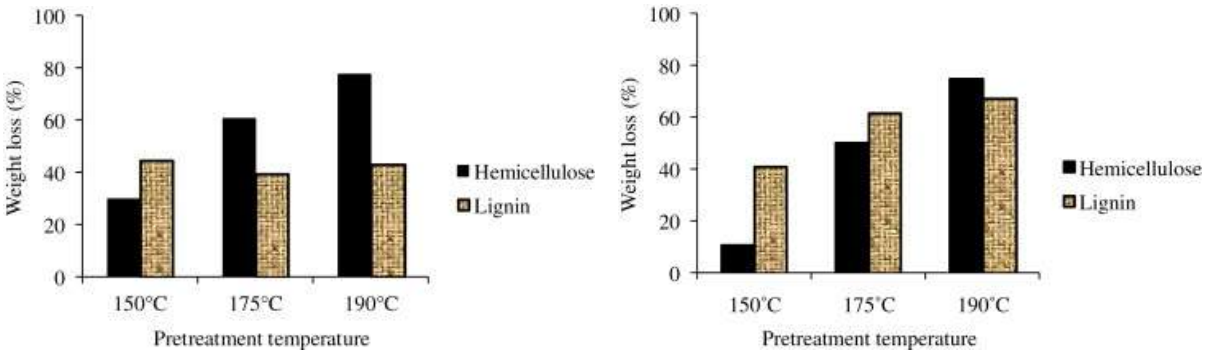


Figure 8. Percentage removal of hemicelluloses and lignin with temperature for switchgrass hydrothermally pretreated (i) at 3.4 MPa and 20 min steady operation time (left) and (ii) in the presence of 0.9 wt.% of $K_2CO_3$ (right).

The liquid hydrolyzate generated during pretreatment was converted into carbon microspheres (Figure 9) by hydrothermal carbonization, providing a value-added byproduct.

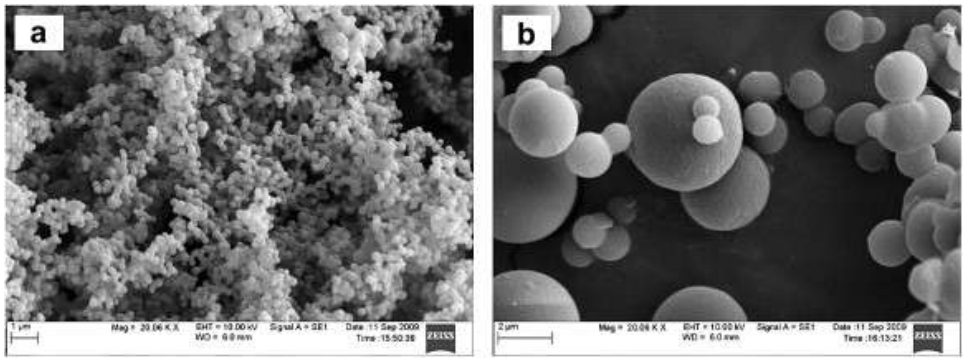


Figure 9. SEM images (at 20,000× magnifications) of carbon microspheres produced from (a) glucose solution and (b) liquid hydrolyzate of run 6 (190 °C and no catalyst).

The carbonization process was further examined by GC–MS analysis to understand the mechanism of microsphere formation (Figure 10).

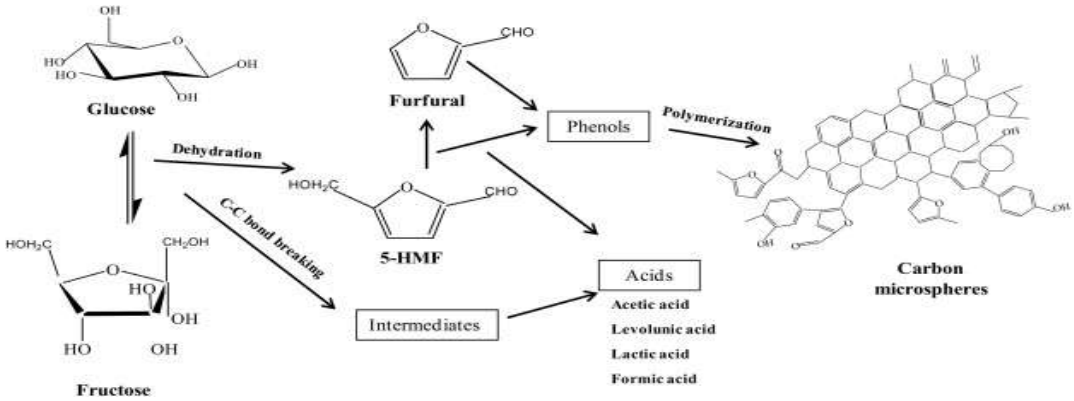


Figure 10. Simplified reaction pathway of glucose during hydrothermal carbonization reactions.

In this part of the project, model compounds as well as biocrude have been reformed in supercritical water to form hydrogen. Glucose, as a model biomass compound, as well as ethanol and glycerol were reformed using $Ru/Al_2O_3$ as catalyst. The reforming experiments were conducted in a continuous tubular reactor with and without $Ru/Al_2O_3$ catalyst at short residence times. In the case of glucose, the addition of catalyst significantly enhanced the overall conversion and hydrogen yield, and reduced methane formation. The gaseous products contained mainly hydrogen, carbon dioxide, methane, and a small amount of carbon monoxide. The effects of experimental conditions such as temperature, reaction time, and concentration of glucose in the feed on formation of hydrogen product were investigated. Experimental hydrogen yields as high as 12 mol of $H_2$/mol of glucose were obtained, which is the stoichiometric limit (Figure 11). The gas yield was sensitive to temperature, residence time, and feed concentration. High yield of $H_2$ with low CO and $CH_4$ yields were obtained at high reaction temperature and low glucose concentrations. Tar formation was observed at high glucose concentrations (>5 wt %). [5].

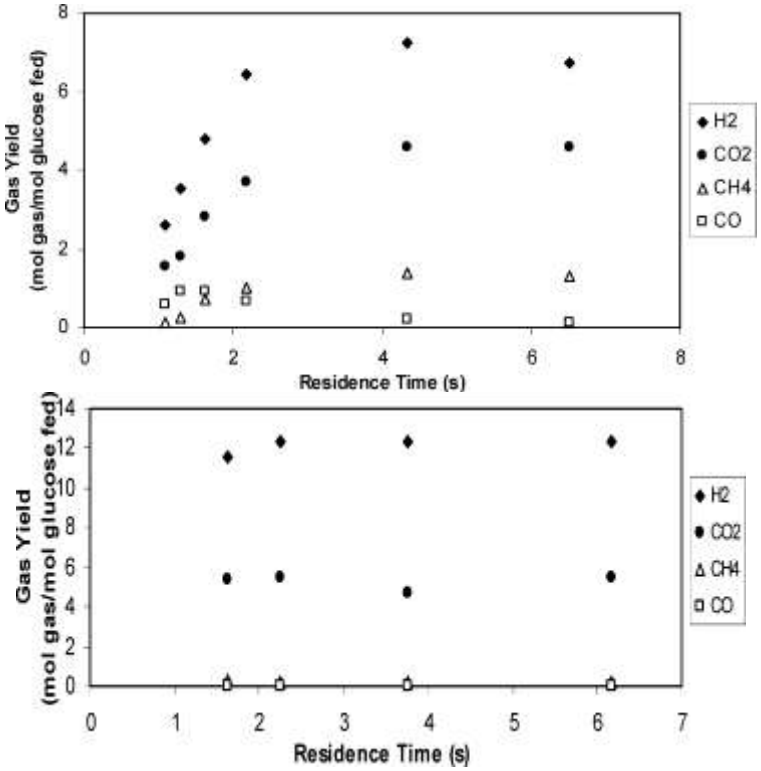


Figure 11. Hydrogen yield during empty bed (top) reforming of glucose (*T*, 700 °C; *P*, 248 bar; glucose concentration, 1 wt %) and with 2.0 g of $Ru/Al_2O_3$ catalyst (bottom).

With ethanol reforming over a $Ru/Al_2O_3$ catalyst, low methane and carbon monoxide formation were observed [6]. Hydrogen formation was favored at high temperature and at high water-to-ethanol ratio. The formation of methane was suppressed by operating at an optimal residence time, high reactor temperature, and a low feed concentration of ethanol. Excellent conversion in reaction time as short as 4 s was achieved. Pressure had a negligible effect on hydrogen yield (Figure 12) above the critical pressure, and for less than 10 wt % ethanol concentration in the feed, there was negligible coke formation.

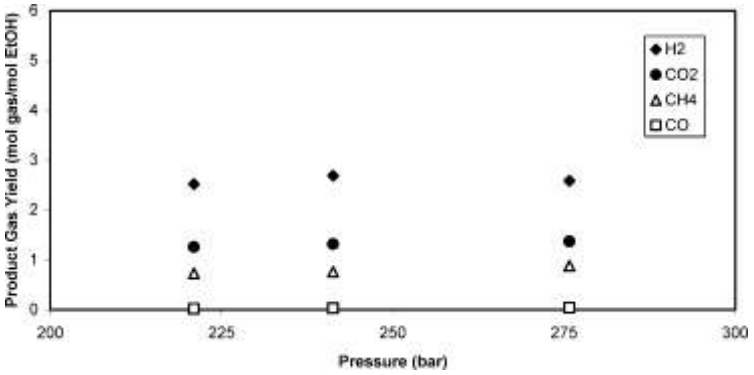


Figure 12. Effect of reactor pressure (*P*, 221 bar; 2 s in $Ru/Al_2O_3$ bed; feed concentration, 10 wt % EtOH; 1.922 g of $Ru/Al_2O_3$).

On the basis of the products obtained, a reaction mechanism was discussed. An activation energy of 65.3 kJ $mol^{-1}$ was observed. This value of activation energy is significantly lower than the values reported (96 kJ $mol^{-1}$) over $Ru/Al_2O_3$ catalyst and (82.7 kJ $mol^{-1}$) over $Co/Al_2O_3$ catalyst for reforming of ethanol in subcritical water. The lower value reported here may be attributed to the nature of the reforming media, supercritical water. Low viscosity coupled with high diffusivity can overcome mass-transfer limitations present in atmospheric steam reforming, resulting in faster rate of reaction and lower activation energy.

In the third sequel of this work [7], hydrogen was produced from glycerol by supercritical water reforming over the same $Ru/Al_2O_3$ catalyst with low methane and carbon monoxide formation. Experiments were conducted over a temperature range of 700–800 °C, feed concentrations up to 40 wt% glycerol, all at short reaction time of less than 5 s. Glycerol was completely gasified to hydrogen, carbon dioxide, and methane along with small amounts of carbon monoxide. At dilute feed concentrations, near-theoretical yield of 7 mol of hydrogen/mol (Figure 13) of glycerol was obtained, which decreases with an increase in the feed concentration. Based on a kinetic model for glycerol reforming, an activation energy of 55.9 kJ/mol was observed.

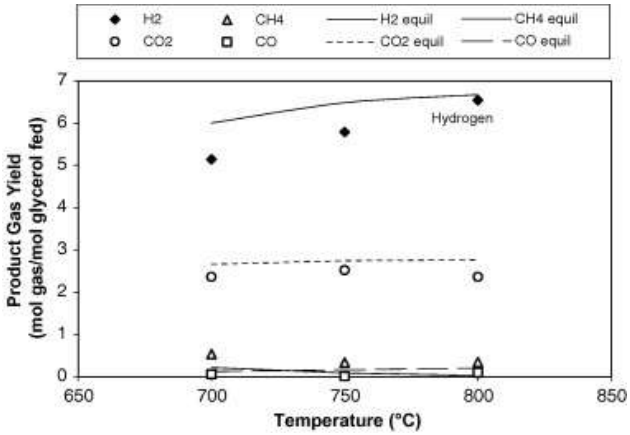


Figure 13. Effect of temperature on product gas yields. (*P*: 241 bar, 1 s residence time, feed conc.: 5 wt%, 2.0 g $Ru/Al_2O_3$.)

Biomass can be liquefied to produce biocrude for ease of transportation and processing. Biocrude contains oxygenated hydrocarbons of varying molecular structure and molecular weights, including lignin derived products, sugars and their decomposition products. It therefore was necessary to try reforming biocrude supercritically to form hydrogen [8]. In this work several catalysts were screened for hydrogen production by gasification of switchgrass biocrude in supercritical water at 600 °C and 250 bar. Nickel, cobalt, and ruthenium catalysts were prepared and tested on titania, zirconia, and magnesium aluminum spinel supports. Magnesium aluminum spinel was seen to be an inappropriate support as reactors quickly plugged. $Ni/ZrO_2$ gave 0.98 mol $H_2$/mol C, the highest hydrogen yield of all tested catalysts; however, over time, increase in pressure drop lead to reactor plugging with all zirconia supported catalysts. Titania supported catalysts gave lower conversions, however they did not plug during the course of the study. Charring of all catalysts was seen to occur at the entrance of the reactor as the biocrude was heated. All support materials suffered significant surface area loss due to sintering. Figure 14 gives the different product gas yields obtained using the suite of catalysts mentioned.

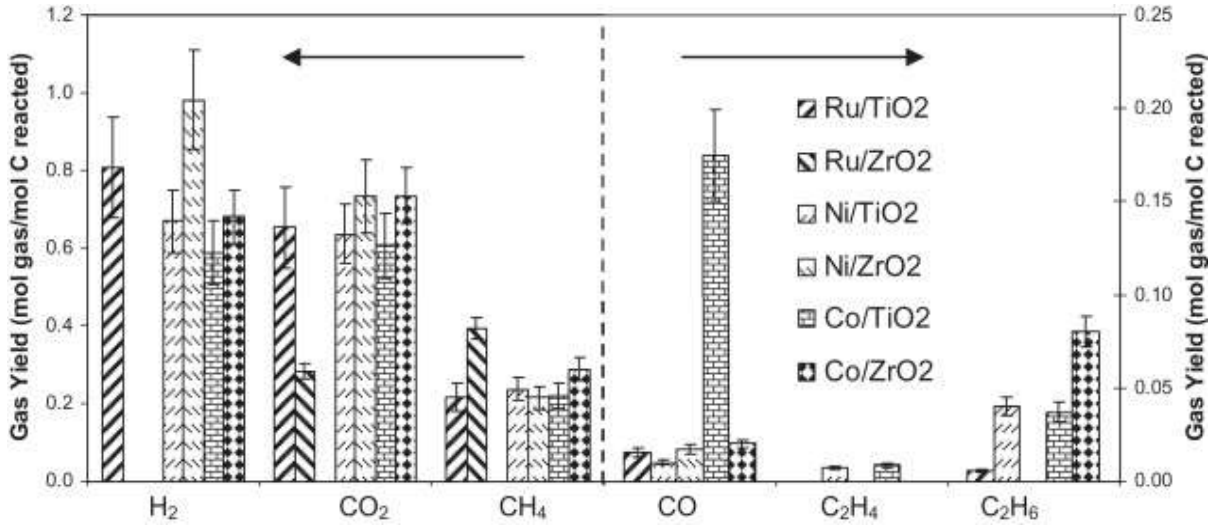


Figure 14. Product gas yields for $TiO_2$ and $ZrO_2$ supported catalysts.

## 3. **Biochar Gasification in alkali hydrothermal medium to produce syngas**

This section deals with the work done in trying to utilize the biochar produced after biomass has been liquefied. The challenges with thermal gasification of biomass to produce syngas include high transportation and drying costs of biomass and the need for high-temperature (700–1000 °C) gasifiers and conditioning of the produced gases. Some of these challenges can be addressed by first converting biomass into high-energy-density biochar before transportation and then hydrothermal gasification of biochar at the site of the Fischer–Tropsch plant for liquid fuel synthesis. In this work, a high-energy-density (>27 MJ/kg) biochar was first produced via hydrothermal carbonization of switchgrass at 300 °C, and then the biochar was gasified in hydrothermal medium at 400–650 °C [9]. The carbon gasification efficiency in hydrothermal medium was much better than that in the thermal medium. For example, at 550 °C, only 5.9% carbon gasification was achieved in the thermal medium, as compared to 23.8% in hydrothermal medium. The addition of 25 wt % $K_2CO_3$ catalyst enhanced the hydrothermal gasification to

43.8%. The gasification can be further enhanced if the biochar was passivated with a small amount of $Ca(OH)_2$ (biochar-Ca) when producing from biomass. With the use of $Ca(OH)_2$ passivation during hydrothermal carbonization and the use of $K_2CO_3$ catalysis during hydrothermal gasification, a high carbon gasification efficiency of 75% was achieved at 600 °C, using short reaction times of 5 and 30 min, respectively. With the recycle of the alkali catalyst and passivation agent, the hydrothermal process can provide an attractive alternative to thermal gasification.

Table 1. Summary of the gas composition from the different experiments at 550 °C.

| Gasification type | Biochar | $K_2CO_3$ Added (on dry basis) (wt %) | Rx time (mins) | Composition of gas (mole %) | | | | HHV MJ/Nm$^3$ |
|---|---|---|---|---|---|---|---|---|
| | | | | $H_2$ | CO | $CH_4$ | $CO_2$ | |
| Thermal | biochar | 0 | 275 | 7.6 | 0 | 6.7 | 86 | 3.4 |
| Hydrothermal | biochar | 0 | 30 | 8 | 13 | 21.8 | 58 | 10.7 |
| Hydrothermal | biochar | 2.5 | 30 | 25.3 | 0 | 20 | 55 | 10.6 |
| Hydrothermal | biochar | 10 | 35 | 11.5 | 9.3 | 26.5 | 53 | 12.5 |
| Hydrothermal | biochar | 25 | 35 | 43.5 | 1.4 | 22.7 | 32 | 13.9 |
| Hydrothermal | biochar | 50 | 90 | 50 | 0.6 | 23.3 | 29 | 14.9 |
| Hydrothermal | biochar-Ca | 25 | 30 | 43.7 | 1.1 | 23.5 | 32 | 14.3 |
| Hydrothermal | biochar-Ca | 50 | 30 | 45.3 | 6.5 | 23.9 | 24 | 15.3 |

The HHV of the residual gases were also calculated from molar compositions and the corresponding gross heating value of each component gas (Table 1). Baratieri et al.[10] pyrolyzed different species of biomass (bagasse, sawdust, grape stalks) at 800 °C and 1 bar to obtain syngas with HHV ranging from 7.3-10.6 MJ $Nm^{-3}$ while Schmieder et al.[11] reported HHV ranging from 3.8-5.3 MJ $Nm^{-3}$ by hydrothermally treating wood and straw at 450 °C. Furthermore, some experiments were carried out whereby switchgrass was hydrothermally gasified at 550 °C, with (10 wt%) and without $K_2CO_3$ and the HHV of the gases obtained ranged around 3-4 MJ /$m^3$, indicating the poor quality of the gases obtained from direct gasification of biomass. From Table 5, it can be deduced that hydrothermally treating biochar without any catalyst yields an HHV closer to pyrolyzed biomass. It is evident that the difference in operating procedures, equipment and scale of the gasification apparatus would impact on the HHV value but it can be concluded that the gas obtained from this study is of promising quality.

Adding calcium hydroxide during biochar production may have provided more accessibility, explaining why biochar–Ca gasified better. It is believed that the ash became less water-soluble, suggesting that some components in ash must have reacted with lime to form water-insoluble compounds, therefore passivating the minerals. Furthermore, according to the oxygen transfer and intermediate mechanism[12], the addition of lime is favorable for the formation of C(O), an adsorbed oxygen/oxygenated species on the carbon surface. Also, a

reducing form ($K_2O$–C) and an oxidizing form ($K_2O_2$–C) of K–C–O intercalates catalyze carbon gasification by C(O), an intermediate to the gasification pathway. Therefore, the concentration of both K–C–O and C(O) dictate the catalytic gasification, which is driven by the competition between two reactions: desorption of C(O) (reaction a) and reaction of C(O) with $K_2O_2$–C (reaction b), as illustrated in Figure 15. From the gas analysis, more $CO_2$ was formed than CO. This suggests that, in thermal and hydrothermal gasification of biochar, reaction b was favored.

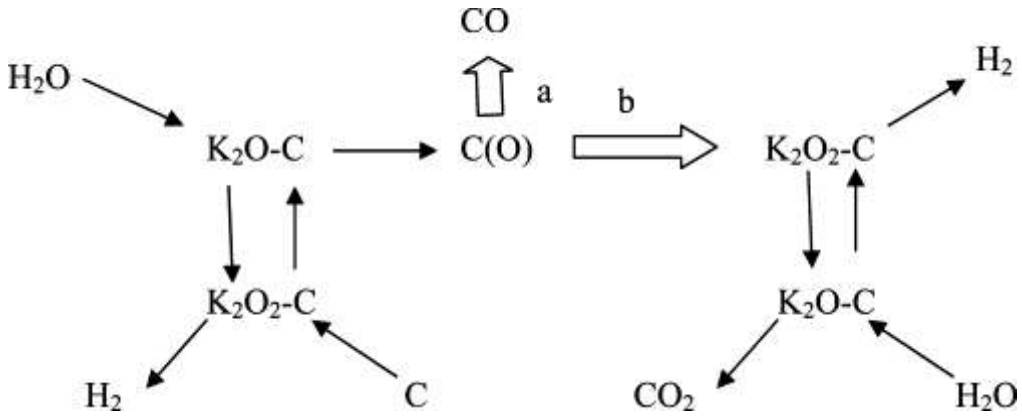


Figure 15. Oxygen transfer and C(O) intermediate hybrid reaction scheme of steam gasification of carbon by potassium.

In summary, this research has made use of water either as a solvent or reactant to facilitate a number of reactions to produce value-added compounds from biomass. In particular, sub and supercritical water have been used in a number of different conversion processes. This research has helped to

- understand the behavior of cellulose and biomass in sub and supercritical water,
- demonstrate that hydrothermal treatment of biomass to produce biocrude is fast and effective,
- show that subcritical water is an effective and benign means to pretreat biomass for subsequent bioethanol production,
- investigate SCW reforming of biocrude components like cellulose and glycerol which gave high hydrogen yields,
- prove that SCW reforming of biocrude is not simple due to the complexity of the feedstock and all catalysts investigated seem to char, and
- highlight the use of biochar in the production of high-quality syngas by using SCW gasification.

**References:**

[1] S. Kumar and R.B. Gupta, Industrial & Engineering Chemistry Research, 47 (2008) 9321.
[2] S. Kumar, R. Gupta, Y. Lee and R.B. Gupta, Bioresource technology, 101 (2010) 1337.
[3] S. Kumar and R.B. Gupta, Energy & Fuels, 23 (2009) 5151.
[4] S. Kumar, U. Kothari, L. Kong, Y. Lee and R.B. Gupta, Biomass and Bioenergy, 35 (2011) 956.
[5] A.J. Byrd, K. Pant and R.B. Gupta, Industrial & Engineering Chemistry Research, 46 (2007) 3574.

[6] A.J. Byrd, K. Pant and R.B. Gupta, Energy & Fuels, 21 (2007) 3541.
[7] A.J. Byrd, K. Pant and R.B. Gupta, Fuel, 87 (2008) 2956.
[8] A.J. Byrd, S. Kumar, L. Kong, H. Ramsurn and R.B. Gupta, International Journal of Hydrogen Energy, 36 (2011) 3426.
[9] H. Ramsurn, S. Kumar and R.B. Gupta, Energy & Fuels, 25 (2011) 2389.
[10] M. Baratieri, P. Baggio, L. Fiori and M. Grigiante, Bioresource Technology, 99 (2008) 7063.
[11] H. Schmieder, J. Abeln, N. Boukis, D. E, K. A, K. M, P. G, S. E and S. M, Journal of Supercritical Fluids 17 (2000) 145.
[12] J. Wang, M. Jiang, Y. Yao, Y. Zhang and J. Cao, Fuel, 88 (2009) 1572.

# Fischer-Tropsch, Water Gas Shift, and Related Studies

Richard D. Ernst, Edward M. Eyring, and Ronald J. Pugmire
University of Utah

During the period of this support, we have been involved in three principal catalysis projects. These involved the Fischer-Tropsch reaction, the Water-Gas-Shift reaction, and the conversion of sugars to hydroxymethylfurfural and/or 2,5-dimethylfuran. We have managed to make progress in each of these areas, and our results will be presented in sections for each. In addition to our cited publications, we have also obtained a U.S. patent dealing with the selective delivery of one metal to locations of a second metal type on a catalyst support, and we have a second U.S. patent pending, which deals with the stabilization of high surface area cerias at high temperatures.

## I. Water-Gas Shift (WGS) Chemistry.

Our work in this area was initiated due to the interest in a potential "hydrogen economy", as this reaction can be used to replace the CO in $CO/H_2$ syn-gas mixtures by $H_2$:

$$CO + H_2O \rightarrow CO_2 + H_2$$

Our strategy has been to attempt to enhance the reactivity of appropriate catalysts by the use of high surface aerogels. To this end we have employed iron aerogels, ceria aerogels, and composite iron-ceria aerogels. In some cases, the reactivity has been enhanced through the addition of 1-2% Pd.

Our work with iron aerogels [1] was spurred by the observation that addition of small quantities of Au or Pd to iron oxide catalysts led to significant rate enhancements. As high surface area iron aerogels can readily be prepared, but had not been employed for WGS catalysis, this seemed to offer potentially useful benefits. The iron aerogels were prepared by reported procedures, and found to have surface areas of approximately 422 $m^2/g$ by the BET (Brunauer-Emmett-Teller) method. However, calcination at temperatures exceeding $260^o$ led to marked reductions in surface area. Thus, $300^o$ C calcination led to a surface area of 293 $m^2/g$, and $450^o$ C led to 82 $m^2/g$. The incorporation of palladium was accomplished via the gas-phase using $Pd(C_5H_5)(C_3H_5)$, (allyl)(cyclopentadienyl)Pd, which we have found (see below) leads to greatly enhanced dispersal compared to solution phase procedures, which may be attributed to the reactivity toward protonation, by surface hydroxyl groups, of the allyl ligand. However, its incorporation in iron aerogels leads to even more facile reductions in surface area. Even for calcination at just $260^o$ C, the surface area of a catalyst with 1% Pd drops to 363 $m^2/g$.

The incorporation of Pd led to dramatic differences in TPR behavior of these catalysts. A simple iron aerogel, comprised primarily of Fe(III), is first converted to an $Fe_3O_4$ species around $370^o$ C, and then to FeO and Fe around $653^o$ C. In contrast, Pd-doped iron aerogels undergo initial reduction in the 100 – $120^o$ C range, with additional reductions occurring between 300 – $600^o$ C. The low temperature reductions for the doped catalysts have been attributed to

interactions between Fe and Pd species. XRD measurements of the pure iron aerogel revealed the presence of $Fe_3O_4$ and Fe(O)(OH) (ferrihydrite) species, whether the sample had been calcined or not. The spent Pd-containing catalysts were found to contain more $Fe_2O_3$, however.

The WGS reactivities of these catalysts were compared using a six channel fixed bed reactor operating in a temperature range of 150 – 350° C. The addition of 1% Pd led to a five fold increase in reactivity (Fig. 1), while an increase to 2% led to a further increase in rate of ~50%.

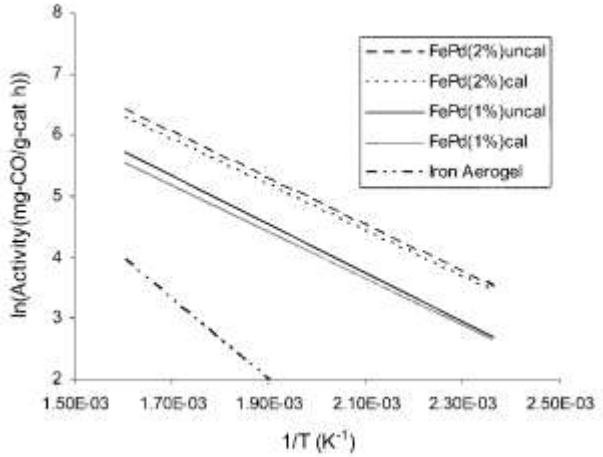


Figure 1. Arrhenius plot for the Pd-doped iron WGS catalyst activities.

While ceria/Pd catalysts have also been found to be quite active for the WGS reaction, we appear to have been the first to employ ceria aerogels in this process. This may reflect the fact that ceria aerogels undergo substantial agglomeration and hence loss of surface area even at temperatures below 300° C. However, we also found that a reported preparation for ceria aerogels did not seem to work as claimed, and as a result we devised an alternative route, based on 2-methoxyethanol [2]. These aerogels were found to have surface areas of ~345 ± 2 $m^2$/g, comparable to values for the best samples reported previously. Gas phase incorporation of Pd was carried out as above, at a loading of 1%, which led to a surface area of 284 ± 1 $m^2$/g. On reduction, the surface area further decreased, to ~136 ± 1 $m^2$/g. CO chemisorption data indicated that 7.6 ± 0.4% of the palladium atoms were located on the surface, leading to an estimation of the average radius of the palladium particles of 7.4 ± 0.4 nm. This is consistent with the observation of 15 nm diameter Pd nanoparticles by TEM.

XPS data indicated that ~ 40% of the cerium was present in the +3 oxidation state, and that 44% of the palladium was present as metal, demonstrating that the metal must have been re–oxidized during the catalytic reaction studies. An Arrhenius plot indicated the activation energies for the as prepared Pd/Ce, reduced Pd/Ce, and pure ceria aerogels to be 55 ± 2, 35 ± 6, and 77 ± 2 kJ/mol. The addition of Pd, in the reduced form, thus can be seen to have approximately cut the barrier in half.

Considering that both iron and ceria can promote the WGS reaction, and that addition of Fe(III) to a Pd/ceria catalyst led to a great increase in activity, which has been attributed to the formation of some sort of Fe/Pd alloy, it seemed reasonable to investigate 4.5:95.5 hybrid

iron/ceria aerogels [3]. The preparation of the hybrid aerogel followed a published procedure, and any incorporation of Pd was carried out in the gas phase using $Pd(C_5H_5)(C_3H_5)$. The hybrid aerogel was found to have a BET surface area of 192 ± 8 $m^2$/g, while 1% and 2% Pd incorporations led to decreases, to 151 ± 7 and 102 ± 8 $m^2$/g, respectively.

Ce XANES spectra revealed a significant difference between the as-prepared and spent catalysts. The spent catalyst exhibited a spectrum very similar to $CeO_2$, while even the as-prepared hybrid aerogel displayed significant quantities of Ce(III). Pd XANES spectra revealed in contrast little change after reaction, with any formation of Pd metal being insignificant, in contrast to what has been found for Ce-free analogues. Fe XANES and XAFS/RSF spectra indicated that the iron in all cases appeared to be present exclusively as Fe(III).

WGS reactivity studies were carried out between 150 – 350° C. An Arrhenius plot of the data led to activation energies of 81.6 ± 8.0, 70.2 ± 7.0, and 68.2 ± 2.0 kJ/mol for the 1% Pd on ceria, 1% Pd on iron-ceria, and 2% Pd on iron-ceria catalysts. Although it has been proposed that the enhancement in the latter two cases was due to the formation of an iron-palladium alloy, the XANES and XAFS/RSF data indicate that the transition metals are present as Fe(III) and

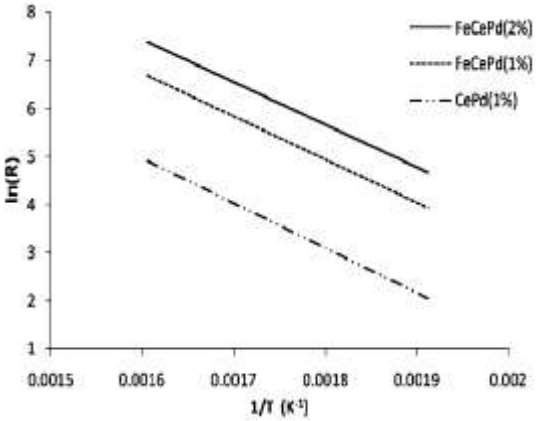


Figure 2. Arrhenius plot for the Pd-doped iron/ceria WGS catalyst activities.

Pd(II) rather than as an alloy. In contrast, pure iron catalysts tend to be converted to a nonstoichiometric magnetite phase.

In order to try to gain a better understanding of the role of cerium in the above processes, a collaborative study with the Seehra group at West Virginia was carried out [4]. A 10% ceria/silica aerogel was prepared from $Ce_2(O\text{-}i\text{-}Pr)_8(i\text{-}PrOH)_2$. XRD spectra of the as-prepared aerogel revealed only the presence of Ce(IV), specifically cubic $CeO_2$. From a linewidth analysis of the catalyst, the particle size was determined to be 2.8 ± 0.8 nm, and this was confirmed by TEM. Although no evidence for Ce(III) was seen by XRD, the more sensitive EMR spectroscopic method did reveal it to be present, consistent with the studies described above. Magnetic measurements indicated the Ce(III) content to be ~18%. The Ce(III) is incorporated in the $CeO_2$ lattice via the presence of oxygen vacancies.

II. Conversion of sugars to hydroxymethylfurfural and 2,5-dimethylfuran

Due to the interest in finding non-petroleum based feedstocks such as biomass in order to reduce our dependency on crude oil and coal, significant effort has been devoted to the conversion of sugars and cellulose into hydroxymethylfurfural (HMF) and 2,5-dimethylfuran (DMF). HMF is potentially valuable as a precursor to furans, levulinic acid, and formic acid, all

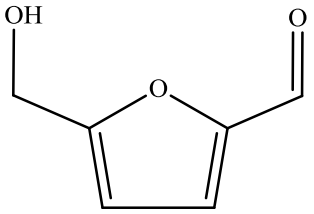


HMF

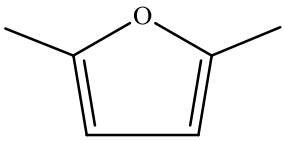


DMF

of which are currently produced from petroleum resources. In addition, HMF may be converted catalytically to DMF, which has an octane rating of 119, an energy density 40% greater than ethanol, and a very low solubility in water, making DMF attractive as an alternative fuel. Of several approaches that have been developed for the conversion of sugars to HMF, the fairly recently reported claim that Cr(II) species were active catalysts for this reaction in ionic liquid solvents, such as [EMIM]Cl (1-ethyl-3-methylimidazolium chloride), attracted our attention both

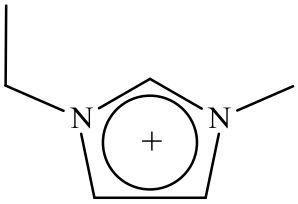


EMIM Cation

due to the importance of the process itself, and to the fact that Cr(II) complexes are notorious for their ease of oxidation, as can be appreciated by the standard one electron reduction potential for the aqueous $Cr^{+3}$ ion, -0.41 V. For Cr(II) to have any chance of participating under the reported reaction conditions, there would need to be complete exclusion of oxygen from the reaction media, which was never indicated in any of the previous reports. Even with this, the oxidation of Cr(II) by protic sources would still be thermodynamically favorable.

Two key features indicated from the start that Cr(III) should be the active catalyst. Not only is Cr(III) generally the most favorable state for chromium, Cr(III) is quite unique among first row transition metal ions in being substitution inert. This inertness is likely related to the unique catalytic activity of chromium among first row transition metals in the sugar to HMF conversion. While Co(III) complexes are also often substitution inert, few of these complexes contain significant numbers of water or other oxygen-based ligands, but instead prefer stronger field

ligands such as amines. Even though these facts clearly implicate Cr(III) as the real catalyst in the formation of HMF, the proposal that the catalyst is actually a Cr(II) species has been continually repeated in the literature. We have therefore investigated the possible catalysis of this reaction by a number of chromium complexes, as well as those of some other transition metals [5].

Though we investigated complexes of titanium, vanadium, manganese, cobalt, copper, and molybdenum, the only ones to give more than single digit percentage yields of HMF were those of Co(III) and Mo(III), both of which are like Cr(III) in being substitution inert. Further, while the previous studies required an "activation step" prior to catalysis, the use of Cr(III) complexes with weakly bound ligands, e.g., $CrCl_3(THF)_3$, gave high conversions (at least 50%) even in the absence of activation. This indicates that the coordination of the sugar to the Cr(III) ion is required for the process to occur, and the fact that no activation was required for $CrCl_3(THF)_3$ is then clearly understandable due to the weak coordination by THF. In addition, the use of the unusual Cr(IV) species, chromium tetrakis(*t*-butoxide), $Cr[OC(CH_3)_3]_4$, also led to catalysis. Just as Cr(II) would be oxidized to the more favorable Cr(III), so too would Cr(IV) be reduced to the more favorable Cr(III). In accord with this expectation, the Cr(IV) complex was active, and gave an unoptimized conversion of 51%.

Two key variables that have not been fully optimized are the time and temperature of the reaction. Using $CrCl_3(THF)_3$ as the catalyst at $100^oC$, an HMF conversion of 57% may be obtained after 1 hour, which increases to 71% after 2 hours, but then decreases to 56% after ~ 3 hours. Thus some improvement in conversion might still be obtainable, or alternatively, should there be a way to extract the HMF out as it is being formed, one might achieve even more dramatic results.

III. Iron Based Fischer-Tropsch (FT) Studies

For these studies, it was necessary to construct two new Fischer-Tropsch reactors, the details of which will not be included herein, though they may be found in previous reports, beginning with our final quarterly report of 2006. Our first two studies utilized iron supported on a mesoporous structured silica, SBA-15. This was prepared by a published procedure, and aluminum was incorporated using $AlCl_3$, so that an Al/Si ratio ranging from 0 – 0.033 was obtained [6]. Subsequently iron was incorporated by solution phase absorption, so that the iron content would be 20%. The samples had surface areas ranging from 490 – 580 $m^2/g$, and average pore diameters of 5.4 – 5.5 nm. XAFS and Mössbauer data nicely agreed on the iron components, which were primarily ferrihydrite (46 – 79%) and $Fe_2O_3$ (21 – 54%) phases. While ferrihydrite itself may be converted cleanly to $Fe_2O_3$, it was found that when supported on SBA-15, this became more difficult. These studies were also carried out on the spent catalyst, which was found to be composed of a mixture of iron, iron oxides, and iron carbides.

Perhaps the most notable observations related to some marked effects brought about by the relatively small amounts of aluminum. The catalytic studies revealed that the aluminum led to a dramatic decrease in the induction period, which would generally be long for an iron-based FT catalyst. In addition, with the Al/Si ratio of 0.010, the $C_{11+}$ fraction increased from 0.50 to nearly 0.80, though further increases in the aluminum content reversed this trend.

In the second study dealing with iron-based SBA-15 catalysts [7], a detailed comparison has been made of the suitabilities of $^{57}$Fe Mössbauer spectroscopy and four different XAFS spectroscopic methods to assess the relative contents of hematite and ferrihydrite in 11 iron-based catalyst formulations. The four XAFS methods consisted of least-squares fitting of iron XANES, d(XANES)/dE, and EXAFS ($k^3$ chi and $k^2$ chi) spectra to the corresponding standard spectra of hematite and ferrihydrite. The comparison showed that, for this particular application, the EXAFS methods were superior to the XANES methods in reproducing the results of the benchmark Mössbauer method in large part because the EXAFS spectra of the two iron oxide standards were much less correlated than the corresponding XANES spectra. Furthermore, the EXAFS and Mössbauer results could be made completely consistent by inclusion of a factor of $1.3 \pm 0.5$ for the ratio of the Mössbauer recoilless fraction of hematite relative to that of ferrihydrite at room temperature (293 K). This difference in recoilless fraction is attributed to the nanoparticulate nature of the ferrihydrite compared to the bulk nature of the hematite. Some possible alternative non-least-squares XAFS methods for determining the iron contents were discussed, in addition to potential criteria that could be used for deciding whether or not the least-squares XANES methods should be applicable to other situations.

Our third study focused on the use of iron aerogels and xerogels as FT catalysts [8]. We had already demonstrated that iron aerogels could serve as active catalysts for the WGS reaction, and it seemed reasonable to extend their use to FT catalysis. The iron aerogels have a particular advantage over iron doped aerogels in that the former are significantly stronger mechanically. We therefore carried out the first studies of the FT activities of iron aerogels, and iron aerogels and xerogels to which a potassium promoter was added.

The iron aerogels, with and without 5% K incorporation, had respective surface areas of 380 and 422 $m^2/g$, which decreased to 240 and 293 $m^2/g$ after calcination at 300$^o$ C. Their average pore diameters were found to be 255 and 300 Å. The respective values for the iron xerogel with 5% K incorporation were found to be 304 and 56 $m^2/g$, and 81 Å. The spent catalyst, which had been largely converted to iron carbides, had a surface area of only 10.2 $m^2/g$, but still a reasonably large pore diameter of 165 Å. TPR data for the various calcined aerogels and xerogels were all similar, showing reduction of $Fe_2O_3$ to $Fe_3O_4$ at ~370$^o$ C, and a broad peak centered near 650$^o$ C for further reduction to FeO and Fe. Mössbauer spectroscopy revealed that the various catalysts were all similar prior to reaction, and resembled ferrihydrites and other non-hematite containing catalysts supported on SBA-15. However, the spent catalysts differed significantly. The spent K-incorporated aerogel catalyst was shown to be primarily the carbide $\chi$-$Fe_5C_2$, with only about 3% magnetite. Similarly, the spent K-incorporated xerogel catalyst was primarily the carbide, with 3% magnetite, but also 18% $Fe_2O_3$. In contrast, the spent iron aerogel catalyst itself was composed primarily of magnetite (66%), followed by the carbide (29%) and $Fe_2O_3$ (5%). As the carbide phase is the active FT catalyst, the significant quantities of oxide in the spent iron aerogel and K-incorporated xerogel catalysts account for their lower activities (vide infra).

The FT activities of these catalysts were studied at a pressure of 100 atm (2:1 $H_2$:CO) and a temperature of 265$^o$ C in a fixed-bed reactor. The pure aerogel was found to lead to a conversion of ~ 14%, while the addition of the potassium promoter brought about an increase to 35%. This

is comparable to that of a catalyst composed of 20 wt% Fe loaded onto a similarly high surface area SBA-15 support. Even with the potassium promoter, the iron xerogel catalyst led only to ~ 7% conversion. For the K-promoted aerogel catalyst, significant quantities of hydrocarbon up to at least 32 carbon atoms were observed, with the maximum occurring around 20.

Our fourth iron-catalyzed FT study utilized ferrihydrites (FHYD) as the catalyst [9]. These naturally occurring substances are formulated as $Fe(O)(OH)(H_2O)_n$, and as a result of their nanoporous natures, have high surface areas and pore volumes. Previous reports by SASOL in South Africa indicated that these catalysts mainly produced olefins and alcohols. However, we prepared a new kind of synthetic doped amorphous two-line FHYD containing aluminum and copper, which are not usually found in nature. NMR data reveal that the Fischer-Tropsch oil produced with our amorphous ferrihydrite catalysis is mostly straight-chain *n*-paraffins.

The Fe:Al:Cu ratio in the new ferrihydrite was found to be 106:25:5, with its surface area being 311 $m^2/g$. Subsequent potassium impregnation (0.3%) and calcination at 400$^o$ C led to a surface area of 230 $m^2/g$. This material was then used in the catalytic studies, following a hydrogen reduction step. XRD spectra for the calcined and uncalcined materials were similar to typical ferrihydrites; however, subsequent reduction then produced a sample showing additional lines due to $Fe_3O_4$ and $FeAl_2O_4$. Mössbauer spectroscopic data were in accord with these conclusions, and also revealed for the spent catalyst a composition of 41% $Fe_2O_3$, 36% $Fe_5C_2$, and 23% $Fe_3O_4$. Cu XANES data revealed that the metal was present as the cupric ion. TEM and other data revealed that the initially prepared materials were amorphous and comprised of particles with an average size of ~ 2 nm. These particles were then grouped into nanoclusters with sizes on the order of 50 – 200 nm.

After promotion with potassium, these FHYDs were found to have high activities as catalysts for the Fischer−Tropsch conversion of syngas to liquid fuels over a period of ~100 h in a fixed bed reactor at 265° C and 100 psig pressure. The methane selectivity was ~ 12%, and products with up to at least 32 carbon atoms were readily observed. Some 72% of the oil component was found to lie in the kerosene/jet/ diesel fuel range, ~ $C_{10–20}$. A comparison of preliminary 100 h data for the synthetic doped FHYD catalyst with those of a commercial fixed-bed catalyst pretreated under similar conditions suggested somewhat better catalytic activity of the synthetic doped FHYD than that of the commercial fixed-bed catalyst. Our amorphous ferrihydrite Fischer-Tropsch catalyst has attracted some licensing interest from entities outside of the university environment.

## IV. Cobalt Based FT Studies

In our first cobalt on aerogel FT study, loadings of 2, 6, and 10% Co were obtained for a silica aerogel [10]. These samples, after the initially incorporated cobalt salts were reduced with hydrogen, were found to have BET surface areas in the range of 570 – 798 $m^2/g$, and mean pore diameters ranging from 21.6 – 36.9 nm. TEM images revealed that for the 2 and 6% Co catalysts, the cobalt was present in nearly spherical form, having respective diameters of 50 and 70 nm, while the 10% Co sample was observed to form needles of crystalline cobalt. We suspect that there is a critical Co concentration, between 6 and 10%, during the supercritical drying process that leads to the difference. Interestingly, CO chemisorption measurements revealed that

on increasing the cobalt content from 2 to 6%, the dispersion (amount of surface Co metal) increases from 0.15 to 0.75%, which is opposite to the trend expected for particles available on a spherical surface. This may reflect a higher surface metal oxide content for the smaller particles, and is also consistent with reports that the extent of reduction of cobalt depends on the cobalt particle size.

Samples with each of the cobalt loadings were also studied by TPR. Two reduction steps were observed for each below 500$^o$ C, which have been typically assigned to reductions of $Co_3O_4$ to CoO, and then CoO to Co. For the 10% Co sample, there was also a significant reduction step around 680$^o$ C, which could be due to the presence of cobalt silicate type structures. Conceivably, their formation could also be involved in the observed formation of needle-like crystals for the 10% samples.

The samples were examined for FT activity using a 2:1 $H_2$/CO ratio, a pressure of 100 psi, and a temperature of 265$^o$ C. The methane selectivities were fairly low, ranging from ~ 6 – 12% as the Co content decreased. The distributions had maxima around the $C_{9\text{-}10}$ range, and for the 10% cobalt catalyst, almost half of the product was larger than $C_9$. This is significantly greater than the 39% found for a related catalyst on a SBA-15 support operating at 230$^o$, and the former number ought to be even greater still were the 10% catalyst operating at this lower temperature. Notably, while the olefin contents ranged from ~ 3 – 18% for the 6% and 10% cobalt catalysts, the value for the 2% catalyst ranged from about 30 – 45%, depending on carbon number. Further, the relative reaction rates for the three catalysts were found to be 1:3.78:4.25. Thus, a reasonable increase was seen on going from 2 to 6% Co, but little change in going to 10% Co. This issue was then addressed in two subsequent studies.

The more complex nature of the 10% Co/Aerogel catalyst was further investigated by XRD, TEM, and magnetic measurements [11]. As noted above, the metallic Co component is present as randomly oriented nanoneedles. XRD data revealed several species that were not present in the 2% Co/Aerogel catalyst. These included Co (present in spent 2% catalysts), nanosized CoO, and a cobalt silicate hydroxide, which may be approximated as $Co_3(Si_2O_5)_2(OH)_2$. The silicate has been believed to be one of the cobalt forms that would undergo reduction only at higher temperatures, and thus this could explain the anomalously low reactivity of the 10% Co catalyst. Magnetic data also supported the presence of both nanosized Co and CoO, and further demonstrated that these were present as separate entities. Given that the presence of surface hydroxyls in the above catalysts appeared to allow for the formation of the silicate phase, it seemed that one might improve the reactivities by silylation of the hydroxyl groups. This was studied using SBA-15 as the support, with a cobalt content of 6% [12]. The silylation was brought about using $[(CH_3)_3Si]_2NH$, hexamethyldisilazane. As this necessarily had to be done following isolation of the solid SBA-15, the cobalt incorporation needed to be carried out via the gas phase. This was readily accomplished using $Co(\eta^4\text{-}C_8H_{12})(\eta^3\text{-}C_8H_{13})$, (1,5-cyclooctadiene)(cyclooctenyl)cobalt. XRD patterns revealed that the fundamental structure of the SBA-15 was retained after the silylation and cobalt incorporation steps, as was the average pore diameter (8.07 – 8.09 nm). While silylation led only to a slight decrease in surface area, the metal incorporation caused a drop from over 700 to ~ 420 – 460 $m^2$/g.

TPR studies revealed that the reduction occurring in the range of 420 – 570° C for the unsilylated sample was absent for the silylated species. The observed reduction percentage also differed, being 15% for the unsilylated sample but 45 – 49% for silylated samples. The reduction process occurring around 600 - 700° C was observed for all samples, and in fact was significantly larger for the silylated samples. Nonetheless, the silylated samples were found to give significantly greater CO conversions, 9.6 – 10.7%, vs. the 5.2% for the unsilylated sample. The methane selectivity also decreased dramatically, from 12.5% to 3.9 – 4.1%, while the $C_{10+}$ selectivity increased, from 4.4 to 12.2 – 17.0%. The chain growth probability increased from 0.83 to 0.86 – 0.90. Overall it appears that the silylation process provides catalysts which bear significant advantages over their unsilylated counterparts. It seems possible that this could provide for a cost-effective alternative to the addition of precious metals such as ruthenium to cobalt FT catalysts.

A small and ultra-small angle X-ray scattering (SAXS, USAXS) study was carried out on the 2 and 10% Co/Aerogel samples in order to gain a better understanding of their general structures [13]. The data revealed the presence of ~ 15 Å micropores, 50 Å mesopores, and Co precipitation domains of ~ 1000 (10% Co) and 1700 Å (2% Co). The observed reduction in the cluster sizes upon reduction appeared counterintuitive, and might be taken as an indication of the occurrence of Ostwald ripening, through which smaller crystallites become replaced by larger ones. However, it could also be that the observation reflected instead a reordering of the elongated particles toward more spherical shapes.

Additional insight concerning the aerogel structures has been obtained via solid state $^{29}Si$ NMR studies, which have been carried out with and without the addition of the metal catalyst component [14]. There are five different general silicon environments that could be present in an aerogel, designated as $Q_n$, for which n denotes the number of attached OSi units to a given silicon atom, and thus ranges from 0 to 4. This means that there would be 4-n terminal oxygens attached as well. The spectra only revealed the presence of the Q2 (internal chain), Q3 (chain branching), and Q4 (cross-linking) sites. In all samples, the $Q_4$ species, with no terminal oxygen atoms, dominated (~ 62 – 67%), followed by $Q_3$, with one terminal oxygen atom (~ 30 – 34%), and $Q_2$, with two terminal oxygen atoms (~ 3 – 6%). Calcination of the samples led to a 1.4 – 4.8% decrease in the $Q_3$ population, which was offset by a 1.5 – 4.8% increase in the $Q_4$ population. The incorporation of 2% Co in the sample led to greater line broadening and poorer resolution of the three silicon environments. The $Q_2$ contribution in particular appeared smaller and nearly indistinguishable. In addition, the $Q_4$ component appeared more dominant relative to the $Q_3$ component, paralleling the effect of calcination.

It was also observed that both ferrocene and ruthenocene ($M(C_5H_5)_2$, M = Fe, Ru) could be incorporated into the aerogel structure via the gas phase. The aerogels took on the colors of the metallocenes, without any chemical reaction taking place. Solid state $^{13}C$ NMR spectra for these samples could be obtained even without spinning, indicating that the metallocenes were rapidly tumbling in their aerogel hosts. The respective line-widths in the solid state were found to be 97 and 198 Hz, compared to the 74 and 168 Hz values determined from solution studies.

As industrial cobalt FT catalysts often employ ruthenium for activation purposes, we have been seeking methods by which the ruthenium could be more effectively utilized (e.g., see following Patent section). One way in which this might be done would be to use metal

complexes in which the two metals were already in close proximity. While numerous ligands have been devised to accomplish this goal, and while dozens of mixed mixed Co/Ru complexes have been prepared, prior to our work these all involved complicated synthetic routes and/or expensive ligands, many of which incorporated heteroatoms such as phosphorus which would be detrimental to most catalysts. Nothing that could be considered to be a simple coordination complex had been devised. We have addressed this issue through the use of pyrazole (1,2-$C_3N_2H_4$) and the related (by deprotonation) pyrazolyl anion as ligands [15]. The anionic form is well known to be able to bridge two metals. We first devised a route to $Ru(C_3N_2H_4)_4(C_3N_2H_3)_2$ (below left), which had two deprotonated ligands present in the coordination sphere, ready to coordinate to other metal centers. Addition of an appropriate cobalt complex indeed led to the desired complex (below right), whose structure was confirmed via an X-ray diffraction study.

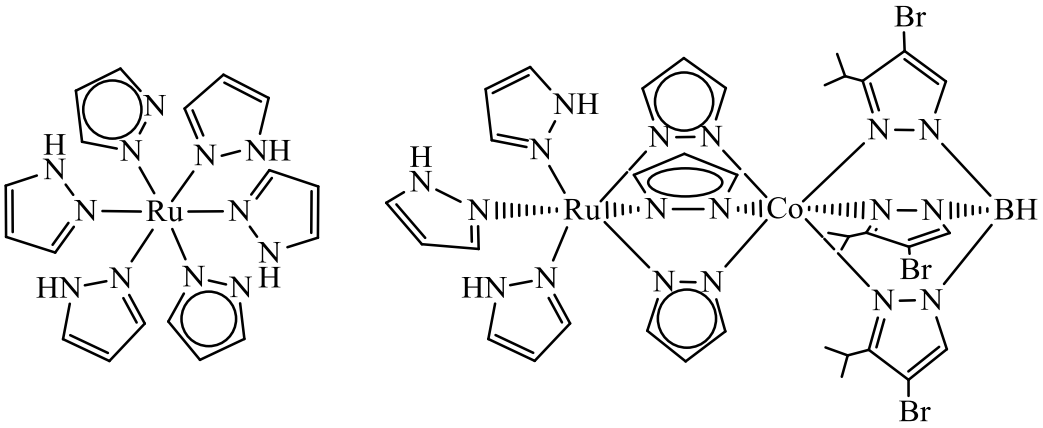


Although this method leads to a 1:1 ratio of Co to Ru, far greater than desirable for industrial FT application, we have also succeeded in preparing a dicobalt complex with these nitrogen-based ligands, and it should be amenable to the incorporation of ruthenium. Furthermore, others have reported a polymeric cobalt complex with these ligands, which should allow for the isolation of heterometallic Co/Ru structures having much higher Co/Ru ratios. Our study then represents something of a "proof of concept" that one should be able to prepare related (and even simpler) complexes containing virtually any combination of metals.

## V. Additional NMR Investigations

One other solid state NMR study was carried out on bicycloheptadiene and 1,5-cyclooctadiene complexes of Mo, Ru, Pd, and Pt, in order to obtain $^{13}C$ chemical shift tensor components which could be correlated with theoretical calculations [16]. Notably, while there were significant changes in the principal values of the chemical shifts, the orientations varied less than 10° from those found in the free dienes. The most shielded component is oriented perpendicular to a given olefin plane, the least shielded component lies in the olefin plane but perpendicular to the C=C bond, and the intermediate component is then oriented along the C=C bond. With the exception of "(bicycloheptadiene)$RuCl_2$", very good agreement between

experimental and theoretical values was obtained (standard deviation of ~ 8 ppm). However, for the ruthenium complex, a deviation of 42.2 ppm was observed, based upon a monomeric structure model. This would seem to be a result of the fact that this complex has long been believed to be polymeric, and indeed the use of an approximate associated model led to a more reasonable standard deviation of 12.5 ppm. Thus, this NMR method has been shown to be a useful tool for assessing structural arrangements for metal complexes. This can be especially important in cases involving insoluble species such as polymers, which might be difficult to crystallize.

## VI. Miscellaneous Studies

Two-stage catalyst systems have been developed for the selective reduction of $NO_x$ by $NH_3$ at low temperatures [17]. In one stage, NO is oxidized by $O_2$, while in a second stage, the selective catalytic reduction (SCR) of $NO_x$ takes place. Three prospective catalysts have been studied, including 1% Pt on alumina, 20% Cu on alumina, and 1% Pt/20% Cu on alumina. The BET surface areas of these catalysts were found to be 148, 90, and 108 $m^2/g$. XRD data demonstrated that the latter two had similar crystallite diameters, 45 and 54 nm, respectively, while any Pt must have been highly dispersed. TPR studies revealed that the behaviors of the Cu-containing catalysts were indistinguishable. A peak present around 400 C for the 1% Pt catalyst was not present for the Cu-containing catalysts, perhaps correlating with the much diminished CO chemisorption observed for the 1% catalysts upon incorporation of Cu. Thus, while 38 micromoles of CO could be absorbed per gram of the 1% Pt catalyst, that dropped to 2 micromoles for the 1% Pt/20% Cu catalyst. The Pt/alumina catalyst was found to have the highest NO oxidation and $NO_x$ removal efficiencies of the three catalysts. These efficiencies were decreased by the presence of water vapor. However, a tandem arrangement utilizing separate beds of the Pt/alumina and Cu/alumina catalysts was found to have the highest SCR performance at temperatures below 200° C, regardless of the presence or absence of water.

## VII. Patents

A U.S. patent has been issued for a process that allows one to specifically target one metal by another through a redox reaction [18]. As an illustration of this, cobaltocene, $Co(C_5H_5)_2$, is thermodynamically capable of reducing many metal oxides to the metals. Thus, if one has such an oxide on a support and cobaltocene is introduced via the gas phase, there will be an electron transfer from the cobaltocene to the metal oxide, which will anchor the resulting cationic cobalt ion near the other metal. This then provides a more selective way of bringing about the association of multimetallic arrangements as compared to simple and more random solution phase processes. Support for our hypotheses has been provided by reactivity studies, which revealed that the use of cobaltocene led to more active catalysts than when the relatively redox-inactive (1,5-cyclooctadiene)(cyclooctenyl)cobalt was used, and also from STEM data obtained by the Huffman group, which revealed a strong correlation between the locations of Co and Ru when cobaltocene was delivered to supported ruthenium oxide surfaces.

As one can recognize from our WGS projects above, the availability of high surface area ceria would be very important, but this is thwarted, at least at higher temperatures, by the dramatic agglomeration that occurs on heating. As an alternative, it became of interest to see if silica aerogel could be used as something of a scaffold on which ceria could be deposited, yielding the equivalent of a more robust ceria aerogel. This approach not only would yield a stronger, yet still highly porous support structure, it would also reduce the amount of the more expensive ceria required for a given amount of support.

Indeed, we have found that the very hydrolytically sensitive $Ce_2(O\text{-}i\text{-}C_3H_7)_8\cdot(i\text{-}C_3H_7OH)_2$ seems to incorporate very well, to at least 10%, into silica aerogel via standard solution methods, while cerium ammonium nitrate (CAN) can be used to achieve incorporations of at least 30 - 40%. The resulting aerogel-supported ceria takes advantage of the high surface area of aerogel to yield surface areas for ceria-based catalysts that have previously not been achieved. Aerogel surface areas above 600 $m^2/g$ were achieved with Ce loadings of 10% and well above 350 $m^2/g$ for loadings of 40% Ce (see Figure 3). Undoped aerogels prepared similarly have surface areas around 700 $m^2/g$, while traditional ceria catalysts tend to have surface areas in the range of only 30 to 215 $m^2/g$.

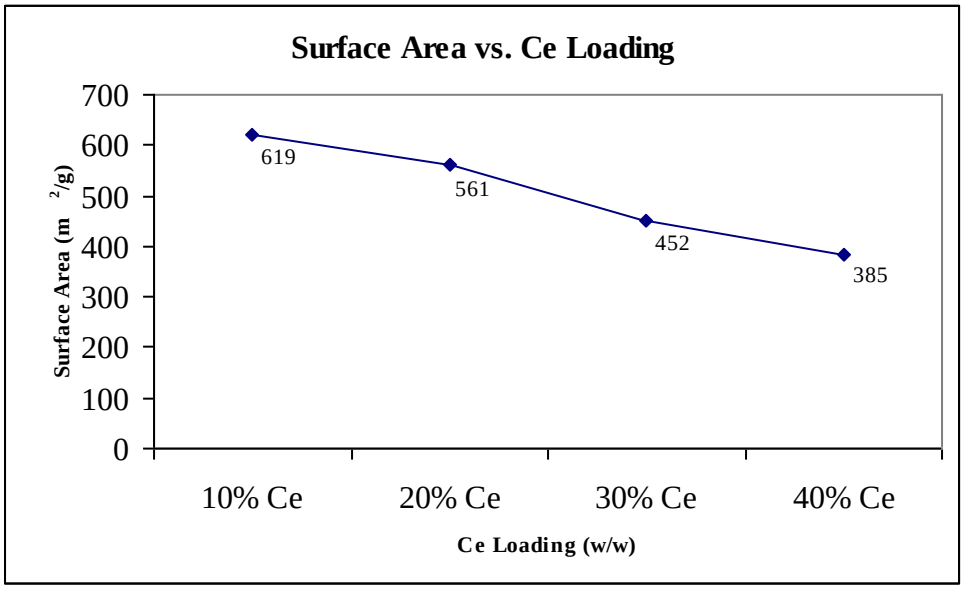


Figure 3. Surface area of ceria on silica aerogels as a function of cerium content.

As important as high surface area is the ability of a ceria-based catalyst to maintain its surface area at high temperatures. It has been previously shown that ceria itself undergoes a dramatic loss of surface area even around 300 ºC. Notably, our aerogel-supported ceria doesn't show the same decrease in surface area. For a series of 20% ceria catalysts, calcinations up to 650 ºC still yield substantially the same high surface areas (see Figure 4). Additional data from the Seehra group substantiated this claim by demonstrating that the average particle size was also unchanged. The activities of the aerogel-supported ceria catalysts compare favorably with

traditional ceria-based catalysts, thereby demonstrating substantial potential for both cost savings and reactivity increases with our composite catalysts.

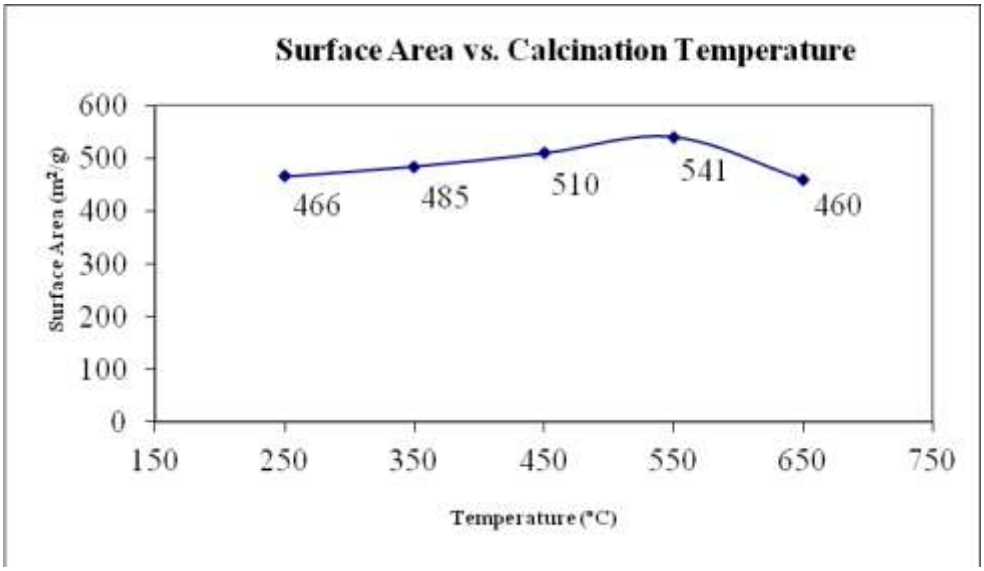


Figure 4. Surface areas of 20% ceria on silica aerogels as a function of calcination temperature.

A U.S. Patent application for the production of this thermally stable, high surface area ceria has been submitted. Considering the importance of ceria in a number of applications, including automobile catalytic converters, we believe this to be potentially useful.

## VIII. References/Publications

1. Sumit Bali, Gregory C. Turpin, Richard D. Ernst, Ronald J. Pugmire, Vivek Singh, Mohindar S. Seehra, and Edward M. Eyring, "Water Gas Shift Catalysis Using Iron Aerogels Doped with Palladium by the Gas-Phase Incorporation Method", *Energy & Fuels*, **22** (2008) 1439–1443.

2. Jennifer L. Gasser-Ramirez, Brian C. Dunn, Daniel W. Ramirez, Eric P. Fillerup, Gregory C. Turpin, Yifan Shi, Richard D. Ernst, Ronald J. Pugmire, Edward M. Eyring, Katherine A. Pettigrew, Debra R. Rolison, and Joel M. Harris, "A simple synthesis of catalytically active, high surface area ceria aerogels", *J. Non-Cryst. Solids*, **354** (2008) 5509-5514.

3. Sumit Bali, Frank E. Huggins, Richard D. Ernst, Ronald J. Pugmire, Gerald P. Huffman, and Edward M. Eyring, "Iron-Ceria Aerogels Doped with Palladium as Water-Gas Shift Catalysts for the Production of Hydrogen", *Ind. Eng. Chem. Res.*, **49** (2010) 1652–1657.

4. P. Dutta, S. Pal, M. S. Seehra, Y. Shi, E. M. Eyring, and R. D. Ernst, "Concentration of $Ce^{3+}$ and Oxygen Vacancies in Cerium Oxide Nanoparticles", *Chem. Mater.*, **18** (2006) 5144–5146.

5. Sumit Bali, Marcus Tofanelli, Richard D. Ernst, and Edward M. Eyring, "Chromium(III) catalysts in ionic liquids for the conversion of glucose to 5-(hydroxymethyl)furfural (HMF): Insight into metal catlalyst:ionic liquid mediated conversion of cellulosic biomass to biofuels and chemicals", *Biomass and Bioenergy*, **42** (2012) 224-227.

6. Dae Jung Kim, Brian C. Dunn, Frank Huggins, Gerald P. Huffman, Min Kang, Jae Eui Yie, and Edward M. Eyring, "SBA-15-Supported Iron Catalysts for Fischer–Tropsch Production of Diesel Fuel", *Energy & Fuels*, **20** (2006) 2608–2611.

7. Frank E. Huggins, Dae-Jung Kim, Brian C. Dunn, Edward M. Eyring, and Gerald P. Huffman, "An evaluation of least-squares fitting methods in XAFS spectroscopy: Iron-based SBA-15 catalyst formulations", *Spectrochimica Acta, Part A*, **72** (2009) 975-983.

8. Sumit Bali, Frank E. Huggins, Gerald P. Huffman, Richard D. Ernst, Ronald J. Pugmire, and Edward M. Eyring, "Iron Aerogel and Xerogel Catalysts for Fischer-Tropsch Production of Diesel Fuel", *Energy and Fuels*, **23** (2009) 14-18.

9. Sumit Bali, Garima Bali, Frank E. Huggins, Mohindar S. Seehra, Vivek Singh, Jared M. Hancock, Roger Harrison, Gerald P. Huffman, Ronald J. Pugmire, Richard D. Ernst, and Edward M. Eyring, "Synthetic Doped Amorphous Ferrihydrite for the Fischer−Tropsch Synthesis of Alternative Fuels", *Ind. Eng. Chem. Res.*, **51** (2012) 4515-4522.

10. Brian C. Dunn, Paul Cole, Daniel Covington, Matthew C. Webster, Ronald J. Pugmire, Richard D. Ernst, Edward M. Eyring, Naresh Shah, and Gerald P. Huffman, "Silica aerogel supported catalysts for Fischer–Tropsch synthesis", *Applied Catalysis A*, **278** (2005) 233–238.

11. P. Dutta, B. C. Dunn, E. M. Eyring, N. Shah, G. P. Huffman, A. Manivannan, and M. S. Seehra, "Characteristics of Cobalt Nanoneedles in 10% Co/Aerogel Fischer−Tropsch Catalyst", *Chem. Mater.*, **17** (2005) 5183–5186.

12. Dae Jung Kim, Brian C. Dunn, Paul Cole, Greg Turpin, Richard D. Ernst, Ronald J. Pugmire, Min Kang, Ji Man Kim, and Edward M. Eyring, "Enhancement in the reducibility of cobalt oxides on a mesoporous silica supported cobalt catalyst", *Chem. Commun.*, (2005) 1462-1464.

13. A. Braun, J. Ilavsky, B. C. Dunn, P. R. Jemian, F. E. Huggins, E. M. Eyring and G. P. Huffman, Ostwald ripening of cobalt precipitates in silica aerogels? An ultra-small-angle X-ray scattering study", *J. Appl. Cryst.*, **38** (2005) 132-138.

14. Zhiru Ma, Brian C. Dunn, Gregory C. Turpin, Edward M. Eyring, Richard D. Ernst, and Ronald J. Pugmire, "Solid state NMR investigation of silica aerogel supported Fischer-Tropsch catalysts", *Fuel Processing Technology*, **88** (2007) 29–33.

15. Yifan Shi, Atta M. Arif, and Richard D. Ernst, "Use of pyrazolyl ligands for the formation of a bimetallic cobalt-ruthenium complex", *Polyhedron*, **30** (2011) 1899 – 1905.

16. Zhiru Ma, Julio C. Facelli, Ronald J. Pugmire, Brian C. Dunn, Gregory C. Turpin, Edward M. Eyring, and Richard D. Ernst, "Solid-state $^{13}C$ NMR and quantum chemical investigation of meal diene complexes", *Magnetic Resonance in Chemistry*, **45** (2007) 393-400.

17. Min Kang, Dae Jung Kim, Eun Duck Park, Ji Man Kim, Jae Eui Yie, Seoung Hyun Kim, Louisa Hope-Weeks, and Edward M. Eyring, "Two-stage catalyst system for selective catalytic reduction of $NO_x$ by $NH_3$ at low temperatures", *Applied Catalysis B: Environmental*, **68** (2006) 21-27.

18. Richard D. Ernst, Edward M. Eyring, Gregory C. Turpin, and Brian C. Dunn, "Methods of Selectively Incorporating Metals onto Substrates", U. S. Patent 7,429,404 (2008).

IX. Student Participants.

**Undergraduates**

Bryce Anderson was excellent not only in the lab but also as a student (3.99 gpa). He had also served two tours of duty in Iraq and Afghanistan. He went on to graduate studies in chemistry at MIT under Prof. Daniel Nocera. Prof. Nocera has recently accepted a position at Harvard University, so Bryce is now continuing his Ph.D. studies there.

**Lisa Chan** has gone on to medical school at Pennsylvania State University.

**Marcus Tofanelli** has gone on to graduate studies in chemistry at the Colorado State University.

**Daniel Ramirez** was an undergraduate student here who took a local job at Ceramatech after finishing his degree.

**Eric Fillerup** received his B.S. degree here and thereafter went to Penn. State for graduate studies.

**Graduate Students**

**Ben Harvey** received his Ph.D. in 2005, and took a postdoctoral position at the China Lake Naval Labs. They do not guarantee any permanence, and so postdocs are advised to look for permanent employment from the day they arrive. On the day that his colleagues heard he had received an invitation for an interview elsewhere, China Lake made him a permanent offer. This last year he has received two major awards, the 2012 NAVAIR Commander's National Award for work on alcohol-to-jet (ATJ) fuels and the 2011 Dr. Delores M. Etter Top Scientists and Engineers of the Year Award (Navy wide), as can be verified by the following links:

http://www.navair.navy.mil/index.cfm?fuseaction=home.PrintNewsStory&id=5104

http://www.serdp.org/News-and-Events/News-Announcements/Program-News/Navy-recognizes-Dr.-Benjamin-Harvey-as-up-and-coming-top-scientist

http://www.navy.mil/submit/display.asp?story_id=69092

http://www.aerotechnews.com/chinalake/2012/06/29/nawcwd-teams-get-navair-commanders-awards/

**Yifan Shi** received his Ph.D. in 2009, and initially took a position at a large pharmaceutical company in Madison, Wisconsin. However, his wife found employment out on the east coast, so Yifan ultimately took a position with Alliance Pharma, Inc. in Malvern, Pennsylvania.

**Gregory Turpin** has passed his Ph.D. exam but not yet turned in a corrected version of his thesis.

**Emily Heider** was a Ph.D. student in Joel Harris's group, and has since taken a position at Florida State University.

**Jennifer Gasser** was a Ph.D. student in Joel Harris's group, and has since taken a position at Thermo Fisher Co.

**Postdoctoral Students**

**Rehan Basta** received her Ph.D. here in 2004, and later did some postdoctoral work in the Ernst group. She now works at Watson Pharmaceuticals in Salt Lake City, Utah, where she has received at least a couple of promotions.

**Feng Lu** was a postdoc with us for 1.5 years, and currently is a postdoc here in the group of Prof. Joel Miller.

**Sumit and Garima Bali** were postdocs, who have since taken new postdoctoral positions at Georgia Tech. University.

**Brian Dunn** was a postdoc who is now working at Conoco Phillips in Bartlesville, Oklahoma.

**Dae Jung Kim** was a postdoc who has taken a position as a Research Engineer at the Center for Applied Energy Research at the University of Kentucky.

**Nam Sun Roh** was a postdoc who has since taken a position at the Korean Institute of Energy Research.

**Zhiru Ma** was a postdoc who has taken a position at an automobile manufacturing company.